

The Kondo Lattice Model: a Dynamical Cluster Approximation Approach

Dissertation zur Erlangung des
naturwissenschaftlichen Doktorgrades
der Julius-Maximilians-Universität Würzburg

8. Dezember 2009

vorgelegt von
Lee C. Martin
aus Basingstoke

Würzburg 2009

Eingereicht am: 8. Dezember 2009
bei der Fakultät für Physik und Astronomie

1. Gutachter: Prof. Dr. Fakher Assaad
2. Gutachter:
der Dissertation.

1. Prüfer: Prof. Dr. Fakher Assaad
2. Prüfer:
3. Prüfer:
im Promotionskolloquium

Tag des Promotionskolloquiums:

Doktorurkunde ausgehändigt am:

Abstract

We apply an antiferromagnetic symmetry breaking implementation of the dynamical cluster approximation (DCA) to investigate the two-dimensional hole-doped Kondo lattice model (KLM) with hopping t and coupling J . The DCA is an approximation at the level of the self-energy. Short range correlations on a small cluster, which is self-consistently embedded in the remaining bath electrons of the system, are handled exactly whereas longer ranged spacial correlations are incorporated on a mean-field level. The dynamics of the system, however, are retained in full. The strong temporal nature of correlations in the KLM make the model particularly suitable to investigation with the DCA.

Our precise DCA calculations of single particle spectral functions compare well with exact lattice QMC results at the particle-hole symmetric point. However, our DCA version, combined with a QMC cluster solver, also allows simulations away from particle-hole symmetry and has enabled us to map out the magnetic phase diagram of the model as a function of doping and coupling J/t .

At half-filling, our results show that the linear behaviour of the quasi-particle gap at small values of J/t is a direct consequence of particle-hole symmetry, which leads to nesting of the Fermi surface. Breaking the symmetry, by inclusion of a diagonal hopping term, results in a greatly reduced gap which appears to follow a Kondo scale.

Upon doping, the magnetic phase observed at half-filling survives and ultimately gives way to a paramagnetic phase. Across this magnetic order-disorder transition, we track the topology of the Fermi surface. The phase diagram is composed of three distinct regions: Paramagnetic with *large* Fermi surface, in which the magnetic moments are included in the Luttinger sum rule, lightly antiferromagnetic with large Fermi surface topology, and strongly antiferromagnetic with *small* Fermi surface, where the magnetic moments drop out of the Luttinger volume. We draw on a mean-field Hamiltonian with order parameters for both magnetisation and Kondo screening as a tool for interpretation of our DCA results. Initial results for fixed coupling and doping but varying temperature are also presented, where the aim is look for signals of the energy scales in the system: the Kondo temperature T_K for initial Kondo screening of the magnetic moments, the Neel temperature T_N for antiferromagnetic ordering, a possible T^* at which a reordering of the Fermi surface is observed, and finally, the formation of the coherent heavy fermion state at T_{coh} .

Kurzfassung

Wir setzen eine Implementierung der dynamischen Cluster Näherung (DCA) mit gebrochener Symmetrie ein um das zweidimensionale lochdotierte Kondo Gitter Model (KLM) mit dem Hüpfmatrixelement t und der Kopplung J zu untersuchen. Die DCA beruht auf einer Näherung der Selbstenergie. Kurzreichweitige Korrelationen auf einem kleinen Cluster, der selbstkonsistent in ein Bad der übrigen Systemelektronen eingebettet ist, werden exakt behandelt, während langreichweitige Korrelationen auf Mean-Field Basis berücksichtigt werden. Dabei wird jedoch die Dynamik des Systems voll beibehalten. Auf Grund starker dynamischer Korrelationen zeigt sich das KLM als besonders geeignet für Untersuchungen im Rahmen der DCA.

Präzise Berechnungen der Einteilchen Spektralfunktion geben gute Übereinstimmung mit exakten Gitter-QMC Resultaten am Teilchen-Loch symmetrischen Punkt. Unsere DCA Version, kombiniert mit einem QMC Cluster Solver, erlaubt es, Simulationen fern vom Teilchen-Loch symmetrischen Punkt durchzuführen und hat es uns ermöglicht das magnetische Phasendiagramm des Modells als Funktion der Dotierung und der Kopplung J/t abzutasten.

Bei halber Füllung zeigen unsere Resultate, dass das lineare Verhalten der Quasiteilchenlücke bei kleinem J/t direkt aus der vorliegenden Teilchen-Loch Symmetrie, die ihrerseits zu Nesting führt, hervorgeht. Brechung dieser Symmetrie durch das Einführen eines diagonalen Hüpfmatrixelements, hat eine an die Kondo Skala gekoppelte, stark reduzierte Quasiteilchenlücke zur Folge.

Im dotiertem System setzt sich die bei Halfüllung beobachtete magnetische Phase fort bis sie letztendlich der paramagnetischen Phase weicht. Wir verfolgen die Entwicklung der Topologie der Fermifläche beim Durchstoßen dieses magnetischen Übergangs vom Ordnungs- zum Unordnungsregime. Das Phasendiagramm unterteilt sich in drei verschiedenen Regionen: Den Paramagnetischen Bereich mit *großer* Fermifläche, in dem die magnetische Momente zum Luttinger Volumen beitragen, den schwachen Antiferromagneten, mit großer Fermiflächetopologie, und den starken Antiferromagneten mit *kleiner* Fermifläche, bei dem die magnetischen Momente nicht am Luttinger Volumen beteiligt sind. Wir beziehen uns zur weiteren Interpretation unserer DCA Resultate auf einen Mean-Field Hamiltonian mit Ordnungsparametern sowohl für die Magnetisierung als auch für die Kondo-Abschirmung.

Erste Resultate bei fester Kopplung und Dotierung, jedoch bei unterschiedlichen Tem-

peraturen, zwecks der Ermittlung der verschiedene Energieskalen des Systems, werden dargestellt. Wir suchen Signale der Kondo Temperatur T_K bei der die Kondo-Abschirmung der magnetische Momente einsetzt, der Neel Temperatur T_N der antiferromagnetischem Ordnung, das eventuelle Auftreten einer durch T^* gekennzeichnete Änderung der Fermiflächen Topologie, und letztendlich die Ausbildung eines kohärenten schwerfermionischen Zustandes bei T_{coh} .

Contents

1	Introduction	9
1.1	Weak Coupling and Strong Coupling limits of the KLM	11
1.2	Correlation, Screening and Magnetisation	14
2	Mean Field Theory, Dynamical Mean Field Theory, and the Dynamical Cluster Approximation	21
2.1	The Mean Field Approach	21
2.2	Dynamical Mean Field Theory	23
2.2.1	The DMFT equations	23
2.3	The Dynamical Cluster Approximation	27
2.4	Broken Symmetry DCA	33
2.4.1	Symmetry breaking DCA definitions	34
2.4.2	Broken Symmetry DCA Self-Consistent Equations	36
2.4.3	Plotting the AF Green function in the extended BZ	41
2.5	Technical Details in the Application of the Algorithm	42
2.5.1	Start point of the DCA iterative solution process	42
2.5.2	Convergence of the solution	43
2.5.3	Interpolation of the Self-Energy	43
3	QMC Hirsch-Fye Cluster Solver	47
3.1	Auxiliary Field Quantum Monte-Carlo Formulation of the KLM	47
3.2	The Hirsch-Fye QMC algorithm in application to the KLM	52
3.2.1	Update Equations	53
4	Mean-Field and Spin Density Wave	57
4.1	The Large- \mathcal{N} Approach	57
4.2	The Spin Density Wave Approach	59
4.3	A Mixed Approach	61
5	The Half-Filled KLM	63
5.1	Perfect Nesting of the Fermi Surface	63
5.2	Magnetic Phase Transition at Half-Filling	67

5.3	Single Particle Spectrum - $t'/t = 0$	69
5.4	Single Particle Spectrum - $t'/t = -0.3$	73
5.5	The Quasi-Particle Gap	80
6	The Hole-Doped KLM	83
6.1	Magnetic Phase Diagram	83
6.2	Staggered Magnetisation	83
6.3	Single Particle Spectrum and Topology of the Fermi Surface	84
6.4	The Spectral Function for $T \neq 0$	93
7	Summary and Conclusions	97
A	Linear Response and the Kubo Formalism	101
B	Delayed Update Algorithm Improvement	105
	Bibliography	107
	Publications	113
	Curriculum Vitae	115
	Acknowledgements	117
	Versicherung an Eides statt	119

1 Introduction

In the 1960's the study of localised magnetic moments was placed firmly in the emerging field of strongly correlated electron systems when Anderson first identified interactions between localised electrons as the driving force for local moment formation [1]. Early experimentalists realised that local moment formation on magnetic iron ions dissolved in non-magnetic metals is dependent on the host [2, 3]. The magnetic susceptibility of a system of iron dissolved in a niobium-molybdenum alloy was seen to follow a Curie-Weiss law for compositions close to molybdenum, indicating the presence of local moments. The low temperature limit of Curie-Weiss susceptibility is given by the Kondo temperature, the temperature at which the local moment is screened due to the formation of an entangled spin singlet state of the local moment and surrounding conduction electrons.

At high energies the local moment in the metallic host is free, but at energies below the Kondo temperature, it interacts so strongly with the surrounding electrons that the magnetic moment is shielded by those electrons. The physics of local moment screening, the Kondo effect, manifests itself in a variety of properties of correlated electron systems including the Kondo resistivity minimum and also the formation of heavy fermion metals. With the latter, the presence of local moments greatly changes the metals properties with quasi-particles developing which may have an effective mass many times larger than the bare electron mass whilst still behaving as a Fermi liquid at low temperatures.

Such behaviour led Doniach to propose that the huge mass renormalisation has its roots in a lattice version of the Kondo effect and that such heavy fermion systems should be modelled by the Kondo lattice model (KLM) [4]. The mass renormalisation can be attributed to the coherent superposition of individual Kondo screening clouds and the resulting metallic state is characterised by a Fermi surface with Luttinger volume (Fermi surface volume) containing both conduction and localised electrons. In its simplest form, the KLM describes a lattice of spin 1/2 magnetic moments coupled antiferromagnetically via an exchange coupling J to a single band of conduction electrons and is believed to capture the physics of heavy fermion materials such as CeCu₆.

The KLM is given by the following Hamiltonian:

$$H = \sum_{\mathbf{k},\sigma} \epsilon(\mathbf{k}) c_{\mathbf{k},\sigma}^\dagger c_{\mathbf{k},\sigma} + J \sum_{\mathbf{i}} \mathbf{S}_{\mathbf{i}}^c \cdot \mathbf{S}_{\mathbf{i}}^f \quad (1.1)$$

with conduction electron creation operator $c_{\mathbf{k},\sigma}^\dagger$ creating a conduction electron on an ex-

tended orbital with wave vector \mathbf{k} and a z-component of spin $\sigma = \uparrow, \downarrow$. The spin 1/2 degrees of freedom, coupled via J , are represented with the aid of the Pauli spin matrices $\boldsymbol{\sigma}$ by

$$\mathbf{S}_i^c = \frac{1}{2} \sum_{s,s'} c_{i,s}^\dagger \boldsymbol{\sigma}_{s,s'} c_{i,s'} \quad (1.2)$$

or the equivalent definition for \mathbf{S}_i^f using the localised orbital creation operators $f_{i,\sigma}^\dagger$. The KLM forbids charge fluctuations on the f -orbitals and as such the constraint of one electron per localised orbital must be included.

Although the physics of the single impurity Kondo problem is well understood [5] the KLM still poses a problem half a century since its original conception. The difficulty with the lattice problem arises due to the presence of two competing energy scales. The first energy scale, given by the Kondo temperature, is associated with the screening of impurity spins via the Kondo effect. At constant density, the J dependence of the inverse effective mass — or the coherence temperature — has been argued to track this single ion Kondo scale [6, 7]. However, in the lattice problem, polarisation of the conduction electron spins around a first magnetic impurity can couple to a second impurity leading to an effective interaction between impurity spins, the Ruderman-Kittel-Kasuya-Yosida (RKKY) interaction [8, 9, 10], and an associated second energy scale. This RKKY scale dominates at low values of the exchange coupling and is the driving force for the observed magnetic order-disorder quantum phase transitions in heavy fermion materials.

The nature of this phase transition is of current interest following experimental results suggesting a sudden change in the Fermi surface topology at the quantum critical point (QCP) for the heavy fermion metal YbRh_2Si_2 [11]. Tuning this system from the non-magnetic heavy fermion metallic phase to the antiferromagnetic metallic phase causes a rapid change in the low temperature Hall coefficient which is extrapolated to a sudden jump at $T = 0$. Since the low-temperature Hall coefficient is related to the Fermi surface volume the results are interpreted as showing a sudden reordering of the Fermi surface at the QCP from a *large* Fermi surface, where the local moment impurity spins are included in the Luttinger volume, to a *small* Fermi surface where the impurity spins drop out of the Fermi surface volume. This scenario lies at odds with the Hertz-Millis description of the quantum phase transition [12, 13] and has triggered alternative descriptions [14, 15]. More recently it has been experimentally shown that the Fermi surface topology change does not necessarily occur only at the magnetic order-disorder QCP. For examples we think of CeIn_3 [16] or $\text{CeRh}_{1-x}\text{Co}_x\text{In}_5$ [17]. In fact, even in YbRh_2Si_2 it has now been shown that the Fermi surface reconstruction can be shifted away from the magnetic phase transition to either side of the QCP via application of positive or negative chemical pressure [18]. In yet another recent example, neutron scattering experiments on the heavy-fermion system $\text{Ce}_{1-x}\text{La}_x\text{Ru}_2\text{Si}_2$ show that, there, fluctuations of the antiferromagnetic order parameter are responsible for the magnetic phase transition and that the transition is well understood

in terms of the Hertz-Millis approach [19].

To summarise, recent experimental results indicate a complicated phase diagram centred around an antiferromagnetic QCP in heavy fermion systems often with the involvement of a restructuring of the Fermi surface. The magnetic phase transition does not however appear to be directly connected with the topology change in all model systems such that in many cases the Hertz-Millis theory of quantum phase transitions holds. In such cases the topology change can be interpreted as a crossover and not the result of the local critical fluctuations proposed in references [14, 15]. The factors controlling the Fermi surface topology are currently of much interest.

In this work we investigate the interplay between Kondo screening and the RKKY interaction in the 2D KLM concentrating in particular on the nature of the phase transition and Fermi surface topology of the ground state. To achieve this we employ a variant of the Dynamical Cluster Approximation (DCA) with a quantum Monte-Carlo algorithm as cluster solver. An introduction to the DCA and in particular our own symmetry breaking DCA variant, is given in chapter 2. Following this, in chapter 3, we review relevant aspects of the QMC solver algorithm as it pertains the KLM Hamiltonian. Chapter 4 considers the KLM on the basis of simple mean-field or spin density wave (SDW) approaches which are then drawn on in the chapters following to gain extra insight into the numerical results. In chapter 5 the KLM is considered at half-filling. Comparison with previous QMC results is made in order to validate our method followed by detailed analysis of the magnetisation, single particle spectra and quasi-particle gap as a function of coupling J/t . Finally, in chapter 6, the system is hole-doped and we map out the magnetic phase diagram as a function of doping and coupling. Here we examine the RKKY driven quantum phase transition to the AF ordered state and follow the evolution of the Fermi surface across this transition. Initial results with increasing temperature are also shown here before we summarise in chapter 7.

Now, before beginning with the description of our numerical methods we use the following introductory sections of this chapter to make some general points about the KLM and in particular to consider the competing effects of RKKY interaction and Kondo screening, which make the model interesting in the first place.

1.1 Weak Coupling and Strong Coupling limits of the KLM

At half-filling and for $J/t \rightarrow \infty$ the ground state of the KLM is a spin liquid in any dimensions [20]. This state is characterised by quantum disorder amongst the spins and also spin and charge correlation functions that decay exponentially in space and time. If we consider the limit $J/t = \infty$ then the wavefunction must be a product of single-site wavefunctions. The single site eigenstates and corresponding energies are:

$$\begin{array}{ll}
\text{singlet} & \frac{1}{\sqrt{2}}(|\uparrow\rangle_f |\downarrow\rangle_c - |\downarrow\rangle_f |\uparrow\rangle_c) \quad E = -\frac{3}{4}J \\
\text{triplet} & \left\{ \begin{array}{l} |\uparrow\rangle_f |\uparrow\rangle_c \\ |\downarrow\rangle_f |\downarrow\rangle_c \\ \frac{1}{\sqrt{2}}(|\uparrow\rangle_f |\downarrow\rangle_c + |\downarrow\rangle_f |\uparrow\rangle_c) \end{array} \right. \quad E = \frac{1}{4}J \\
\text{doublet} & |\uparrow\rangle_f |\uparrow\downarrow\rangle_c \quad ; \quad |\downarrow\rangle_f |\uparrow\downarrow\rangle_c \quad E = 0 \\
\text{doublet} & |\uparrow\rangle_f |0\rangle_c \quad ; \quad |\downarrow\rangle_f |0\rangle_c \quad E = 0.
\end{array}$$

The energy spectrum for the complete system is easily labelled via two quantum numbers (N_d, N_t) : The number of doubly occupied or empty sites, N_d , and the number of on-site triplets, N_t . The energy of a general state for the half-filled N -site system is calculated by summing up the energies of the composite single-site states:

$$E(N_d, N_t) = -\frac{3}{4}JN + \frac{3}{4}J \cdot 2N_d + JN_t. \quad (1.3)$$

The factor 2 in the second term in the sum is because at half-filling, the number of doubly occupied conduction electron sites equals the empty sites. The ground state at half-filling in the $J/t = \infty$ limit will therefore be a product state of on-site singlets and be defined by the quantum numbers $(0, 0)$. The lowest spin excitation out of the ground state is achieved by breaking a singlet to form a triplet. The spin gap to this excited state $(0, 1)$ is $\Delta_s = J$. The quasiparticle gap, the energy required to add/remove an electron is just $\Delta_{qp} = \frac{3}{4}J$. The charge gap $\Delta_c = \frac{3}{2}J$ is the energy required for excitation to $(1, 0)$, thereby changing the charge configuration. Now since the charge, spin and quasiparticle excitations are all gapped, the strong coupling $J/t = \infty$ limit is a suitable start for perturbation theory in t/J to investigate the nature of the system at progressively smaller J/t . In particular, the low level excitations will evolve continuously with decreasing J/t .

Alternatively, we can consider the spin liquid phase from the hybridisation picture given by the periodic Anderson model (PAM) also used as a model for heavy fermion systems. The PAM Hamiltonian is given by

$$H_{PAM} = \sum_{k,\sigma} \epsilon(\mathbf{k}) c_{\mathbf{k}\sigma}^\dagger c_{\mathbf{k}\sigma} + V \sum_{i,\sigma} \left(c_{i\sigma}^\dagger f_{i\sigma} + f_{i\sigma}^\dagger c_{i\sigma} \right) + \sum_{i,\sigma} \epsilon_f n_{i\sigma}^f + U \sum_i n_{i\uparrow}^f n_{i\downarrow}^f \quad (1.4)$$

where V defines the degree of hybridisation between the conduction band and localised f-orbitals at each site. A Coulomb repulsion U is only applied to the f-electrons. Anderson showed for the single-site model, with an f-orbital at a single site only, that under the symmetric condition

$$E_F - \epsilon_f = \epsilon_f + U - E_F, \quad (1.5)$$

where E_F is the Fermi energy, then the energy required for the doubly occupied f-site is the same as for the empty f-site. As long as the upper and lower levels have little overlap

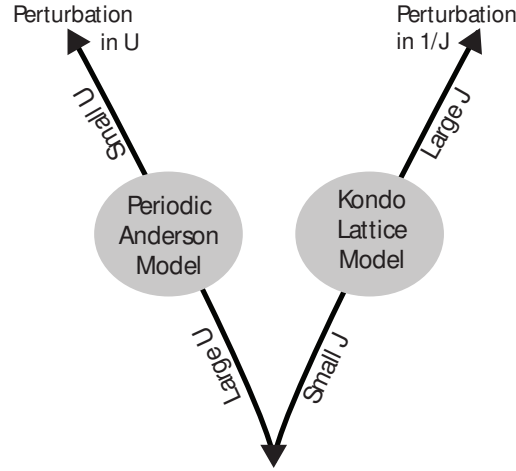


Figure 1.1: Limiting cases of the KLM and the PAM.

with the Fermi energy, then the Coulomb term causes the f -site to be singly occupied on average. In the PAM, as long as the f level is well below the Fermi energy, a large U will still mean that the occupancy on the f -sites is close to one. This is the Kondo regime of the PAM. More formally, the KLM can be derived from the PAM via a Schrieffer-Wolff transformation [21]. In this way, the KLM coupling parameter is related to the PAM parameters as $J \propto \frac{V^2}{U}$. We recognise that the large U limit of the PAM is equivalent to the small J limit of the KLM (Fig. 1.1).

Interestingly, the large J/t spin liquid limit of the KLM, can still be linked to the PAM in the small U limit even though only with a *large* U acting between the f -electrons can we arrive at the KLM with the condition of single occupancy on the f -sites fulfilled. For $U = 0$ the (non-interacting) PAM just describes the hybridisation between the c and f electrons. The Hamiltonian would be

$$H_{PAM}^0 = \sum_{k,\sigma} \begin{pmatrix} c_{\mathbf{k}\sigma}^\dagger & f_{\mathbf{k}\sigma}^\dagger \end{pmatrix} \begin{pmatrix} \epsilon(\mathbf{k}) & V \\ V & \epsilon_f \end{pmatrix} \begin{pmatrix} c_{\mathbf{k}\sigma} \\ f_{\mathbf{k}\sigma} \end{pmatrix}. \quad (1.6)$$

Diagonalising this Hamiltonian gives an upper and a lower hybridised band in the quasi-particle spectrum with energies

$$E_{\pm}(\mathbf{k}) = \frac{1}{2} \left(\epsilon(\mathbf{k}) + \epsilon_f \pm \sqrt{(\epsilon(\mathbf{k}) - \epsilon_f)^2 + 4V^2} \right) \quad (1.7)$$

and the quasi-particles are created with hybridised operators $\gamma_{\mathbf{k}\sigma}^\dagger = u_{\mathbf{k}}c_{\mathbf{k}\sigma}^\dagger + v_{\mathbf{k}}f_{\mathbf{k}\sigma}^\dagger$ and $\eta_{\mathbf{k}}^\dagger = -v_{\mathbf{k}}c_{\mathbf{k}\sigma}^\dagger + u_{\mathbf{k}}f_{\mathbf{k}\sigma}^\dagger$ (where $|u_{\mathbf{k}}|^2 + |v_{\mathbf{k}}|^2 = 1$) such that

$$H_{PAM}^0 = \sum_{k,\sigma} \left(E_+(\mathbf{k})\gamma_{\mathbf{k}\sigma}^\dagger\gamma_{\mathbf{k}\sigma} + E_-(\mathbf{k})\eta_{\mathbf{k}\sigma}^\dagger\eta_{\mathbf{k}\sigma} \right). \quad (1.8)$$

When the hybridisation matrix element V is zero, the two electron systems are completely decoupled and we have localised f -spins with atomic state energies ϵ_f embedded in a conduction band of free c -electrons. But with $V \neq 0$ the quasi-particles are of c - f nature, or hybridised, and display a two-band gapped spectrum where the maximum of the lower band is at (π, π) and the minimum of the upper band at $(0, 0)$. Turning on a small Coulomb interaction will progressively renormalise the hybridised bands as correlation effects strengthen.

We get exactly the same hybridised band structure for the KLM in the $J \rightarrow \infty$ limit if we come at it with the large- \mathcal{N} mean-field approach shown in section 4.1. We have also already argued above that the strong coupling KLM is a suitable point for perturbative expansion in t/J to lower values of J .

From the above we have tried to make clear the connection between the KLM and the PAM in the large J - small U limit. In this limit the KLM cannot be derived from the PAM but, taking both as models in their own right, the respective limits produce the same spin liquid phase and this phase evolves continuously away from the limit. At small J , large U , the models converge (Fig. 1.1).

However, at small J/t the nature of the phase is not so clear. Consider to begin with $J/t = 0$. Here the localised spins are completely decoupled from the conduction electrons which themselves are just a free electron gas. Due to the freedom of the localised spins, the total system is highly degenerate. The system will be a paramagnetic metal with gapless spin and charge excitations. Even in one dimension, where long range AF order cannot exist, it is difficult to predict whether the paramagnetic metallic state of $J = 0$ will persist to small finite values of J/t since the smallest of couplings lifts the degeneracy caused by the free localised spins and introduces complex correlation effects. In fact, for dimensions $d \geq 2$ and at small values of J/t , the ground state of the system displays long range AF order mediated by the RKKY interaction to be described shortly, i.e. the system is in the Neel state with gapless magnon excitations. We see that the point $J = 0$ can be considered a singular limit, where the model is of such a different nature to the limit of $J/t \rightarrow 0$, that a perturbative expansion in J/t around $J = 0$ is not an easy matter.

1.2 Correlation, Screening and Magnetisation

The complexities of the KLM and the PAM are quite subtle. Correlations in these models are due to scattering events with the localised spins. This is easily visualised in the KLM by considering a conduction electron moving around the lattice. At each lattice site it can undergo a spin flip process involving the localised spin at that site if both partners have antiparallel spin. The conduction electron therefore leaves a spin flip trail in the localised spins as it moves around the lattice. Whether a second conduction electron moving onto a

lattice site can undergo a spin flip is then dependent on the spin flip trail left by the first conduction electron and, of course, all the other conduction electrons. All the itinerant conduction electrons and the localised spins are therefore correlated with one another in a highly complex manner. We can also see on the basis of this intuitive argument that the correlations must be of a strong temporal nature, since the second electron feels the effects of the trail left by the first at a given site only when it itself arrives at that site some time later.

It is argued, however, that determination of the ground state can be reduced to basically considering two competing effects. The first is the extension of the idea of Kondo screening to a dense Kondo lattice of impurities. Initially beginning with a single impurity with spin state $|\uparrow\rangle_f$ or $|\downarrow\rangle_f$, it becomes energetically favourable at sufficiently low temperatures for a conduction electron at the lattice site of the impurity to build an entangled Kondo singlet state,

$$|\text{Kondo singlet}\rangle = \frac{1}{\sqrt{2}}(|\uparrow\rangle_f|\downarrow\rangle_c - |\downarrow\rangle_f|\uparrow\rangle_c), \quad (1.9)$$

such that the magnetic impurity spin is fully screened. This is known as the Kondo effect and the temperature scale for its onset is given by the Kondo temperature T_K which scales as

$$T_K \sim e^{-\frac{t}{J}}. \quad (1.10)$$

The Kondo temperature can also be thought of in connection with the tunnelling rate τ^{-1} describing the amplitude for a spin flip process of the impurity spin state. If the impurity spin is strongly correlated with the surrounding electrons the high rate of spin flips means that the magnetic moment disappears. The temperature at which this occurs defines the Kondo temperature as

$$T_K \sim \tau^{-1} \quad (1.11)$$

below which the magnetic moment is screened.

For the single impurity problem the Kondo singlet acts as a scattering centre, which gives rise to an increase in the resistivity at low temperature and a minimum in the resistivity curve. In the Kondo lattice problem, with magnetic impurities at every lattice site, again there is an increase in resistivity as the crossover to Kondo screening takes place with decreasing temperature. The temperature of this crossover will be related to the single impurity Kondo temperature but modified by lattice effects. With further temperature decrease scattering begins to take place coherently in accordance with Bloch theory for a periodic scattering potential, and a narrow band with width of the order T_K is formed. The narrow band has such little curvature that the effective mass m^* of the quasiparticles is very large giving rise to the term *heavy fermions*. Experimentally,

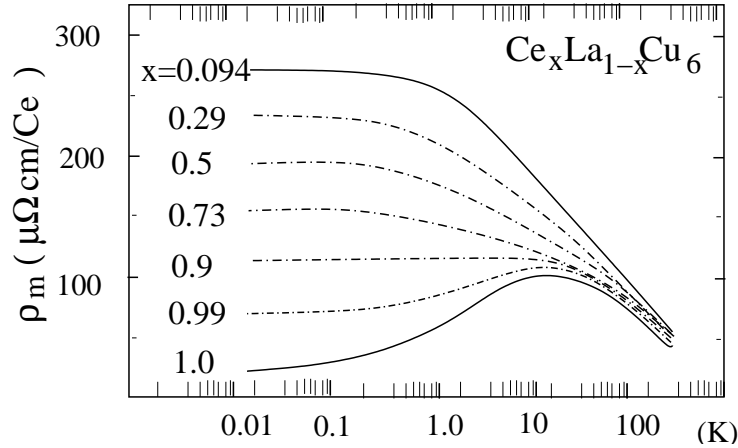


Figure 1.2: Resistance in $\text{Ce}_{1-x}\text{La}_x\text{Cu}_6$ as a function of temperature [22]. Coherence develops as x approaches 1.

the development of the coherent heavy fermion state has also been observed by gradually increasing the concentration of Ce in LaCu_6 [22] (Fig. 1.2). This is equivalent to increasing the concentration of magnetic moments in the non-magnetic conduction electron sea. With the development of coherence ($x \rightarrow 1$ in Fig. 1.2) the temperature dependency of the resistivity follows

$$\rho = \rho_0 + AT^2 \quad (1.12)$$

in accordance with Fermi liquid theory. In this regime the electronic specific heat also becomes linear

$$C_V = \gamma^*T \quad (1.13)$$

but with a greatly enhanced linear coefficient

$$\gamma^* = \frac{m^*}{m}\gamma \quad (1.14)$$

in comparison to the γ for the conduction band in the absence of the magnetic moments. For the heavy fermion material CeCu_6 , for example, $\gamma^* = 1550\text{mJ mole}^{-1} \text{K}^{-2}$ where we make the comparison to pure Cu with $\gamma = 0.695\text{mJ mole}^{-1} \text{K}^{-2}$.

The second effect, which competes with Kondo screening, is due to the fact that localised magnetic moments can couple with each other via an indirect interaction known as RKKY, so-called after the main investigators of the mechanism: Ruderman, Kittel, Kasuya and Yosida [8, 9, 10]. We show later in chapter 5 (5.26), in connection, however, to deriving the conditions for perfect nesting, that the z-z component of the static spin susceptibility

of the conduction electrons is

$$\chi(\mathbf{q}) = -\frac{2}{N} \sum_k \frac{n_F(\epsilon(\mathbf{k})) - n_F(\epsilon(\mathbf{k} + \mathbf{q}))}{\epsilon(\mathbf{k}) - \epsilon(\mathbf{k} + \mathbf{q})} \quad (1.15)$$

with the Fermi function n_F and conduction electron dispersion $\epsilon(\mathbf{k})$. A localised magnetic impurity at site j will cause a spin polarisation of the conduction electrons, and this response at a site i is governed by the strength of the coupling J between the impurity spin and the electron spin at site j multiplied with the real-space Fourier transform of the susceptibility:

$$\chi(\mathbf{r}_i - \mathbf{r}_j) = \sum_{\mathbf{q}} \chi(\mathbf{q}) e^{i\mathbf{q}(\mathbf{r}_i - \mathbf{r}_j)}. \quad (1.16)$$

A second magnetic impurity at site i can, in turn, again couple to the spin density at i via the hybridisation coupling J . We therefore have an effective interaction between magnetic moments at sites i and j :

$$J_{\text{RKKY}}(\mathbf{r}_i - \mathbf{r}_j) \sim J^2 \chi(\mathbf{r}_i - \mathbf{r}_j, \omega = 0). \quad (1.17)$$

As an example of the form this interaction can explicitly take we consider a simple quadratic band $\epsilon(\mathbf{k}) = \frac{\mathbf{k}^2}{2m}$ in three dimensions. In this simplified case, calculation (for example [23]) shows the effective interaction J_{RKKY} to be

$$J_{\text{RKKY}}(r_i - r_j) \sim -J^2 D(k_F) \frac{\cos(2k_F(r_i - r_j))}{(k_F(r_i - r_j))^3} \quad (1.18)$$

with Fermi wave vector k_F and conduction electron density of states at the Fermi wave vector $D(k_F)$. In general, we can think of a magnetic moment as a delta-function-like magnetic field placed into the conduction electron host band. This will give rise to an oscillatory response in the conduction electron spin density. It is the oscillatory nature of the effective interaction which makes the RKKY interaction the proposed mechanism for the stabilisation of the AF phase in the KLM. The oscillations in the spin density are of the same form as the Friedel oscillations in the charge density of conduction electrons screening a charged impurity in a metal. The RKKY mechanism for effective coupling of magnetic moments is illustrated in Fig. 1.3.

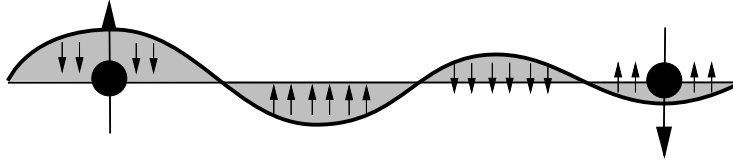


Figure 1.3: Two magnetic moments (large arrows) experience an effective coupling via the RKKY interaction. The conduction electron spins become polarised by the first magnetic moment causing Friedel oscillations in the spin density. The second magnetic moment in turn couples to the polarisation

From a k -space perspective, and considering equation (1.15), we may see the oscillation as being due to the sharp discontinuities in electron occupation at the Fermi surface, wave vector k_F , which will equate to an oscillatory form after Fourier transformation to real-space. We can associate an energy scale E_{RKKY} with the RKKY interaction J_{RKKY} such that

$$E_{\text{RKKY}} \propto J^2 \chi(\mathbf{q}, \omega = 0) = J_{\text{RKKY}}(\mathbf{q}) \quad (1.19)$$

whereas for Kondo screening of the magnetic moments the scale is given by the Kondo temperature

$$T_K \sim e^{-t/J}. \quad (1.20)$$

For large values of J/t then $T_K > E_{\text{RKKY}}$ and the Kondo screened paramagnetic ground state is found whereas for small values of J/t then $E_{\text{RKKY}} > T_K$ and RKKY induced AF order between impurity spins will dominate. The phase diagram of the KLM according to Doniach is summarised schematically in Fig. 1.4. The zero temperature transition point between the PM and AF ordered phase represents a quantum critical point. This phase transition is part of the main focus of the results presented in this work.

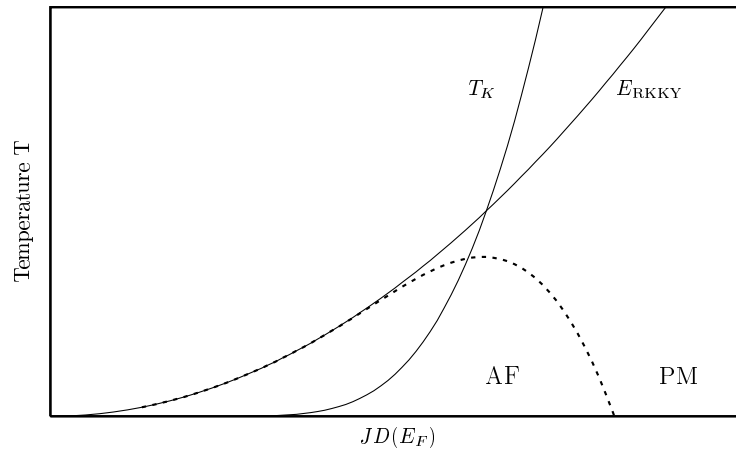


Figure 1.4: Phase diagram of the KLM according to Doniach based on comparison of the energy scales for Kondo screening T_K versus RKKY interaction E_{RKKY} . The paramagnetic (PM) and antiferromagnetic (AF) ordered states are separated by a phase transition (dotted line) terminating in a quantum critical point at zero temperature

2 Mean Field Theory, Dynamical Mean Field Theory, and the Dynamical Cluster Approximation

2.1 The Mean Field Approach

Even the simplest quantum many-body Hamiltonians pose problems in their solution. Exact solutions of the Hubbard Model, for example, which is often considered as a kind of minimalist model for strongly interacting electrons in a solid, are only available in special cases: notably, several analytical results can be obtained in one-dimension by means of the Bethe Ansatz (see, for example, the review article [24] and references therein). In general cases suitable approximations are sought with which one may capture the physics of the situation under investigation. Approximations which have some controllable limiting case are particularly desirable since in the relevant limit it is then possible to understand the essence of the approximation and its effect on the physics of the system as one moves away from this limit. In fact, expansion around some limiting case forms the basis of many systematic controllable improvement methods. We can think, here, of the example given by perturbation theory, in which the actual approximation used is decided upon on the basis of which physics are to be investigated.

Mean field theories constitute one such class of approximation methods. The underlying concept, in application to lattice models, is to replace the many site lattice by a single site embedded in an effective interaction field which is calculated self-consistently and takes into account the effect of the remaining sites. In classical and quantum spin lattice models, in which each lattice site is associated with a localised spin degree of freedom, the self-consistent equations determining the mean field are well known and their solution is known to become exact in the limiting case of infinite coordination number or, equivalently, infinite dimensions. For example consider a simple Ising-like spin model

$$H = - \sum_{i,j} J_{ij} S_i S_j \tag{2.1}$$

where S_i is a discrete variable representing the spin at site i and taking only the values ± 1 , and J_{ij} is a ferromagnetic ($J_{ij} > 0$) or antiferromagnetic ($J_{ij} < 0$) coupling between spins at i and at j . An effective Hamiltonian is created by considering each spin to be

in an effective interaction field created by all the other surrounding spins and replacing those surrounding spin operators by their expectation values $m_j = \langle S_j \rangle$. The effective Hamiltonian is then

$$H^{eff} = - \sum_i h_i^{eff} S_i \quad (2.2)$$

with the effective field at site i given by

$$h_i^{eff} = \sum_j J_{ij} m_j. \quad (2.3)$$

We note that if we assume translational symmetry and a homogeneous spin coupling between, say, nearest-neighbours only ($J_{ij} = J$ for nearest neighbours i, j and $J_{ij} = 0$ otherwise) the effective field is dependent on just a single parameter m since $m_j = m \forall j$. Solving now for the magnetisation of the spin at a given site under the influence of the effective field $h^{eff} = h_i^{eff} = zJm$ (where z is the coordination number) gives

$$m = \tanh(\beta h^{eff}). \quad (2.4)$$

We note that in order to preserve a finite entropy and internal energy per site the coupling must be rescaled as $J = \frac{J^*}{z}$ as $z \rightarrow \infty$. The mean field equations defined by (2.3) and (2.4) must be solved self-consistently.

Such spin lattice problems have the simple controllable limit of infinite dimensionality for which the approximation becomes exact. This is intuitively clear for our Ising spin example since in infinite dimensions a given spin is surrounded by infinite neighbours such that fluctuations in the local effective field become negligible.

Therefore, when applied to classical or quantum spin systems, the mean field approach displays the desirable characteristics of controllability and exactness in the limiting case of $d \rightarrow \infty$. This is all well and good for problems involving localised degrees of freedom but the system becomes fundamentally more complicated when we introduce itinerant degrees of fermionic freedom. One prominent example is the Hubbard model with Hamiltonian

$$H = -t \sum_{\langle i,j \rangle, \sigma} (a_{i\sigma}^\dagger a_{j\sigma} + h.c.) + U \sum_{i, \sigma} n_{i\uparrow} n_{i\downarrow}, \quad (2.5)$$

which includes a nearest neighbour hopping t in addition to an on-site (Coulomb) interaction U . To develop a mean-field theory for this model one may proceed analogously to the spin lattice model mean field approximation by neglecting fluctuations in the interaction field in order to reduce the Hamiltonian to that of an effective single site problem. Formally, this is achieved within the Hartree-Fock (HF) approximation by writing the two-particle interaction term, given more generally as the product of two operators A and B , as

$$AB = (A - \langle A \rangle)(B - \langle B \rangle) + A\langle B \rangle + \langle A \rangle B - \langle A \rangle \langle B \rangle. \quad (2.6)$$

The last term on the right hand side is just a product of expectation values and therefore just a complex number which cancels out in the partition function $Z = e^{-\beta H}$ when calculating the expectation value of some operator A as $\langle A \rangle = \frac{1}{Z} \text{Tr}(Ae^{-\beta H})$. The approximation is given by neglecting the first term which describes fluctuations of the operators about their expectation values:

$$AB \xrightarrow{HF} A\langle B \rangle + \langle A \rangle B - \langle A \rangle \langle B \rangle. \quad (2.7)$$

Again, we may ask ourselves whether the approximation becomes exact in the limit $d \rightarrow \infty$. Metzner and Vollhardt began study of the Hubbard model and related models in high dimensions in 1989 [25], which sparked a series of papers on the subject which showed the usefulness of the limiting case when considering such models in lesser dimensions as small as even $d = 3$ or $d = 2$ [26, 27]. However, when applied to the Hubbard model, the HF approximation does not match the exact result in the limit $d \rightarrow \infty$ [25, 26] since the neglected fluctuation term $(n_{i\uparrow} - \langle n_{i\uparrow} \rangle)(n_{i\downarrow} - \langle n_{i\downarrow} \rangle)$ in the on-site interaction is in fact of order one regardless of dimensionality.

2.2 Dynamical Mean Field Theory

The desire to find a mean field approximation for which the dimensionality d or coordination number z may be used as a control parameter to extrapolate to an exact solution in the limit $d \rightarrow \infty$ was the focus of a number of studies in the years following the groundbreaking work of Metzner and Vollhardt in 1989 [25]. For a list of the historical development of infinite dimensional studies and dynamical mean field theory (DMFT) we refer the reader to the review article of A. Georges *et al.* [28].

2.2.1 The DMFT equations

The goal is to calculate the interacting Green function

$$G(\mathbf{k}, i\omega_n) = \frac{1}{i\omega_n - (\epsilon(\mathbf{k}) - \mu) - \Sigma(\mathbf{k}, i\omega_n)} \quad (2.8)$$

for the lattice model. We wish to achieve this by some kind of mean-field approximation to deal with the spacial fluctuations whilst retaining the dynamics of the itinerant electrons and at the same time guaranteeing the controllable limit of $d \rightarrow \infty$. We begin by considering the following effective action for a dynamic model containing two-particle interactions only at a single-site:

$$S_{eff} = U \int_0^\beta d\tau n_\uparrow(\tau) n_\downarrow(\tau) - \int_0^\beta d\tau \int_0^\beta d\tau' \sum_\sigma c_\sigma^\dagger(\tau) \mathcal{G}_0^{-1}(\tau - \tau') c_\sigma(\tau') \quad (2.9)$$

The Green function \mathcal{G}_0 , which we will henceforth refer to as the bath Green function, contains all the information of the sites around a particular chosen site. In other words

the other sites have been integrated out and the action is that of an *impurity*¹ embedded in a space-averaged bath of the surrounding electrons with which the impurity interacts. Physically, \mathcal{G}_0 represents the effective amplitude for an electron to be created at the impurity site at a time τ and be destroyed again at time τ' . Or equivalently, it is the amplitude for an electron to come out of the bath onto the impurity site at a given time and return to the bath a certain time later. This bath Green function may be considered as the natural extension of the mean-field (Weiss field) seen in the Ising-spin example considered above, where the order parameter was given by the magnetisation, to the case of itinerant spins such as in the Hubbard model. The difference is that whereas for classical (or quantum spin models without hopping) the mean-field was a single parameter, in the itinerant spin model the quantity playing the role of the Weiss field, i.e. \mathcal{G}_0 , is still local in space but is now a dynamic quantity able to capture the effect of quantum fluctuations onto the impurity site. The interacting Green function to \mathcal{G}_0 for the impurity problem is given by

$$\bar{G}^{-1}(i\omega_n) = \mathcal{G}_0^{-1} - \Sigma^{\text{imp}}[\bar{G}(i\omega_n)], \quad (2.10)$$

where the skeleton expansion for the self-energy Σ^{imp} of the impurity problem is a functional of the interacting Green function \bar{G} . In this equation we are dealing with the Matsubara frequency Green function (with fermionic Matsubara frequencies $\omega_n = (2n+1)\pi/\beta$) which is obtained via

$$\bar{G}(i\omega_n) = \int_0^\beta d\tau \bar{G}(\tau) e^{i\omega_n \tau} \quad (2.11)$$

from the imaginary time Green function in turn calculated using the effective action S_{eff} :

$$\bar{G}(\tau - \tau') = -\langle T c(\tau) c^\dagger(\tau') \rangle_{S_{eff}}. \quad (2.12)$$

Now, the function $\bar{G}(i\omega_n)$ is a local function which describes the impurity site and its interactions with the effective bath. In the spirit of the mean field approach we require that the local Green function of the full model (which equates to a summation over \mathbf{k} in the first BZ) must be equal to the interacting function $\bar{G}(i\omega_n)$ of the effective impurity model. Therefore we have the condition

$$\bar{G}(i\omega_n) \stackrel{!}{=} \frac{1}{N} \sum_{\mathbf{k} \in \text{BZ}} G(\mathbf{k}, i\omega_n) = \frac{1}{N} \sum_{\mathbf{k} \in \text{BZ}} \frac{1}{i\omega_n - (\epsilon(\mathbf{k}) - \mu) - \Sigma^{\text{imp}}(i\omega_n)}. \quad (2.13)$$

This may be considered as the analogon to the requirement $h_i = \sum_j J_{ij} m_j$ (2.3) in the Ising model. It is important to note that on the right hand side of (2.13) the \mathbf{k} -dependent self-energy $\Sigma(\mathbf{k}, i\omega_n)$ of the full lattice model has been replaced by the purely local self-energy $\Sigma^{\text{imp}}(i\omega_n)$ of the effective impurity model. We will come back to this important point shortly.

¹We use the term impurity since solving a problem where particle interactions are restricted to a finite number of sites is often the case for models of systems with magnetic impurities.

In this section we have attempted to show some analogies between the DMFA and the Weiss mean-field approach to lattice problems. In the DMFA the bath Green function $\mathcal{G}_0(i\omega_n)$ plays a similar role to the Weiss effective field, where the spacial fluctuations are integrated, or *frozen* out. The important difference with the DMFA is that local quantum fluctuations between states are taken fully into account. The dynamics of these local state transitions as a function of imaginary time are described by $\mathcal{G}_0(\tau)$. The ingredients required in an effective Hamiltonian to describe the local problem must therefore include a hybridisation term, allowing electrons to come out of the bath onto the impurity site and return again to the bath, in addition to a term to describe the local interaction. If we equate the bath electrons with a conduction band and the impurity site with an impurity f-orbital electron, then we see that a general form of the single impurity Anderson model would provide a suitable Hamiltonian for our effective problem

$$H^{\text{SIAM}} = \sum_{i\sigma} \epsilon_i c_{i\sigma}^\dagger c_{i\sigma} + \sum_{i\sigma} V_i \left(c_{i\sigma}^\dagger f_\sigma + f_\sigma^\dagger c_{i\sigma} \right) + \epsilon_f \sum_{\sigma} f_\sigma^\dagger f_\sigma + U n_\uparrow^f n_\downarrow^f, \quad (2.14)$$

where the parameters ϵ_i and V_i would have to be chosen such that the model's non-interacting Green function

$$\mathcal{G}_0^{\text{SIAM}}(i\omega_m) = \frac{1}{(i\omega_m - \epsilon_f) - \frac{1}{N} \sum_i \frac{V_i^2}{i\omega_m - \epsilon_i}} \quad (2.15)$$

coincides with the effective \mathcal{G}_0 in (2.9). To make the link with impurity model Hamiltonians more concretely we may consider the skeleton diagrams of the self-energy diagrammatic perturbation expansion (where we follow the arguments presented in [29]).

The first few skeleton diagrams in the diagrammatic perturbation expansion for the Hubbard model (taken as an example) are given in Fig. 2.1. The double lines in the diagram represent the interacting Green function, which could also be decomposed into a sum of terms containing products of non-interacting Green functions. The non-interacting Green function propagator between sites i and j will give a power of t , the hopping matrix element, of $t^{|i-j|}$ with Manhattan distance $|i-j|$. This will then also be the lowest power of t present in the interacting Green function. In the limit of infinite dimensionality d , it is important to realise that the hopping matrix element must be rescaled as $t = t^*/\sqrt{d}$ in order to maintain a non-trivial model with finite kinetic energy per site. Now, a given vertex at site i in any diagram may be linked to a site j via P_{ij} independent paths along fully dressed propagators. Summing over j is equivalent to summing over the Manhattan distance $R = |i-j|$ and multiplying with the number of sites $N(R)$ found to be at that distance. Since $N(R)$ is just proportional to the dimension d then the total sum produces a term with a power of t of at least

$$t^{RP_{ij}} d^R \propto \left(\frac{1}{d}\right)^R \left(\frac{P_{ij}}{2} - 1\right). \quad (2.16)$$

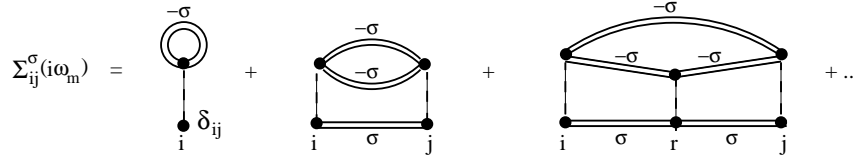


Figure 2.1: Diagrammatic perturbation expansion series for the Hubbard Model: The double lines are full interacting Green function propagators, and the diagrams are therefore the skeleton diagrams (figure taken from [29])

Just by considering the diagrams in the expansion we see that vertices at different sites i and j will always be joined by at least three independent paths, $P_{ij} \geq 3$ so that in the limit $d \rightarrow \infty$ such diagrams will tend to zero with a power law of at least $(1/\sqrt{d})^R$ and not contribute to the sum. Only local diagrams will survive in this limit, with all vertices carrying the same spacial index. We then note that a skeleton diagram perturbation expansion for the impurity site self-energy $\Sigma_{ff}(i\omega_n)$ of the single impurity Anderson model looks, order for order, exactly the same as for the Hubbard model, with all vertex indices labelled by the same site index (the impurity site). The topology of the skeleton diagrams just gives the functional form of the self-energy. We can therefore conclude that in the limit $d \rightarrow \infty$ the skeleton self-energy functional of the Hubbard model is the same as that of the SIAM.

$$\Sigma^{\text{Hubb.}}[\cdot] \equiv \Sigma^{\text{SIAM}}[\cdot]. \quad (2.17)$$

So we see that if the limit $d \rightarrow \infty$ is taken, then the self-consistent equations (2.10) and (2.13) become exact, since the above analysis has shown that the self-energy of the full lattice problem really is a local quantity whose functional form is the same as for the embedded impurity problem. We therefore have a method with the desired controllable limit of $d \rightarrow \infty$ which we refer to as DMFT, as opposed to the *approximation* of a local self-energy in lower dimensions, which is referred to as the dynamical mean-field approximation (DMFA). Assuming a local self-energy means we are neglecting even the shortest ranged spacial correlations. This is fine for problems where the main physics is of a local nature. The desire to gradually restore at least short ranged correlations can be achieved by a variety of proposals [30], collectively referred to as quantum cluster theories. In this work we use a variant of the dynamical cluster approximation (DCA). The DCA is best formulated in k -space. Looking back to the DMFA, a purely local self-energy is equivalent to assuming that the self-energy does not depend on \mathbf{k} . The DCA described in the next section gradually reintroduces the \mathbf{k} -dependence of the self-energy.

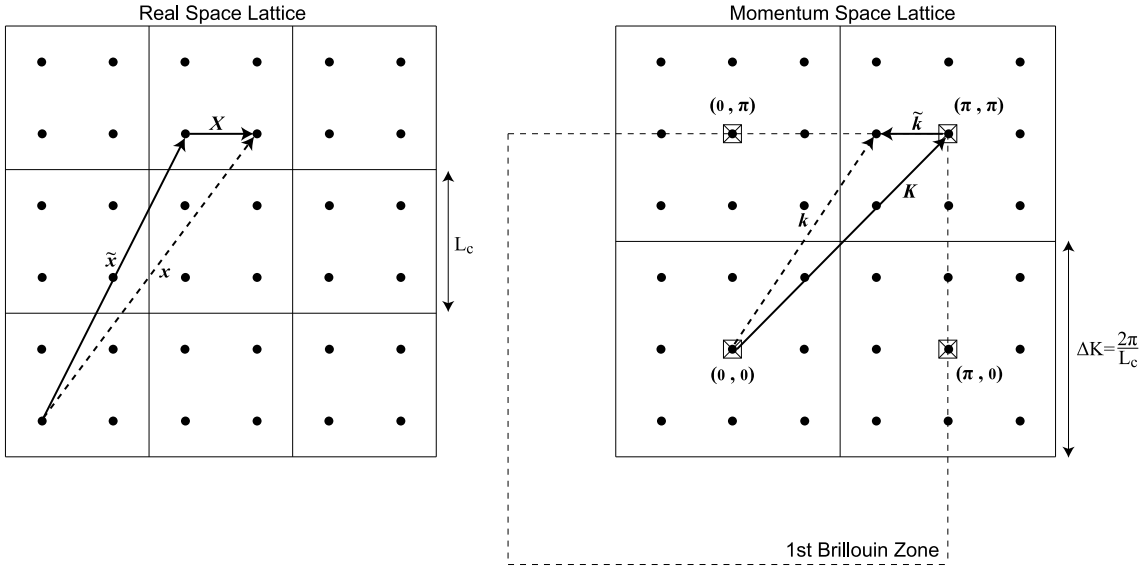


Figure 2.2: DCA is an approximation in k -space which in real space corresponds to understanding a lattice vector \mathbf{x} as an inter-cluster vector $\tilde{\mathbf{x}}$ plus an intra-cluster vector \mathbf{X} . In k -space, the example shows a cluster patching of the first BZ using $N_c = 4$: inside each patch around patch centres, \mathbf{K} , the self-energy is approximated as k -independent.

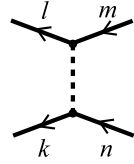
2.3 The Dynamical Cluster Approximation

The DCA is based on an underlying approximation to the self-energy of the full lattice problem. In the DMFA, the self-energy is assumed to be momentum independent so that for a given Matsubara frequency $i\omega_n$, it is constant across the whole Brillouin zone: $\Sigma(\mathbf{k}, i\omega_n) = \Sigma(i\omega_n)$. As already mentioned, in real-space this is equivalent to neglecting non-local correlations. The DCA begins to restore the k -dependency by defining smaller sized *patches* in momentum space in which the self-energy is constant for a given frequency. The self-energy for momenta in a neighbouring patch may take a different constant value for that frequency. We consider this, and the implications for the self-consistent equations, more formally below.

In momentum space a k -vector in the first Brillouin zone is described by a centre of patch vector \mathbf{K} and a vector $\tilde{\mathbf{k}}$ within the patch such that $\mathbf{k} = \tilde{\mathbf{k}} + \mathbf{K}$. In real space this can be equated to each site of the original lattice being described by a vector $\tilde{\mathbf{x}}$, which determines the origin of a given cluster, and an intra-cluster vector \mathbf{X} to point to one of the N_c sites within that cluster.

The reciprocal vector spaces to each other are therefore: $\tilde{\mathbf{x}} \leftrightarrow \tilde{\mathbf{k}}$ and $\mathbf{X} \leftrightarrow \mathbf{K}$. Fig. 2.2 illustrates the various vector definitions and divisions of momentum space and real space into patches and clusters.

In the language of Feynman diagrams, each vertex in a diagram represents an interaction term as follows



$$\equiv v(kl; nm) \frac{1}{\beta} \delta_{\omega_k + \omega_l, \omega_m + \omega_n},$$

where $v(kl; nm)$ is defined for the two-particle interaction of the model at hand, and the Kronecker delta just ensures energy conservation for the interaction. On the simple example of the Hubbard model, with on-site Coulomb interaction U , then

$$v(\mathbf{k}_m, \mathbf{k}_n; \mathbf{k}_l \mathbf{k}_p) = \frac{U}{N} \delta_{\mathbf{k}_m + \mathbf{k}_n, \mathbf{k}_l + \mathbf{k}_p} \delta_{\sigma_m \sigma_l} \delta_{\sigma_n \sigma_p} \delta_{\sigma_m, -\sigma_n} \quad (2.18)$$

$$= \frac{U}{N^2} (N \delta_{\mathbf{k}_m + \mathbf{k}_n, \mathbf{k}_l + \mathbf{k}_p}) \delta_{\text{spin}}, \quad (2.19)$$

where we use a short hand for the spin Kronecker deltas, $\delta_{\text{spin}} = \delta_{\sigma_m \sigma_l} \delta_{\sigma_n \sigma_p} \delta_{\sigma_m, -\sigma_n}$, which are there to restrict the on-site Coulomb interaction to spins of opposite signs (Pauli principle!) and forbid spin flips. The quantity in brackets is defined as the Laue function which can be written as

$$\Delta = N \delta_{\mathbf{k}_m + \mathbf{k}_n, \mathbf{k}_l + \mathbf{k}_p} = \sum_i e^{i \mathbf{r}_i (\mathbf{k}_m + \mathbf{k}_n - \mathbf{k}_l - \mathbf{k}_p)} \quad (2.20)$$

and which imposes strict conservation of momentum on the interaction process given by the vertex.

The basic approximation in the DCA is an approximation to the Laue function:

$$\Delta_{\text{DCA}} = N_c \delta_{M(\mathbf{k}_m) + M(\mathbf{k}_n), M(\mathbf{k}_l) + M(\mathbf{k}_p)}, \quad (2.21)$$

where $M(\mathbf{k})$ is a function which maps the momentum \mathbf{k} to the cluster momentum \mathbf{K} at the centre of the patch in which \mathbf{k} is found. In formulae, and using the same symbolism for the vectors as in Fig. 2.2, i.e. for an original lattice momentum vector $\mathbf{k} = \mathbf{K} + \tilde{\mathbf{k}}$, we have

$$M(\mathbf{k}) = M(\mathbf{K} + \tilde{\mathbf{k}}) = \mathbf{K}. \quad (2.22)$$

When inserted into the vertex interaction the DCA Laue function results in a relaxation of strict momentum conservation since momentum is now only approximately conserved, in fact, with a tolerance equal to the size of a patch. We see that this approximation easily allows a smooth transition between the simplest case with $N_c = 1$ and the limit $N_c = N$, the size of the original lattice. For $N_c = 1$ all \mathbf{k} -vectors are mapped to a single momentum, the self-energy becomes momentum independent, and we obtain the DMFA. For $N_c = N$ we would recover full momentum dependence and the solution would be exact:

$$\Delta_{\text{DCA}} \xrightarrow{N_c \rightarrow 1} \Delta_{\text{DMFA}} \quad (2.23)$$

$$\Delta_{\text{DCA}} \xrightarrow{N_c \rightarrow N} \Delta_{\text{exact}}. \quad (2.24)$$

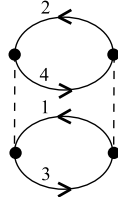


Figure 2.3: A typical second-order diagrammatic perturbation term in the Baym-Kadanoff generating functional Φ . Per definition of Φ , as a skeleton expansion, the full lines represent full interaction Green functions. The numbered labelling of these propagators represents the momentum, Matsubara frequency and spin of the propagator. For example, $1 \equiv (\mathbf{k}_1, i\omega_1, \sigma_1)$

In order to guarantee a thermodynamically consistent approximation, in which a quantity calculated as a derivative of the grand potential Ω agrees with the result calculated via the Green function G , the grand potential must be stationary with respect to G :

$$\frac{\delta\Omega}{\delta G} = 0. \quad (2.25)$$

To meet this condition it is sufficient that the single-particle self-energy $\Sigma = G_0^{-1} - G^{-1}$ can be obtained from the Baym-Kadanoff generating functional Φ [31, 32] via functional derivation:

$$\Sigma = \frac{\delta\Phi[G]}{\delta G}. \quad (2.26)$$

The generating functional $\Phi = \Phi[G, v]$ is defined as the sum of all topologically different, closed, skeleton diagrams constructed with the full interacting Green function G , as propagating/non-propagating lines, and any number of interaction vertices v .

To demonstrate the effect of replacing the exact momentum conserving Laue function Δ with the DCA Laue function Δ_{DCA} we consider explicitly a second order diagram term in Φ and assume a local Coulomb interaction U at the vertices as represented in Fig. 2.3.

This diagram is translated into a mathematical formula according to the Feynman rules:

1. Each dotted line represents an interaction vertex, which we take to be the on-site Coulomb interaction, as given in (2.19) together with the preceding diagram of the vertex.
2. Full lines $\equiv -G_{\mathbf{k}_i}(i\omega_i)$.
3. Extra factor for non-propagating lines (where a full line enters and leaves the same vertex): $e^{i\omega_n 0^+}$.
4. Include a factor $(-1)^n \frac{\epsilon^S}{h(\theta)}$ where n is the perturbation order (number of vertices in the diagram), $\epsilon = -1$ (1) for fermions (bosons), S is the number of closed propagator loops, and $h(\theta)$ is the topology factor.

5. Summation over all internal momenta and all internal Matsubara energies (which will mean summing over all \mathbf{k} and ω variables here since all diagrams in the generating functional Φ are, per definition, closed diagrams).

Fig. 2.3 therefore translates to

$$\sum_{\mathbf{k}_1, \mathbf{k}_2, \mathbf{k}_3, \mathbf{k}_4} \sum_{\omega_1, \omega_2, \omega_3, \omega_4} \frac{(-1)^n \epsilon^n U^2}{h(\theta) N^4} (N \delta_{\mathbf{k}_1 + \mathbf{k}_2, \mathbf{k}_3 + \mathbf{k}_4})^2 \frac{1}{\beta^2} (\delta_{\omega_1 + \omega_2, \omega_3 + \omega_4})^2 \times \\ \times \delta_{\text{spin}} (-G_{\mathbf{k}_1}(i\omega_1)) (-G_{\mathbf{k}_2}(i\omega_2)) (-G_{\mathbf{k}_3}(i\omega_3)) (-G_{\mathbf{k}_4}(i\omega_4)). \quad (2.27)$$

We now make the approximation to the Laue function, i.e. $\Delta \rightarrow \Delta_{\text{DCA}}$, so that

$$N \delta_{\mathbf{k}_1 + \mathbf{k}_2, \mathbf{k}_3 + \mathbf{k}_4} \rightarrow N_c \delta_{M(\mathbf{K}_1 + \tilde{\mathbf{k}}_1) + M(\mathbf{K}_2 + \tilde{\mathbf{k}}_2), M(\mathbf{K}_3 + \tilde{\mathbf{k}}_3) + M(\mathbf{K}_4 + \tilde{\mathbf{k}}_4)} \quad (2.28)$$

$$= N_c \delta_{\mathbf{K}_1 + \mathbf{K}_2, \mathbf{K}_3 + \mathbf{K}_4}. \quad (2.29)$$

The sums over momenta can be split up as $\sum_{\mathbf{k}_i} = \sum_{\mathbf{K}_i, \tilde{\mathbf{k}}_i}$, where now the sums over momenta vectors $\tilde{\mathbf{k}}_i$ inside a patch are not subject to a momentum conserving Kronecker delta. With a shorthand notation for the energies Kronecker delta, $\delta_{\text{energies}} = \delta_{\omega_1 + \omega_2, \omega_3 + \omega_4}$, the diagram term becomes

$$\sum_{\mathbf{K}_1, \mathbf{K}_2, \mathbf{K}_3, \mathbf{K}_4} \sum_{\omega_1, \omega_2, \omega_3, \omega_4} \frac{(-1)^n \epsilon^n U^2}{\beta^2 h(\theta) N_c^2} \delta_{\mathbf{K}_1 + \mathbf{K}_2, \mathbf{K}_3 + \mathbf{K}_4} \delta_{\text{spin}} \delta_{\text{energies}} \times \\ \times \left(-\frac{N_c}{N} \sum_{\tilde{\mathbf{k}}_1} G_{\mathbf{K}_1 + \tilde{\mathbf{k}}_1}(i\omega_1) \right) \left(-\frac{N_c}{N} \sum_{\tilde{\mathbf{k}}_2} G_{\mathbf{K}_2 + \tilde{\mathbf{k}}_2}(i\omega_2) \right) \times \\ \times \left(-\frac{N_c}{N} \sum_{\tilde{\mathbf{k}}_3} G_{\mathbf{K}_3 + \tilde{\mathbf{k}}_3}(i\omega_3) \right) \left(-\frac{N_c}{N} \sum_{\tilde{\mathbf{k}}_4} G_{\mathbf{K}_4 + \tilde{\mathbf{k}}_4}(i\omega_4) \right). \quad (2.30)$$

We define a *coarse-grained* Green function

$$\bar{G}_{\mathbf{K}}(i\omega) = \frac{N_c}{N} \sum_{\tilde{\mathbf{k}}} G_{\mathbf{K} + \tilde{\mathbf{k}}}(i\omega) \quad (2.31)$$

as the average over the patch momentum vectors of the full lattice in that patch, so that translating the mathematical expression back into a diagram gives exactly the same figure as to start with but where now each full line represents a coarse-grained Green function $\bar{G}_{\mathbf{K}}$. On this example for a typical diagram in the expansion for Φ , we note that, now, the only summation left is over the small number (N_c) of centre of patch vectors \mathbf{K}_i such that the exact same diagrams and terms to be summed up would have been obtained by considering the skeleton diagram perturbation expansion for a simple cluster of N_c lattice sites with corresponding N_c cluster momentum vectors \mathbf{K}_i in reciprocal space. This is under the condition that the full interacting Green function G^c for such a cluster is equal to the coarse-grained Green function of the lattice. Now, since the self-energy can be

generated from the Φ -functional, we see that the approximation to the Laue function is equivalent to an approximation to the self-energy of the lattice: The skeleton self-energy of the lattice has the same functional form as that of an N_c -site cluster, but the argument of the functional (or in other words, each full propagator line in the Feynman diagrams) is equal to the coarse-grained Green function of the lattice itself.

In formulae we have for the DCA lattice Green function

$$G_{\mathbf{k}}(i\omega_n) = \frac{1}{G_{\mathbf{k}}^0(i\omega_n)^{-1} - \Sigma^c(\mathbf{K}, i\omega_n)}, \quad (2.32)$$

whereby $M(\mathbf{k}) = \mathbf{K}$. The task is therefore to calculate the self-energy for an *effective* cluster model, in the sense that the interacting Green function for this cluster model must be equal to the DCA coarse-grained Green function of the lattice model. The Dyson equation for this case gives

$$\Sigma^c(\mathbf{K}, i\omega_n) = \mathcal{G}_{\mathbf{K}}^0(i\omega_n)^{-1} - \bar{G}_{\mathbf{K}}(i\omega_n)^{-1}, \quad (2.33)$$

in which we define \mathcal{G}^0 as the non-interacting Green function of the effective cluster Hamiltonian. In the same way as in the DMFT this function may be seen as including the integrated-out effects of dynamical fluctuation interactions with the bath of electrons surrounding the real-space cluster. One also speaks of *cluster-excluded* bath Green function, to indicate that interactions on the cluster itself have yet to be included via the cluster self-energy Σ^c . The functional form of the self-energy is known: it is that of an N_c -site interacting cluster. We therefore need only find some suitable *cluster solver* capable of producing the corresponding interacting Green function to a given non-interacting (bath) Green function in order to extract the self-energy via (2.33). In this work we use a relevant implementation [33] of the Hirsch-Fye QMC impurity algorithm [34] as cluster solver. The set of equations (2.32) and (2.33), taken together with the definition of the coarse-grained Green function (2.31), then represent a closed set of equations which must be solved self-consistently for the lattice function $G_{\mathbf{k}}(i\omega_n)$. To this end we use the following iterative solution system:

1. Make an initial guess for the bath Green function \mathcal{G}^0 .
2. With \mathcal{G}^0 as input, use the QMC cluster solver to calculate the corresponding interacting Green function, which we define as $G_{\mathbf{K}}^c$.
3. calculate the cluster self-energy with

$$\Sigma^c(\mathbf{K}, i\omega_n) = \mathcal{G}_{\mathbf{K}}^0(i\omega_n)^{-1} - G_{\mathbf{K}}^c(i\omega_n)^{-1}. \quad (2.34)$$

4. Use the self-energy to calculate the coarse-grained Green function of the lattice:

$$\bar{G}_{\mathbf{K}}(i\omega) = \frac{N_c}{N} \sum_{\tilde{\mathbf{k}}} \frac{1}{i\omega_n - (\epsilon(\mathbf{K} + \tilde{\mathbf{k}}) - \mu) - \Sigma^c(\mathbf{K}, i\omega_n)}. \quad (2.35)$$

5. Check for convergence of the scheme: The self-consistent equations are solved if the coarse-grained Green function \bar{G} is equal to the interacting Green function of the cluster G^c .
6. If not converged, then calculate a new improved estimate for the bath Green function by excluding the interactions on the cluster via

$$\mathcal{G}_{\mathbf{K}}^0(i\omega_n)^{-1} = \bar{G}_{\mathbf{K}}(i\omega_n)^{-1} + \Sigma^c(\mathbf{K}, i\omega_n) \quad (2.36)$$

and go back to step 2.

In practice we have often considered the convergence of certain observables, for example the staggered magnetisation of the f-electrons and the c-electron occupancy, which we are interested in, measured during the QMC cluster solver part of the cycle at each iteration step, as a convenient test of whether or not a self-consistent solution has been reached. Checks are then subsequently made to confirm that the coarse-grained Green function is equal to the interacting cluster Green function within the QMC error bars. The start point for a new simulation will in general be a non-interacting Green function or, in order to speed up the convergence, we often use the DCA result of a neighbouring simulation in parameter space.

We note that the coarse-graining and Dyson equation are applied to the Green functions as a function of Matsubara frequencies. However, the QMC algorithm works on functions of discrete imaginary times. Therefore an efficient method for Fourier transform between the two representations is necessary. For the transform from Matsubara frequency to imaginary time,

$$G(\tau) = \frac{1}{\beta} \sum_{n=-\infty}^{\infty} e^{-i\omega_n\tau} G(i\omega_n), \quad (2.37)$$

we calculate the Matsubara sum up to a cut-off frequency and take account of the remaining terms by fitting to the asymptotic behaviour of Matsubara Green function [29].

The transform from imaginary time to frequencies is much more problematic. With the aid of the single particle spectral function $A(\omega) = -\frac{1}{\pi} \Im G^{ret}(\omega)$ we can write the desired Green function as

$$G(i\omega_n) = \int d\omega \frac{A(\omega)}{i\omega_n - \omega}. \quad (2.38)$$

To find the spectral function we can attempt to invert the spectral representation of the imaginary time Green function

$$G(\tau) = - \int d\omega A(\omega) \frac{e^{-\tau\omega}}{1 + e^{\beta\omega}}, \quad (2.39)$$

which proves so difficult since we know the value of $G(\tau)$ only at each discrete Trotter time slice. The inversion is an ill-defined problem since many possible spectral functions would produce a $G(\tau)$ which is consistent with the statistical error of the measured $G(\tau)$. Similar to the method used in reference [29] we draw on methods of Maximum Entropy, based on Bayesian probability, to define a ‘most likely’ spectral function, given the data and any pre-knowledge of the solution, whilst minimising the amount of artificial structure, i.e. finding the solution with maximum information entropy given the aforementioned constraints. In our implementation, we now favour the so-called stochastic analytic continuation approach [35], of which the Maximum Entropy method is a special limit [36].

2.4 Broken Symmetry DCA

The DCA described in the previous is capable of capturing spacial correlations where the correlation length is less than the size of the cluster in real-space. However, broken spin symmetry phases are suppressed since we work with a unit cell containing only one site. During the iterative solution process the spin-up and spin-down Green functions of the lattice, calculated at each iteration step, will not be equal to each other if the system parameters are such as to cause AF ordering. The spin-up and spin-down functions must be averaged after each QMC iteration step in order to restore the translational symmetry assumed through definition of the lattice vectors. If a given parameter set $J/t, \mu, \beta t$ would produce a spin-symmetry broken solution, then this artificial restoration of spin-symmetry means that our self-consistent solution would not be correct. With this standard DCA approach, which is fine for paramagnetic regions of parameter space, we are therefore unable to enter magnetically ordered regions of the phase diagram of the KLM. Our approach to this problem has been to develop a new implementation of the DCA in which we define a larger unit cell capable of accommodating broken spin-symmetry.

We note that spin susceptibility measurements, within even the standard implementation of the DCA, could be used to indicate an AF phase transition, since we need only look for a closing of the spin-gap and corresponding divergence of the static spin susceptibility. However, such two-particle correlation functions have been seen to be particularly difficult to measure within the DCA approach [37], since they involve the inversion of a Bethe-Salpeter equation for the two-particle correlation function, which is a function of three momentum indices and three Matsubara frequencies. We remember that the QMC cluster solver however works in real-space and imaginary time. A recent publication made attempts towards calculating susceptibilities by approximating the full irreducible two-particle vertex by an effective vertex dependent on the momentum and frequency of the spin and/or charge excitation [38]. Our broken spin symmetry DCA here allows recognition of the phase transition simply by reading out a QMC measurement of the

single-particle staggered magnetic moment for the f-electrons once a self-consistent solution to the DCA equations has been reached. Additionally, simulations within the AF ordered phase now become accessible. As a final remark before defining our symmetry breaking implementation of DCA we point out that work is currently underway towards resolving the difficulties in calculating two-particle correlations within the DCA [39]. The new approach involves calculating susceptibility functions and the component Green functions $G(i\omega_m)$ in Matsubara frequencies directly at each QMC step in the DCA algorithm instead of first calculating $G(\tau)$, obtaining the spectral function $A(\omega)$ via the stochastic Maximum Entropy method [35, 36] and subsequently calculating $G(i\omega) = \int d\omega \frac{A(\omega)}{i\omega_m - \omega}$.

2.4.1 Symmetry breaking DCA definitions

We will always refer to the original lattice as meaning the real-space lattice formed by the basis vectors

$$\mathbf{a}_x = a \begin{pmatrix} 1 \\ 0 \end{pmatrix}, \quad \mathbf{a}_y = a \begin{pmatrix} 0 \\ 1 \end{pmatrix} \quad (2.40)$$

and a unit cell consisting of a single lattice point. The lattice constant is a , which we will set equal to one in applications but retain here for clarity of the definitions. The smallest unit cell with which we can capture AF symmetry breaking consists of two, neighbouring, original lattice sites. We label each site within a unit cell with a vector \mathbf{r}_μ i.e.

$$\mathbf{r}_1 = \begin{pmatrix} 0 \\ 0 \end{pmatrix}, \quad \mathbf{r}_2 = a \begin{pmatrix} 1 \\ 0 \end{pmatrix}. \quad (2.41)$$

This unit cell is represented by the dotted lines in Fig. 2.4, on which we also show all the other real-space lattice vectors defined in this section.

The superlattice of the two-site unit cell is created with basis vectors

$$\mathbf{a}_1 = a \begin{pmatrix} 1 \\ 1 \end{pmatrix}, \quad \mathbf{a}_2 = a \begin{pmatrix} 1 \\ -1 \end{pmatrix} \quad (2.42)$$

and the lattice constant of this 45°-tilted lattice is $\alpha = |\mathbf{a}_1| = |\mathbf{a}_2| = a\sqrt{2}$. Points on this translationally invariant superlattice are described by $\mathbf{x} = m\mathbf{a}_1 + n\mathbf{a}_2$ with whole numbers m and n . The reciprocal lattice vectors to this superlattice are therefore given by

$$\mathbf{G} = m\mathbf{b}_1 + n\mathbf{b}_2 \quad (2.43)$$

where the reciprocal basis vectors are

$$\mathbf{b}_1 = \frac{\pi}{a} \begin{pmatrix} 1 \\ 1 \end{pmatrix}, \quad \mathbf{b}_2 = \frac{\pi}{a} \begin{pmatrix} 1 \\ -1 \end{pmatrix} \quad (2.44)$$

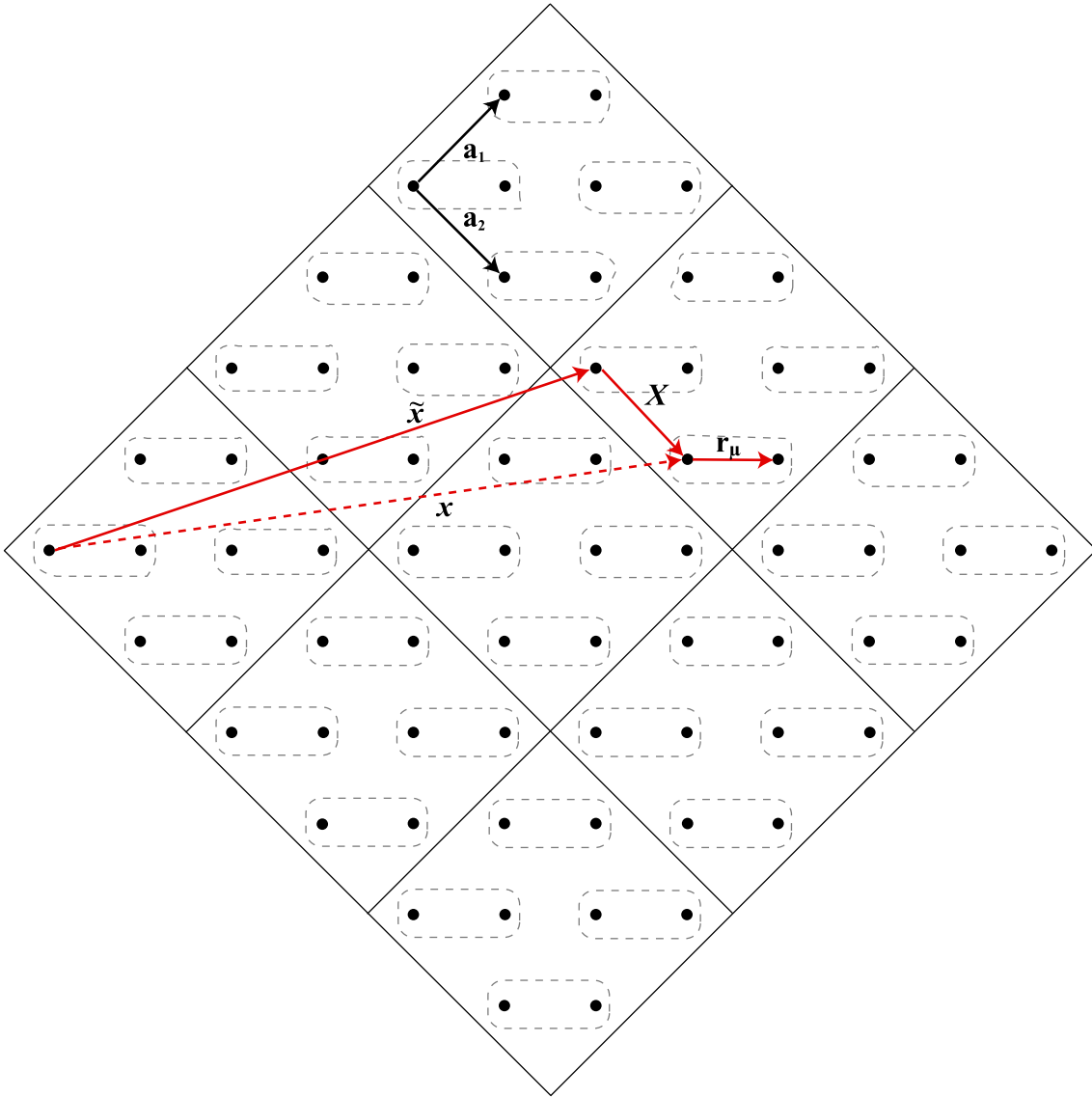


Figure 2.4: Demonstration of the relations between, and definitions of: the unit cells (dotted lines), orbital vectors \mathbf{r}_μ in the unit cell, primitive lattice vectors \mathbf{a}_1 , \mathbf{a}_2 , lattice vectors \mathbf{x} , cluster superlattice $\tilde{\mathbf{x}}$ and intra-cluster vectors \mathbf{X} .

such that $\mathbf{a}_i \cdot \mathbf{b}_i = 2\pi\delta_{ij}$ is fulfilled. If L is the linear size of the superlattice (which is taken large enough to ensure the thermodynamic limit) and this superlattice is thought of as periodically repeated in space, then a fine mesh of discrete k values is created in momentum space. With $\mathbf{k} = m\frac{\mathbf{b}_1}{L} + n\frac{\mathbf{b}_2}{L}$ and $m, n \in [\frac{L}{2} + 1, \frac{L}{2}]$ we denote an element of the Brillouin zone of the superlattice of the unit cells. We will periodically refer to this Brillouin zone as the magnetic Brillouin zone (MBZ), which is exactly half the size of the original BZ and tilted through 45° .

Within the spirit of a real-space formulation of the DCA we now define a cluster of $N_c^{AF} = 4$ unit cells in real-space, using the index AF to indicate that it is a cluster of, in this example, four 2-site (AF) unit cells. To be sure of what is meant, this cluster contains eight original lattice points equating to a total of 16 orbitals since each lattice site has space for one f-electron and one c-electron. Obviously, in the context of the QMC cluster solver used, where the computational time scales with the number of orbitals to the cubed (see section 3.2.1), this is a large number of orbitals, such that $N_c^{AF} = 4$ was the largest cluster considered in this work. The main portion of our results refer to a ‘‘cluster’’ of size $N_c^{AF} = 1$ which nevertheless still contains four orbitals. However, we continue to demonstrate the formalism on the larger cluster for non-trivial generality. As before, within the standard DCA formulism, we use $\tilde{\mathbf{x}} = mL_c\mathbf{a}_1 + nL_c\mathbf{a}_2$ to denote the location of a cluster in real-space, with $L_c = \sqrt{N_c^{AF}} = 2$ being the linear size of the cluster in units of the lattice constant α of the superlattice of unit cells. The reciprocal lattice to the superlattice $\tilde{\mathbf{x}}$ of the real-space clusters is given by $\mathbf{K} = m\frac{\mathbf{b}_1}{L_c} + n\frac{\mathbf{b}_2}{L_c}$. Those such reciprocal vectors within the MBZ are the cluster momentum vectors of the DCA. An element of the Brillouin zone of the superlattice of the cluster is defined by a vector $\tilde{\mathbf{k}}$. These momentum vectors therefore define the vectors in the patch around the cluster vector \mathbf{K} for which the approximation of a k-independent self-energy is made. In summary of the above, in momentum space, any vector \mathbf{k} in the MBZ can be decomposed into a cluster (centre of patch) vector \mathbf{K} and a patch vector $\tilde{\mathbf{k}}$:

$$\mathbf{k} = \mathbf{K} + \tilde{\mathbf{k}}. \quad (2.45)$$

Additionally, a vector $\bar{\mathbf{k}}$ in the BZ of the original lattice can be written as

$$\bar{\mathbf{k}} = \mathbf{k} + \mathbf{G} \quad (2.46)$$

with suitably chosen \mathbf{G} as defined in (2.43). The relationship between the various types of k-vectors and an example of the patching used in the MBZ when using the cluster size $N_c^{AF} = 4$ is shown in Fig. 2.5.

2.4.2 Broken Symmetry DCA Self-Consistent Equations

With the above definitions, introduced to cope with broken spin-symmetry between nearest neighbours in the original lattice, we now consider the implications for the DCA self-

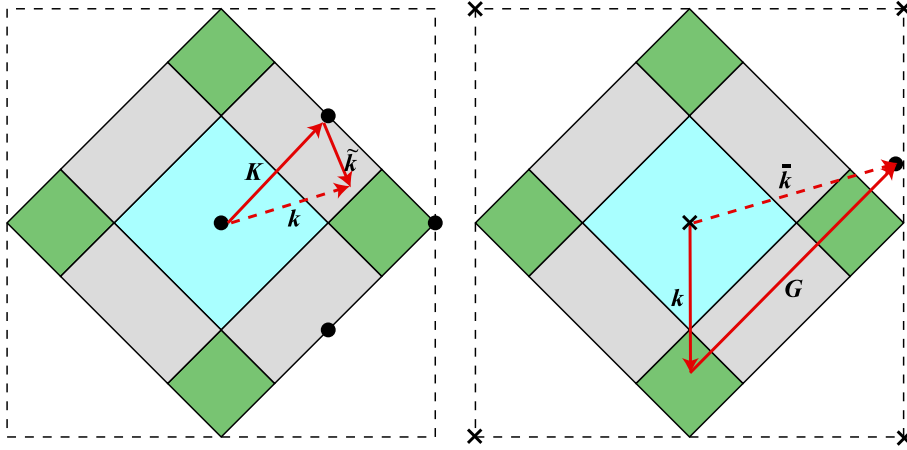


Figure 2.5: Demonstration of the DCA patching in momentum space that we use when $N_c^{AF} = 4$. Left: a vector \mathbf{k} within the MBZ can be decomposed into a centre-of-patch vector \mathbf{K} , which is a reciprocal lattice vector to the cluster superlattice in real-space, and a vector $\tilde{\mathbf{k}}$ within the patch. Right: A vector $\tilde{\mathbf{k}}$ within the BZ of the original lattice can be decomposed into a vector \mathbf{k} within the MBZ plus a vector \mathbf{G} , which is a reciprocal lattice vector to the basis vectors $\mathbf{a}_1, \mathbf{a}_2$ in real-space.

consistent equations. The aim is to write an expression for the lattice Green function on which the DCA can be applied. We will see that when the unit cell contains more than one lattice site we will obtain a matrix equation for the Green function to reflect the different orbitals in the real-space unit cell.

To begin with we consider the non-interacting Green function starting with a non-interacting Hamiltonian consisting only of a general hopping term. A given site in the original lattice is described by a pair of vectors $(\mathbf{x}, \mathbf{r}_\mu)$, which gives the position of the unit cell in the superlattice of unit cells, and the position of the site within the unit cell, respectively. Using real-space creation and annihilation operators using these indices, and hopping $t_{\mathbf{x}\mu; \mathbf{y}\nu}$ between the given sites, the Hamiltonian is written as

$$H_0 = \sum_{\mathbf{x}\mu, \mathbf{y}\nu} c_{\mathbf{x}, \mathbf{r}_\mu}^\dagger t_{\mathbf{x}\mu; \mathbf{y}\nu} c_{\mathbf{y}, \mathbf{r}_\nu}. \quad (2.47)$$

We restrict ourselves for the moment to nearest neighbour hopping (with amplitude t) on a square lattice and use the two-site unit cell and vector definitions given in section 2.4.1. For a given site there are four hopping possibilities: one takes place within the same unit cell, and the remaining three go into one of the neighbouring cells. Alternatively, referring to Fig. 2.6 we can choose a particular cell and write down the hopping processes relating to the sites within that cell, whilst being careful to avoid overcounting of equivalent hopping

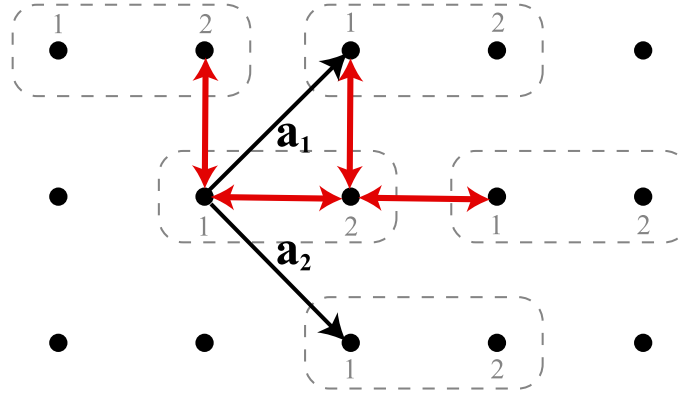


Figure 2.6: The possible hopping processes onto and off of a given unit cell and between the orbitals of that cell are shown as red arrows in the diagram. Hopping possibilities in the direction to the left of the cell or below it are already counted due to the assumed translational symmetry of the lattice with primitive vectors \mathbf{a}_1 , \mathbf{a}_2 .

processes under translation.

$$H_0 = -t \sum_{\mathbf{x}} \left[c_{\mathbf{x},r_1}^\dagger c_{\mathbf{x},r_2} + c_{\mathbf{x},r_1}^\dagger c_{\mathbf{x}-\mathbf{a}_2,r_2} + c_{\mathbf{x},r_2}^\dagger c_{\mathbf{x}+\mathbf{a}_1,r_1} + c_{\mathbf{x},r_2}^\dagger c_{\mathbf{x}+\mathbf{a}_1+\mathbf{a}_2,r_1} + \text{h.c.} \right]. \quad (2.48)$$

We can Fourier transform with respect to the superlattice of unit cells using

$$c_{\mathbf{x},r_\mu} = \sqrt{\frac{2}{N}} \sum_{\mathbf{k}} e^{i\mathbf{k}\mathbf{x}} c_{\mathbf{k},r_\mu}. \quad (2.49)$$

The result can be written as

$$H_0 = -t \sum_{\mathbf{k}} \begin{pmatrix} c_{\mathbf{k},r_1}^\dagger & c_{\mathbf{k},r_2}^\dagger \end{pmatrix} \begin{pmatrix} 0 & z \\ z^* & 0 \end{pmatrix} \begin{pmatrix} c_{\mathbf{k},r_1} \\ c_{\mathbf{k},r_2} \end{pmatrix} \quad (2.50)$$

where

$$z = \left(1 + e^{-i\mathbf{k}\mathbf{a}_1}\right) \left(1 + e^{-i\mathbf{k}\mathbf{a}_2}\right) \quad (2.51)$$

and z^* is just the complex conjugate. The generalisation to a formulation with an N_b -site unit cell is just

$$H_0 = \sum_{\mathbf{k}} \sum_{\mu\nu} c_{\mathbf{k},r_\mu}^\dagger \hat{Z}(\mathbf{k})_{\mu\nu} c_{\mathbf{k},r_\nu} \quad (2.52)$$

where the $N_b \times N_b$ matrix \hat{Z} is the Fourier transform (to k -vectors in the first Brillouin zone of the superlattice formed by the basis vectors appropriate to the definition of the

unit cell) of the hopping $t_{\mathbf{x}\mu;\mathbf{y}\nu}$. In other words it is a matrix form for the free dispersion $\epsilon(\mathbf{k})$ where the row and column indices stand for the different spacial orbitals in the unit cell. We note each element on the diagonal of the matrix represents hopping from an orbital at a certain position in a first unit cell onto an orbital with the same position in another unit cell. For our specific case, with an $N_b = 2$ AF-unit cell, the inclusion of next-nearest neighbour hopping, taking place in directions \mathbf{a}_1 and \mathbf{a}_2 , would give rise to non-zero diagonal elements in \hat{Z} . We discuss the inclusion of these diagonal hopping processes at the end of section 5.1.

In principle at least, using larger unit cells would mean that the type of ordering must not be anticipated. So whether it be AF or some more complicated spiral ordered spin phase is of no consequence: if one period of the order fits onto the unit cell then it would show up naturally. In practice though, increasing the cluster size is linked with a large increase in the computational time required for a simulation. The bottleneck of the iterative solution technique is the QMC cluster solver, in which the time scales with the total number of orbitals within the cluster to the power of three.

Continuing the derivation we write (2.52) as

$$H_0 = \sum_{\mathbf{k}} \vec{c}_{\mathbf{k}}^\dagger \hat{Z}(\mathbf{k}) \vec{c}_{\mathbf{k}} \quad (2.53)$$

with $\vec{c}_{\mathbf{k}} = \left(c_{\mathbf{k},\mathbf{r}_1} \cdots c_{\mathbf{k},\mathbf{r}_{N_b}} \right)^T$. We can bring this equation in diagonal form with respect to the orbital indices by inserting suitable unitary matrices $U_{\mathbf{k}}$:

$$H_0 = \sum_{\mathbf{k}} \vec{c}_{\mathbf{k}}^\dagger U_{\mathbf{k}} U_{\mathbf{k}}^\dagger \hat{Z}(\mathbf{k}) U_{\mathbf{k}} U_{\mathbf{k}}^\dagger \vec{c}_{\mathbf{k}} \quad (2.54)$$

$$= \sum_{\mathbf{k}} \vec{\gamma}_{\mathbf{k}}^\dagger \hat{\lambda}(\mathbf{k}) \vec{\gamma}_{\mathbf{k}}. \quad (2.55)$$

Here we have defined the diagonal matrix

$$\hat{\lambda}(\mathbf{k}) = U_{\mathbf{k}}^\dagger \hat{Z}(\mathbf{k}) U_{\mathbf{k}} \quad (2.56)$$

with the eigenvalues of $\hat{Z}(\mathbf{k})$ as its elements, and

$$\vec{\gamma}_{\mathbf{k}}^\dagger = \vec{c}_{\mathbf{k}}^\dagger U_{\mathbf{k}} \quad ; \quad \vec{\gamma}_{\mathbf{k}} = U_{\mathbf{k}}^\dagger \vec{c}_{\mathbf{k}} \quad (2.57)$$

are composite fermionic operators for which H_0 is diagonal. We further define the non-interacting Green function matrix $\hat{G}_{\mathbf{k}}^0(i\omega_m)$ containing elements

$$\left\{ \hat{G}_{\mathbf{k}}^0(i\omega_m) \right\}_{\mu\nu} = \int_0^\beta d\tau e^{i\omega_m\tau} \langle T c_{\mathbf{k},\mathbf{r}_\mu}(\tau) c_{\mathbf{k},\mathbf{r}_\nu}^\dagger(0) \rangle \quad (2.58)$$

and calculate this matrix after unitary transformation with $U_{\mathbf{k}}$:

$$\left\{ U_{\mathbf{k}}^\dagger \hat{G}_{\mathbf{k}}^0(i\omega_m) U_{\mathbf{k}} \right\}_{ij} = \int_0^\beta d\tau e^{i\omega_m\tau} \langle T \left(U_{\mathbf{k}}^\dagger \right)_{i\mu} c_{\mathbf{k},\mathbf{r}_\mu}(\tau) c_{\mathbf{k},\mathbf{r}_\nu}^\dagger(0) \left(U_{\mathbf{k}} \right)_{\nu j} \rangle \quad (2.59)$$

$$= \left\{ \left[i\omega_m \mathbb{1} - \hat{\lambda}_{\mathbf{k}} \right]^{-1} \right\}_{ij}. \quad (2.60)$$

The Green function matrix is now given by

$$\hat{G}_{\mathbf{k}}^0(i\omega_m) = U_{\mathbf{k}} \left[i\omega_m \mathbb{1} - \hat{\lambda}_{\mathbf{k}} \right]^{-1} U_{\mathbf{k}}^\dagger \quad (2.61)$$

$$= \left[U_{\mathbf{k}} (i\omega_m \mathbb{1} - \hat{\lambda}_{\mathbf{k}}) U_{\mathbf{k}}^\dagger \right]^{-1} \quad (2.62)$$

$$= \left[i\omega_m \mathbb{1} - \hat{Z}_{\mathbf{k}} \right]^{-1}. \quad (2.63)$$

It is then logical to include interactions via a self-energy matrix $\hat{\Sigma}(\mathbf{k}, i\omega_m)$ which effectively renormalises the hopping processes between orbitals such that the dispersion matrix would be modified. The full interacting Green function is then

$$\hat{G}_{\mathbf{k}}(i\omega_m) = \left[i\omega_m \mathbb{1} - \hat{Z}_{\mathbf{k}} - \hat{\Sigma}(\mathbf{k}, i\omega_m) \right]^{-1} \quad (2.64)$$

$$= \left[\hat{G}_{\mathbf{k}}^0(i\omega_m)^{-1} - \hat{\Sigma}(\mathbf{k}, i\omega_m) \right]^{-1}. \quad (2.65)$$

Now we may define the DCA patches in k-space (the patching must take place in the true BZ of the superlattice of the unit cells; i.e. the MBZ) and make the approximation to the Laue function as before in the standard DCA approach (see section 2.3) to arrive at the corresponding matrix-equation equivalents to the self-consistent equations (2.32), (2.33), and the coarse-grained Green function (2.31). When defining the geometry of the cluster in k-space it is important to preserve the point symmetry of the underlying lattice problem. Thus it is ensured that equivalent points in k-space are mapped to the same cluster momentum via the mapping function $M(\mathbf{k})$ [37].

In this work we have solved these equations for the KLM, defining for our purpose, a two-site unit cell. This cell actually contains four orbitals corresponding to two itinerant c-electron sites and two localised f-electron sites. The self-consistent equations therefore involve 4×4 matrices for the Green functions. However, the KLM enforces single occupancy on the f-sites and those elements $\hat{G}_{\mu\nu}$ which correspond to propagation between f-sites and c-sites are zero. \hat{G} is therefore block diagonal, with two non-zero submatrices corresponding to the c-sites and f-sites, respectively. Due to this, the DCA matrix equations can be decomposed into matrix equations of dimension 2×2 so that the f and c sectors may be handled separately from each other. Further, in the f-sector the submatrix will be diagonal and its elements independent of \mathbf{k} since we know that the lattice Green function for the f-electrons must be purely local and non-propagating. This means that already at the first iteration step of the iterative solution process, the QMC result for the interacting cluster Green function for the f-electrons is the correct result for the lattice.

To see this we first point out that in general, after convergence to a self-consistent solution has been reached, local quantities measured on the cluster while the QMC cluster solver runs will be equal to the same quantity on the lattice [37]. Now, our initial ‘‘guess’’ for the non-interacting f-electron sector of the bath (cluster excluded) Green function matrix

will simply be to set the diagonal elements equal to a constant -0.5 in imaginary time. This ensures that without interactions, therefore with detached localised spins, we start with half-filling since $n^f = -G_{ii}^0(\tau = 0) = \frac{1}{2}$. The function is constant in imaginary time because without interactions, there is no excitation spectrum, which would be generated by slopes in the imaginary time Green function (compare section 5.5). This first guess is therefore also equivalent to the non-interacting lattice Green function for the f-electrons. The cluster solver gives the cluster Green function so that we can calculate the f-electron self-energy (also a local quantity) on the cluster. Since all the quantities are k-independent, calculation of the coarse-grained DCA lattice Green function just gives the cluster Green function again and convergence has already been reached in the first iteration step. In our application then, at each iteration step, we reset the f-electron sector of the Green function matrix to the known non-interacting lattice Green function for the f-electrons in order to keep statistical errors under control, which can creep in due to the QMC cluster solver.

2.4.3 Plotting the AF Green function in the extended BZ

As we have seen, in the AF phase the doubling of the unit cell due to the broken spin symmetry means that the true BZ is defined by a diamond shape, half the size of the original lattice BZ. In order to compare the single particle spectra $A(\mathbf{k}, \omega)$ of both cases we will later plot results for the AF spectra using the same k -vectors as in the PM case. That is to say, we are going to plot the AF spectra in an *extended* Brillouin zone scheme. This is justified because we calculate the combined excitation spectrum of spin-up and spin-down electrons. For this quantity the translational symmetry of the original lattice is restored so that the relevant k -space in which to plot is given by the original lattice BZ. The spectrum can be extracted from the lattice Green function which will be averaged over the two spin directions. However, in the AF broken symmetry formulation of the DCA, we have already shown that this Green function is a 2×2 matrix, reflecting the two orbitals of the unit cell. Transforming back to the k -vectors of the original BZ is achieved in the following. A real-space lattice site $\bar{\mathbf{x}}$ of the original lattice can be decomposed as

$$\bar{\mathbf{x}} = \tilde{\mathbf{x}} + \mathbf{X} + \mathbf{r}_\mu = \mathbf{x} + \mathbf{r}_\mu \quad (2.66)$$

so that an annihilation operator $c_{\bar{\mathbf{x}}}$ at this site may be written as $c_{\mathbf{x},\mathbf{r}_\mu}$. In momentum space an element of the original lattice BZ can be written as $\bar{\mathbf{k}} = \mathbf{k} + \mathbf{G}$ so that

$$c_{\bar{\mathbf{k}}} = \frac{1}{\sqrt{N}} \sum_{\mathbf{x},\mu} e^{-i\bar{\mathbf{k}}(\mathbf{x}+\mathbf{r}_\mu)} c_{\mathbf{x},\mathbf{r}_\mu} \quad (2.67)$$

$$= \frac{1}{\sqrt{N}} \sum_{\mathbf{x},\mu} e^{-i(\mathbf{k}+\mathbf{G})\mathbf{x}} e^{-i\bar{\mathbf{k}}\mathbf{r}_\mu} c_{\mathbf{x},\mathbf{r}_\mu} \quad (2.68)$$

$$= \frac{1}{\sqrt{N}} \sum_{\mathbf{x},\mu} e^{-i\mathbf{k}\mathbf{x}} e^{-i\bar{\mathbf{k}}\mathbf{r}_\mu} c_{\mathbf{x},\mathbf{r}_\mu}, \quad (2.69)$$

where in the last step we have used the fact that $\mathbf{G}\mathbf{x} = 2\pi m$ (m is a whole number) since they are reciprocal lattice vectors to each other per definition. Carrying out the sum over \mathbf{x} gives

$$c_{\bar{\mathbf{k}}} = \frac{1}{\sqrt{2}} \sum_{\mu} e^{-i\bar{\mathbf{k}}\mathbf{r}_\mu} c_{\mathbf{k},\mathbf{r}_\mu}. \quad (2.70)$$

Together with the equivalent formula for the creation operator, we can write the desired Green function in the extended Brillouin zone as

$$g_{\bar{\mathbf{k}}}(\mathbf{i}\omega_n) = \frac{1}{2} \sum_{\mu,\nu} e^{i\bar{\mathbf{k}}(\mathbf{r}_\nu - \mathbf{r}_\mu)} \left\{ \hat{G}_{\mathbf{k}}(\mathbf{i}\omega_n) \right\}_{\mu\nu} \quad (2.71)$$

$$= \frac{1}{2} \sum_{\mu,\nu} e^{i\bar{\mathbf{k}}(\mathbf{r}_\nu - \mathbf{r}_\mu)} \left\{ \frac{1}{\hat{G}_{\mathbf{k}}^0(\mathbf{i}\omega_n)^{-1} - \hat{\Sigma}^c(\mathbf{K}, \mathbf{i}\omega_n)} \right\}_{\mu\nu}. \quad (2.72)$$

We note that the Green function matrix on the right hand side of the equation is to be understood as the spin averaged matrix.

2.5 Technical Details in the Application of the Algorithm

2.5.1 Start point of the DCA iterative solution process

In general, we do not know in advance whether the parameters of a simulation will cause the system to order magnetically or not. We therefore begin each simulation by setting a small external magnetic field. This is achieved by adding a Zeeman term to the 2×2 free dispersion matrix $\hat{Z}_{\mathbf{k}}$ of the non-interacting Green function (compare derivation in section 2.4.2) that we use to start a simulation:

$$\hat{G}_{\mathbf{k},\sigma}^0(\mathbf{i}\omega_m) = \left[\mathbf{i}\omega_m \mathbb{1} - \hat{Z}_{\mathbf{k},\sigma} \right]^{-1}, \quad (2.73)$$

where, if we also include a nearest neighbour hopping,

$$\hat{Z}_{\mathbf{k},\sigma} = \begin{pmatrix} -2t'[\cos(\mathbf{k}\mathbf{a}_1) + \cos(\mathbf{k}\mathbf{a}_2)] & -tz \\ & -tz^* \\ & -2t'[\cos(\mathbf{k}\mathbf{a}_1) + \cos(\mathbf{k}\mathbf{a}_2)] \end{pmatrix} + \sigma \begin{pmatrix} h_z & 0 \\ 0 & h_z \end{pmatrix}. \quad (2.74)$$

The second term is for the external staggered magnetic field which is only included to start a simulation. If the parameters of the simulation are such as to stabilise the AF order, then this will become evident in the broken spin symmetry of the DCA self-energy.

2.5.2 Convergence of the solution

In practice we confirm that the DCA self-consistent equations have been fulfilled by initially checking the convergence of the observables in which we are interested. After convergence, we additionally check that the coarse-grained Green function $\bar{G}_{\mathbf{K}}(\tau)$ is equal to the QMC cluster Green function $G_{\mathbf{K}}^c(\tau)$ within the statistical error bars. Far from the magnetic phase transition the system often converges quickly (within some 15 iterations) to a self-consistent solution. Close to the phase transition convergence experiences critical slowing down. The magnetisation fluctuates around the final self-consistent solution value for many iterations. We show the typical progression of the staggered magnetisation with iterations for the two cases in Fig. 2.7. In the case of slow convergence, we have experimented with achieving better results by carrying out a series of simulations with identical parameters except for the value of an applied external field, implemented as in the previous subsection, but where we keep its value constant until convergence is reached. A small applied AF field reduces the number of iterations needed to reach convergence, and the hope was that if the field was small enough we could linearly extrapolate the QMC measured magnetisation down to the result we would obtain with zero applied field. However, experience has shown that the size of field required in order to justify linear extrapolation does not reduce the number of iterations required for convergence significantly. Since we must carry out a number of simulations, one for each value of the applied field, the total number of iterations required to obtain a solution via this proposed extrapolation method is not reduced.

2.5.3 Interpolation of the Self-Energy

When using a cluster of size $N_c^{AF} > 1$ the Brillouin zone is divided into N_c^{AF} patches. The DCA will give a self-energy function $\Sigma(\mathbf{K}_i, i\omega_n)$ for each of the centre of patch vectors \mathbf{K}_i . When plotting the single particle spectrum there will be a discontinuous jump in the spectrum when moving from one patch in k-space to the next since the self-energy will

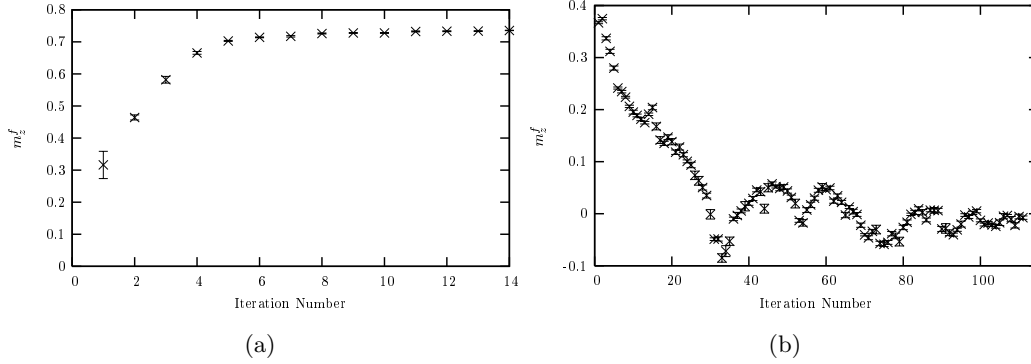


Figure 2.7: Typical progression of the staggered magnetisation (shown here for $J/t = 0.8$, $\beta t = 100$) with the number of DCA iterations: a) well inside the AF ordered phase where convergence is fast. b) slow convergence very close to the magnetic phase transition

be different in the next patch. As N_c^{AF} is increased, the discontinuities would decrease in size until a smooth function is reached in the $N_c^{AF} = N$ limit. If we desire, we might wish to interpolate the self-energy between the patches to obtain smooth spectral functions in k -space. Arguably, however, one should not do anything with the self-energy, since this is the result one obtains in the well-reasoned DCA, which is known to be a causal and conserving approximation. Nevertheless, perhaps only for aesthetic reasons, we describe a possible interpolation scheme for the self-energy in the following.

By means of example we take $N_c^{AF} = 4$ but a generalisation to larger cluster sizes is trivial. We write the self-energy for a given centre-of-patch vector \mathbf{K}_i as

$$\Sigma(\mathbf{K}_i, i\omega_n) = \sum_{\mathbf{r}} e^{i\mathbf{K}_i \cdot \mathbf{r}} A(\mathbf{r}, i\omega_n), \quad (2.75)$$

where the vectors \mathbf{r} are the vectors of the original square lattice and $A(\mathbf{r}, i\omega_n)$ is a suitable function. If we choose an origin vector and then divide the lattice vectors in the sum into *shells* around that origin, determined as nearest neighbour, next-nearest neighbour and so on, then we can rewrite as

$$\Sigma(\mathbf{K}_i, i\omega_n) = \sum_{\{\mathbf{r}_1\}} e^{i\mathbf{K}_i \cdot \mathbf{r}_1} A(\mathbf{r}_1, i\omega_n) + \sum_{\{\mathbf{r}_2\}} e^{i\mathbf{K}_i \cdot \mathbf{r}_2} A(\mathbf{r}_2, i\omega_n) + \dots \quad (2.76)$$

with the set of vectors $\{r_i\}$ in shell i given by

$$\begin{aligned} \{r_1\} &= \begin{pmatrix} 0 \\ 0 \end{pmatrix} \\ \{r_2\} &= \begin{pmatrix} 0 \\ 1 \end{pmatrix}, \begin{pmatrix} 1 \\ 0 \end{pmatrix}, \begin{pmatrix} 0 \\ -1 \end{pmatrix}, \begin{pmatrix} -1 \\ 0 \end{pmatrix} \\ \{r_2\} &= \{\dots\text{next-nearest neighbour vectors}\dots\} \\ &\vdots \end{aligned}$$

For a given Matsubara frequency we use a shorthand notation

$$S_{ij} = \sum_{\{\mathbf{r}_j\}} e^{i\mathbf{K}_i \mathbf{r}_j} \quad (2.77)$$

$$A_j = A(r_j, i\omega_n) \quad (2.78)$$

$$\Sigma_i = \Sigma(\mathbf{K}_i, i\omega_n) \quad (2.79)$$

and can then setup the equation system

$$\Sigma_i = S_{ij} A_j \quad (2.80)$$

with summation over j . Writing as vectors and inverting the equation we have

$$\vec{A} = \hat{S}^{-1} \vec{\Sigma} \quad (2.81)$$

such that we can find the required functions $A(r_i, i\omega_n)$. Now for a vector \mathbf{k} lying somewhere between cluster vectors (between centre-of-patch vectors) we can interpolate the self-energy as

$$\Sigma(\mathbf{k}, i\omega_n) = \sum_{i=1}^4 \sum_{\{\mathbf{r}_i\}} e^{i\mathbf{k}\mathbf{r}_i} A(r_i, i\omega_n). \quad (2.82)$$

Obviously, if \mathbf{k} is in fact a cluster vector \mathbf{K} then the above equation will just give the correct value of the self-energy as per definition in (2.76).² For a vector between the cluster vectors, the shell system interpolates the self-energy.

²This is an important point and we note, with particular relevance to our later discussion of the Fermi surface, that for $N_c^{AF} = 4$ there are cluster vectors at both (π, π) and $(\frac{\pi}{2}, \frac{\pi}{2})$ and as such the results there are definitely not influenced by any interpolation process.

3 QMC Hirsch-Fye Cluster Solver

3.1 Auxiliary Field Quantum Monte-Carlo Formulation of the KLM

The DCA method is dependent on an effective cluster solver to calculate the self-energy for an effective model with non-interacting Green function equal to the bath Green function \mathcal{G} . We employ a QMC auxiliary field method where the algorithm is essentially that of Hirsch and Fye [34] first introduced to treat a small number of magnetic impurities in a metal. The formulation requires that we are able to write the Hamiltonian in a form suitable for the introduction of auxiliary fields.

The KLM is given by

$$H_{KLM} = \sum_{\mathbf{k}, \sigma} \epsilon(\mathbf{k}) c_{\mathbf{k}\sigma}^\dagger c_{\mathbf{k}\sigma} + J \sum_{\mathbf{i}} \mathbf{S}_{\mathbf{i}}^c \cdot \mathbf{S}_{\mathbf{i}}^f. \quad (3.1)$$

We rewrite this in a quadratic form

$$H' = \sum_{\mathbf{k}, \sigma} \epsilon(\mathbf{k}) c_{\mathbf{k}\sigma}^\dagger c_{\mathbf{k}\sigma} - \frac{J}{4} \sum_{\mathbf{i}} \left(\sum_{\sigma} c_{\mathbf{i}\sigma}^\dagger f_{\mathbf{i}\sigma} + f_{\mathbf{i}\sigma}^\dagger c_{\mathbf{i}\sigma} \right)^2. \quad (3.2)$$

The relationship between H' and H is given by realising that when multiplying out the square in (3.2) this term only allows pair hopping between the c and f orbitals, for example $c_{\mathbf{i}\uparrow}^\dagger c_{\mathbf{i}\downarrow}^\dagger f_{\mathbf{i}\downarrow} f_{\mathbf{i}\uparrow}$. The term does not however produce any single electron hopping between these orbitals. Therefore the total number of doubly occupied and empty f-sites is conserved:

$$\left[H', \sum_{\mathbf{i}} (1 - n_{\mathbf{i}\uparrow}^f)(1 - n_{\mathbf{i}\downarrow}^f) + n_{\mathbf{i}\uparrow}^f n_{\mathbf{i}\downarrow}^f \right] = 0. \quad (3.3)$$

Applying a projection Q_0 onto the subspace with no doubly occupied or empty f-sites is then seen to give the KLM:

$$H' Q_0 = H_{KLM}. \quad (3.4)$$

In practical application this projection can be achieved by adding a Hubbard term H_U for f-sites. The resultant model Hamiltonian $H = H' + H_U$ is in a convenient form for

auxiliary field QMC:

$$\begin{aligned}
 H = & \sum_{\mathbf{k}, \sigma} \epsilon(\mathbf{k}) c_{\mathbf{k}\sigma}^\dagger c_{\mathbf{k}\sigma} - \frac{J}{4} \sum_{\mathbf{i}} \left(\sum_{\sigma} c_{\mathbf{i}\sigma}^\dagger f_{\mathbf{i}\sigma} + f_{\mathbf{i}\sigma}^\dagger c_{\mathbf{i}\sigma} \right)^2 \\
 & + U_f \sum_{\mathbf{i}} (n_{\mathbf{i}\uparrow}^f - \frac{1}{2})(n_{\mathbf{i}\downarrow}^f - \frac{1}{2}).
 \end{aligned} \tag{3.5}$$

We can write

$$H = H_t + H_J + H_U \tag{3.6}$$

with which we initially wish to calculate the partition function

$$Z = \text{Tr} \left[e^{-\beta(H - \mu N)} \right]. \tag{3.7}$$

The three terms in the Hamiltonian do not commute with each other but we may still factorise the exponential function by using the Trotter decomposition. The propagation in imaginary time from 0 to β is split into L_T time-slices of equal size $\Delta\tau$ such that $L_T \Delta\tau = \beta$. For non-commuting operators H_1, H_2 in the Hamiltonian $H = H_1 + H_2$ it is clear that $e^{-\beta(H_1 + H_2)} = \lim_{\Delta\tau \rightarrow 0} [e^{-\Delta\tau H_1} e^{-\Delta\tau H_2}]^{L_T}$. For a small, but finite $\Delta\tau$ it can be shown¹ that when calculating the expectation value of an operator O then

$$\frac{\text{Tr}[e^{-\beta H} O]}{\text{Tr}[e^{-\beta H}]} = \frac{\text{Tr}[(e^{-\Delta\tau H_1} e^{-\Delta\tau H_2})^{L_T} O]}{\text{Tr}[(e^{-\Delta\tau H_1} e^{-\Delta\tau H_2})^{L_T}]} + \mathcal{O}(\Delta\tau^2) \tag{3.8}$$

and the systematic error of the Trotter decomposition is of order $\Delta\tau^2$.

For our partition function we therefore write

$$Z = \text{Tr} \left[\prod_{\tau=1}^{L_T} e^{-\Delta\tau H_U} e^{-\Delta\tau H_J} e^{-\Delta\tau H_t} \right]. \tag{3.9}$$

The terms with H_J and H_U are two-particle terms which we cannot calculate trivially. To handle these terms we introduce auxiliary fields to reduce down to single particle operators however this can only be achieved at the expense of having to perform a large sum over all possible field configurations. This is where the QMC sampling comes in: A configuration occurs with a certain statistical weight and therefore measurements of Greens functions and observables are carried out by summing the individual measurements for each configuration reached in a Markov chain of configurations.

With a Hubbard-Stratonovich transformation we introduce the field variable $l = \pm 1, \pm 2$ for the H_J quadratic term [40] to obtain

$$e^{-\Delta\tau H_J} = \prod_{\mathbf{i}} e^{\Delta\tau \frac{J}{4} (\sum_{\sigma} c_{\mathbf{i}\sigma}^\dagger f_{\mathbf{i}\sigma} + f_{\mathbf{i}\sigma}^\dagger c_{\mathbf{i}\sigma})^2} \tag{3.10}$$

$$= \prod_{\mathbf{i}} \left(\sum_{l=\pm 1, \pm 2} \gamma(l) e^{\sqrt{\frac{\Delta\tau J}{4}} \eta(l) \sum_{\sigma} (c_{\mathbf{i}\sigma}^\dagger f_{\mathbf{i}\sigma} + f_{\mathbf{i}\sigma}^\dagger c_{\mathbf{i}\sigma})} + \mathcal{O}(\Delta\tau^4) \right), \tag{3.11}$$

¹the proof assumes that both H_1 and H_2 and also the operator O in question must be simultaneously real representable in a given basis. See, for example, reference [29], appendix B for further details

where

$$\gamma(\pm 1) = 1 + \frac{\sqrt{6}}{3}, \quad \gamma(\pm 2) = 1 - \frac{\sqrt{6}}{3} \quad (3.12)$$

$$\eta(\pm 1) = \pm \sqrt{2(3 - \sqrt{6})}, \quad \eta(\pm 2) = \pm \sqrt{2(3 + \sqrt{6})}. \quad (3.13)$$

The transformation is approximate with error proportional to $\Delta\tau^4$ on each time slice. The total systematic error gathered over all time slices will be proportional to $L_T\Delta\tau^4$ which is equal to $\beta\Delta\tau^3$ and therefore an order of magnitude smaller than the error incurred by the Trotter decomposition.

For the H_U -term we introduce the auxiliary field variables $s_{\mathbf{i}} = \pm 1$ to write

$$e^{-\Delta\tau H_U} = e^{-\Delta\tau U_f \sum_{\mathbf{i}} (n_{\mathbf{i}\uparrow}^f - \frac{1}{2})(n_{\mathbf{i}\downarrow}^f - \frac{1}{2})} \quad (3.14)$$

$$= C \sum_{s_1, \dots, s_N = \pm 1} e^{\alpha \sum_{\mathbf{i}} s_{\mathbf{i}} (n_{\mathbf{i}\uparrow}^f - n_{\mathbf{i}\downarrow}^f)} \quad (3.15)$$

with

$$C = \frac{e^{-\frac{\Delta\tau U N}{4}}}{2^N}, \quad \cosh(\alpha) = e^{\frac{\Delta\tau U}{2}}. \quad (3.16)$$

We insert (3.11) and (3.15) into the partition function (3.9) and after we pull the sum over the field variables to the front, which means both field variables now possess an imaginary time index and an index for each lattice site, we are left with

$$Z = \sum_{\substack{\{s_{\mathbf{i},\tau}\} = \pm 1 \\ \{l_{\mathbf{j},\tau}\} = \pm 1, \pm 2}} C^{L_T} \left(\prod_{\mathbf{i},\tau} \gamma(l_{\mathbf{i},\tau}) \right) \text{Tr} \left[\prod_{\tau=1}^{L_T} e^{\alpha \sum_{\mathbf{i}} s_{\mathbf{i},\tau} (n_{\mathbf{i}\uparrow}^f - n_{\mathbf{i}\downarrow}^f)} \times \right. \\ \left. \times e^{\sqrt{\frac{\Delta\tau J}{4}} \sum_{\mathbf{j}} \eta(l_{\mathbf{j},\tau}) \sum_{\sigma} (c_{\mathbf{j}\sigma}^{\dagger} f_{\mathbf{j}\sigma} + f_{\mathbf{j}\sigma}^{\dagger} c_{\mathbf{j}\sigma})} e^{-\Delta\tau \sum_{\mathbf{k},\sigma} (\epsilon(\mathbf{k}) - \mu) c_{\mathbf{k}\sigma}^{\dagger} c_{\mathbf{k}\sigma}} \right]. \quad (3.17)$$

We introduce the operator $a_{x,\sigma}$ where the index x is a super-index representing the lattice site and whether we are dealing with an f-electron orbital or c-electron orbital at that site. Therefore we set $x = (\mathbf{i}, n)$ and define $a_{(\mathbf{i},1),\sigma} = f_{\mathbf{i},\sigma}$ and $a_{(\mathbf{i},2),\sigma} = c_{\mathbf{i},\sigma}$. With these operators we construct vector-like objects \vec{a}_{σ} and $\vec{a}_{\sigma}^{\dagger}$ corresponding to column and row vectors, respectively, where each element $a_{x,\sigma}$ of the vector is actually a 2×2 matrix. Using this representation we can write the partition function as

$$Z = \sum_{\substack{\{s_{\mathbf{i},\tau}\} = \pm 1 \\ \{l_{\mathbf{j},\tau}\} = \pm 1, \pm 2}} C^{L_T} \left(\prod_{\mathbf{i},\tau} \gamma(l_{\mathbf{i},\tau}) \right) \prod_{\sigma} \text{Tr}^{(\sigma)} \left[e^{\vec{a}_{\sigma}^{\dagger} \hat{V}^{(\sigma)}(\{s_{\mathbf{i},\tau}\}) \vec{a}_{\sigma}} \times \right. \\ \left. \times e^{\vec{a}_{\sigma}^{\dagger} \hat{J}(\{l_{\mathbf{i},\tau}\}) \vec{a}_{\sigma}} e^{-\Delta\tau \vec{a}_{\sigma}^{\dagger} \hat{T} \vec{a}_{\sigma}} \right]. \quad (3.18)$$

We note that the trace can be broken into the product of the trace over the spin-up and spin-down sectors since the Hamiltonian is block diagonal in spin-space. The matrices \hat{J} and \hat{T} are spin independent but since the discrete Hubbard-Stratonovich transformation used to decouple the two-particle Coulomb interaction term breaks spin-symmetry for a given field configuration $\{s_{i,\tau}\}$, the matrix $\hat{V}^{(\sigma)}$ carries a spin index. Using the properties of Slater determinants to evaluate the trace the partition function can then be written as

$$Z = \sum_{\substack{\{s_{i,\tau}\}=\pm 1 \\ \{l_{j,\tau}\}=\pm 1,\pm 2}} C^{L_T} \left(\prod_{i,\tau} \gamma(l_{i,\tau}) \right) \prod_{\sigma} \det \left[\mathbb{1} + \hat{B}_{L_T}^{(\sigma)} \dots \hat{B}_1^{(\sigma)} \right], \quad (3.19)$$

with the $N \times N$ matrix (where the elements are themselves again 2×2 matrices)

$$\hat{B}_{\tau}^{(\sigma)} = e^{\hat{V}^{(\sigma)}(\{s_{i,\tau}\})} e^{\hat{J}(\{l_{i,\tau}\})} e^{-\Delta\tau\hat{T}}. \quad (3.20)$$

To continue we introduce the further definitions

$$U_{\{s,l\}}(\tau_2, \tau_1) = \prod_{\sigma} \prod_{n=n_1+1}^{n_2} e^{\bar{a}_{\sigma}^{\dagger} \hat{V}^{(\sigma)}(\{s_{i,n}\}) \bar{a}_{\sigma}} e^{\bar{a}_{\sigma}^{\dagger} \hat{J}(\{l_{i,n}\}) \bar{a}_{\sigma}} e^{-\Delta\tau \bar{a}_{\sigma}^{\dagger} \hat{T} \bar{a}_{\sigma}}, \quad (3.21)$$

$$\hat{B}_{\{s,l\}}^{(\sigma)}(\tau_2, \tau_1) = \prod_{n=n_1+1}^{n_2} \hat{B}_n^{(\sigma)}, \quad (3.22)$$

with the imaginary times $\tau_i = n_i \Delta\tau$ on a Trotter time-slice. Since we have already formulated the partition function through the introduction of auxiliary fields we are now able to write the expectation value of an observable A as

$$\langle A \rangle = \frac{\sum_{\{s,l\}} \left(\prod_{i,\tau} \gamma(l_{i,\tau}) \right) \text{Tr} [U_{\{s,l\}}(\beta, 0) A]}{\sum_{\{s,l\}} \left(\prod_{i,\tau} \gamma(l_{i,\tau}) \right) \prod_{\sigma} \det \left(\mathbb{1} + \hat{B}_{\{s,l\}}^{(\sigma)}(\beta, 0) \right)} \quad (3.23)$$

$$= \sum_{\{s,l\}} \frac{\left(\prod_{i,\tau} \gamma(l_{i,\tau}) \right) \prod_{\sigma} \det \left(\mathbb{1} + \hat{B}_{\{s,l\}}^{(\sigma)}(\beta, 0) \right)}{\sum_{\{s,l\}} \left(\prod_{i,\tau} \gamma(l_{i,\tau}) \right) \prod_{\sigma} \det \left(\mathbb{1} + \hat{B}_{\{s,l\}}^{(\sigma)}(\beta, 0) \right)} \times \frac{\text{Tr} [U_{\{s,l\}}(\beta, 0) A]}{\prod_{\sigma} \det \left(\mathbb{1} + \hat{B}_{\{s,l\}}^{(\sigma)}(\beta, 0) \right)} \quad (3.24)$$

$$= \sum_{\{s,l\}} \left(\frac{\left(\prod_{i,\tau} \gamma(l_{i,\tau}) \right) \prod_{\sigma} \det \left(\mathbb{1} + \hat{B}_{\{s,l\}}^{(\sigma)}(\beta, 0) \right)}{\sum_{\{s,l\}} \left(\prod_{i,\tau} \gamma(l_{i,\tau}) \right) \prod_{\sigma} \det \left(\mathbb{1} + \hat{B}_{\{s,l\}}^{(\sigma)}(\beta, 0) \right)} \right) \times \left(\frac{\text{Tr} [U_{\{s,l\}}(\beta, 0) A]}{\text{Tr} [U_{\{s,l\}}(\beta, 0)]} \right) \quad (3.25)$$

$$= \frac{\sum_{\{s,l\}} P_{\{s,l\}} \langle A \rangle_{\{s,l\}}}{\sum_{\{s,l\}} P_{\{s,l\}}}. \quad (3.26)$$

In the final line we have introduced the definitions

$$P_{\{s,l\}} = \left(\prod_{\mathbf{i},\tau} \gamma(l_{\mathbf{i},\tau}) \right) \prod_{\sigma} \det \left(\mathbb{1} + \hat{B}_{\{s,l\}}^{(\sigma)}(\beta, 0) \right) \quad (3.27)$$

and

$$\langle A \rangle_{\{s,l\}} = \frac{\text{Tr} [U_{\{s,l\}}(\beta, 0) A]}{\text{Tr} [U_{\{s,l\}}(\beta, 0)]}. \quad (3.28)$$

The observable can therefore be calculated by performing the weighted summation of $\langle A \rangle_{\{s,l\}}$ for each field configuration $\{s, l\}$. We therefore equate $\langle A \rangle_{\{s,l\}}$ with the value of the observable for that given field configuration. The function $W = \frac{P_{\{s,l\}}}{\sum_{\{s,l\}} P_{\{s,l\}}}$ could be interpreted as a probability since the summing over $\{s, l\}$ gives 1. However to interpret W as a probability it must also be positive which is not necessarily the case. We therefore write

$$P_{\{s,l\}} = \text{sign}_{\{s,l\}} |P_{\{s,l\}}|, \quad (3.29)$$

where $\text{sign}_{\{s,l\}}$ is just ± 1 dependent on the field configuration. We can then derive for the observable

$$\langle A \rangle = \frac{\sum_{\{s,l\}} \text{sign}_{\{s,l\}} |P_{\{s,l\}}| \langle A \rangle_{\{s,l\}}}{\sum_{\{s,l\}} \text{sign}_{\{s,l\}} |P_{\{s,l\}}|} \quad (3.30)$$

$$= \frac{\left(\sum_{\{s,l\}} |P_{\{s,l\}}| \text{sign}_{\{s,l\}} \langle A \rangle_{\{s,l\}} \right) / \left(\sum_{\{s,l\}} |P_{\{s,l\}}| \right)}{\left(\sum_{\{s,l\}} |P_{\{s,l\}}| \text{sign}_{\{s,l\}} \right) / \left(\sum_{\{s,l\}} |P_{\{s,l\}}| \right)}, \quad (3.31)$$

which we can write as

$$\langle A \rangle = \frac{\langle \text{sign} A \rangle'}{\langle \text{sign} \rangle'}, \quad (3.32)$$

where we mean that the average value of $\text{sign} A$ must be divided by the average sign , where both values are now calculated with the positive definite probability function $W' = \frac{|P_{\{s,l\}}|}{\sum_{\{s,l\}} |P_{\{s,l\}}|} = \frac{P'_{\{s,l\}}}{\sum_{\{s,l\}} P'_{\{s,l\}}}$. This allows a proper definition in terms of weight functions but has the drawback that if the average $\text{sign} \langle \text{sign} \rangle'$ is small then the QMC simulation requires much more time to run to compensate for the statistical fluctuations of the observable. One may think that the origin of this *sign problem* which is often the limitation of QMC methods might be just in the particular choice of Hubbard-Stratonovich transformation. While some decompositions may alleviate the sign problem to some degree it has been argued that Hubbard-Stratonovich transformations in general are unable to resolve the problem [41].

In the spirit of Monte-Carlo, instead of carrying out the huge sum over the configuration space of the auxiliary fields, a Markov chain of configurations is created where the configurations in the chain occur according to the weight function $P'_{\{s,l\}}$ which we will just call

$P_{\{s,l\}}$ from now on. The value of the observable measured at each of these configurations is averaged to obtain a final value with a statistical error proportional to the square root of the number of configurations in the chain. The process for choosing the next configuration in the chain must underly the conditions of ergodicity and detail balance. Our sampling procedure is to sweep through the complete set of field variables and propose a new value for each one sequentially. For this s-field variable this means a change proposal at position m of $s_m \rightarrow s'_m = -s_m$, and for the l-field a change to a new value $\pm 1, \pm 2$ is selected randomly. If we call the new configuration after one such move $\{s', l'\}$ then for the proposed move we define an acceptance ratio as

$$R = \frac{P'_{\{s,l\}}}{P_{\{s,l\}}} \quad (3.33)$$

and the move is accepted either via a Metropolis algorithm or, as we use here, heat-bath method. A proposed move is therefore accepted if a generated random number $x \in [0, 1]$ satisfies

$$x \leq \frac{R}{1 + R}. \quad (3.34)$$

3.2 The Hirsch-Fye QMC algorithm in application to the KLM

The further development of the auxiliary field formalism and derivation of the Hirsch-Fye algorithm essentially follows the usual route [34, 42], but with some particular features due to the fact that we have two sets of auxiliary field variables. We review here solely the fundamental definitions, the acceptance probability for a suggested change in the field-configuration for the next step in the Markov chain, and the subsequent update equation for the Green function matrix, which is the central equation of the algorithm. We first define the Green function matrix $g^{(\sigma)}$ with total dimension $2NL_T \times 2NL_T$, which we divide into $NL_T \times NL_T$ blocks of 2×2 matrices in which row/column 1 refers to the f-electron orbital and row/column 2 refers to the c-electron orbital. We use the super-index labelling $x = (\mathbf{i}, \tau)$ for rows or columns of this super-matrix. Therefore

$$g_{xy}^{(\sigma)} = \begin{pmatrix} \langle T f_{\mathbf{i}\sigma}(\tau_1) f_{\mathbf{j}\sigma}^\dagger(\tau_2) \rangle & \langle T f_{\mathbf{i}\sigma}(\tau_1) c_{\mathbf{j}\sigma}^\dagger(\tau_2) \rangle \\ \langle T c_{\mathbf{i}\sigma}(\tau_1) f_{\mathbf{j}\sigma}^\dagger(\tau_2) \rangle & \langle T c_{\mathbf{i}\sigma}(\tau_1) c_{\mathbf{j}\sigma}^\dagger(\tau_2) \rangle \end{pmatrix}. \quad (3.35)$$

Calculating g (dropping the spin for the moment) is handled in the same way as described for $\langle A \rangle$ in (3.26). Therefore we need to be able to calculate the elements of $g_{\{s,l\}}$ for each auxiliary field configuration in the Markov chain. The index $\{s, l\}$ is used to denote that the correlation functions of the Green function matrix are to be calculated in analogy to the definition of $\langle A \rangle_{\{s,l\}}$, i.e. for a given field configuration. We note that for a given arbitrary field configuration a Wick theorem applies for the Green function. Calculation

of the Green function matrix for each field configuration therefore gives complete access to all desired observables and correlation functions, because these can be decomposed into a sum of products of elements of the matrix $g_{\{s,l\}}$.

3.2.1 Update Equations

It can be shown [43] that

$$\det \left[\mathbb{1} + \hat{B}_{L_T}^{(\sigma)} \dots \hat{B}_1^{(\sigma)} \right] = \det \left[(g^{(\sigma)})^{-1} \right]. \quad (3.36)$$

With this useful relation we see from (3.33) and (3.27) that the update acceptance function R for a move can be written as

$$R = \frac{P'_{\{s,l\}}}{P_{\{s,l\}}} \quad (3.37)$$

$$= \left(\prod_{i,\tau} \frac{\gamma(l'_{i,\tau})}{\gamma(l_{i,\tau})} \right) \prod_{\sigma} \det \left[g^{(\sigma)} (g'^{(\sigma)})^{-1} \right]. \quad (3.38)$$

Now if the proposed move was for an s-field then the first bracketed term will be equal to one since in that case the l' field variable configuration is unchanged from the original l configuration. For an l-field proposed move at site m this term is just $\frac{\gamma(l'_m)}{\gamma(l_m)}$. We also note that since the proposed move only changes a single field variable at a single site then the product $g^{(\sigma)} (g'^{(\sigma)})^{-1}$ is a relatively simple matrix equivalent to the identity matrix on all rows except the row corresponding to the flipped field variable such that the determinant is readily calculated.

The Green function matrix $g^{(\sigma)'}$ for configuration $\{s', l'\}$ is related to the Green function matrix $g^{(\sigma)}$ for configuration $\{s, l\}$ via the equation

$$g^{(\sigma)'} = g^{(\sigma)} \left[\mathbb{1} + \Delta^{(\sigma)} (\mathbb{1} - g^{(\sigma)}) \right]^{-1} \quad (3.39)$$

with the matrix

$$\Delta^{(\sigma)} = e^{\hat{V}^{(\sigma)}(\{s'_{i,\tau}\})} e^{\hat{J}(\{l'_{i,\tau}\})} \left(e^{\hat{V}^{(\sigma)}(\{s_{i,\tau}\})} e^{\hat{J}(\{l_{i,\tau}\})} \right)^{-1} - \mathbb{1}. \quad (3.40)$$

A configuration change $\{s, l\} \rightarrow \{s', l'\}$ consisting of an s-field variable flip at super-index site m (which represents a certain lattice site and Trotter time slice), such that $s'_m = -s_m$, whilst leaving the l-field unchanged gives

$$\Delta^{(\sigma)} = e^{\hat{V}^{(\sigma)}(\{s'_{i,\tau}\})} e^{-\hat{V}^{(\sigma)}(\{s_{i,\tau}\})} - \mathbb{1} \quad (3.41)$$

such that the coupling J-term does not play a role and the explicit form of the update equation follows precisely the original Hirsch-Fye algorithm [34].

A simple change of the l-field variable at site with super-index m takes the form $l_m \rightarrow l'_m \in \{\pm 1, \pm 2\}$ where we will randomly choose the new value l'_m from the set. We will use a simplified formalism such that

$$\Delta^{(\sigma)} = e^{\hat{V}^{(\sigma)}} e^{\hat{J}'} e^{-\hat{J}} e^{-\hat{V}^{(\sigma)}} - \mathbb{1}, \quad (3.42)$$

where since the matrix \hat{J} is dependent on the l-fields the changed configuration is represented by the dash on this matrix. Referring to (3.11) it is clear that

$$\left(\hat{J}\right)_{xy} = \sqrt{\frac{\Delta\tau J}{4}} \eta(l_x) \begin{pmatrix} 0 & 1 \\ 1 & 0 \end{pmatrix} \delta_{xy} \quad (3.43)$$

with only off-diagonal terms in the 2×2 matrix representing the orbitals for a given lattice site and Trotter slice (remember, $x = (\mathbf{i}, \tau)$ is a super-index) since the J-term only couples a c-orbital to an f-orbital. However, the interaction is local in space and time, hence δ_{xy} . For insertion into the exponential function in (3.42) we diagonalise \hat{J} to obtain the diagonal matrix \hat{D} :

$$\left(\hat{U}^T \hat{J} \hat{U}\right)_{xy} = \hat{D}_{xy} = \sqrt{\frac{\Delta\tau J}{4}} \eta(l_x) \begin{pmatrix} 1 & 0 \\ 0 & -1 \end{pmatrix} \delta_{xy} \quad (3.44)$$

with

$$\hat{U}_{xy} = \frac{1}{\sqrt{2}} \begin{pmatrix} 1 & -1 \\ 1 & 1 \end{pmatrix} \delta_{xy}. \quad (3.45)$$

We can now write

$$\left(\Delta^{(\sigma)}\right)_{xy} = \left(e^{\hat{V}^{(\sigma)}} \hat{U} (e^{\hat{D}'} e^{-\hat{D}} - \mathbb{1}) \hat{U}^T e^{-\hat{V}^{(\sigma)}}\right)_{xy}. \quad (3.46)$$

Now since we have assumed that the l-field is only to be changed for super-index m then this reduces simply to

$$\left(\Delta^{(\sigma)}\right)_{xy} = \begin{pmatrix} \xi_{11} & \xi_{12} \\ \xi_{21} & \xi_{22} \end{pmatrix} \delta_{xy} \delta_{xm} \quad (3.47)$$

$$= \xi^{(\sigma)} \delta_{xy} \delta_{xm} \quad (3.48)$$

with the matrix elements calculated to

$$\xi_{11} = \cosh \left[\sqrt{\frac{\Delta\tau J}{4}} (\eta(l'_m) - \eta(l_m)) \right] - 1, \quad (3.49)$$

$$\xi_{12} = e^{\sigma\alpha sm} \sinh \left[\sqrt{\frac{\Delta\tau J}{4}} (\eta(l'_m) - \eta(l_m)) \right], \quad (3.50)$$

$$\xi_{21} = \sinh \left[\sqrt{\frac{\Delta\tau J}{4}} (\eta(l'_m) - \eta(l_m)) \right] e^{-\sigma\alpha sm}, \quad (3.51)$$

$$\xi_{22} = \cosh \left[\sqrt{\frac{\Delta\tau J}{4}} (\eta(l'_m) - \eta(l_m)) \right] - 1. \quad (3.52)$$

In the update equation (3.39) we have the term

$$\left[\Delta^{(\sigma)}(\mathbb{1} - g^{(\sigma)}) \right]_{xy} = \sum_z \Delta_{xz}^{(\sigma)}(\mathbb{1} - g^{(\sigma)})_{zy} \quad (3.53)$$

$$= \sum_z \xi^{(\sigma)} \delta_{xz} \delta_{xm} (\mathbb{1} - g^{(\sigma)})_{zy} \quad (3.54)$$

$$= (\xi^{(\sigma)} \delta_{xm})(\mathbb{1} - g^{(\sigma)})_{my}. \quad (3.55)$$

This can now be represented in an “outer-product” manner of the form

$$\Delta^{(\sigma)}(\mathbb{1} - g^{(\sigma)}) = \vec{u} \otimes \vec{v}, \quad (3.56)$$

where the elements of the “vectors” \vec{u} , \vec{v} are really 2×2 matrices:

$$u_x = \xi^{(\sigma)} \delta_{xm}, \quad v_y = (\mathbb{1} - g^{(\sigma)})_{my}. \quad (3.57)$$

The expression is handled more easily by writing in terms of standard vectors with scalar elements defined by

$$\mathbf{u}_1 = (0, \dots, 0, \xi_{11}, \xi_{21}, 0, \dots, 0)^T, \quad (3.58)$$

$$\mathbf{u}_2 = (0, \dots, 0, \xi_{11}, \xi_{21}, 0, \dots, 0)^T, \quad (3.59)$$

$$\begin{aligned} \mathbf{v}_1 = & (\delta_{m1} - g_{m1}^{ff\sigma}, \delta_{m1} - g_{m1}^{fc\sigma}, \dots, \delta_{mn} - g_{mn}^{ff\sigma}, \delta_{mn} - g_{mn}^{fc\sigma}, \dots \\ & \dots, \delta_{mN} - g_{mN}^{ff\sigma}, \delta_{mN} - g_{mN}^{fc\sigma})^T, \end{aligned} \quad (3.60)$$

$$\begin{aligned} \mathbf{v}_2 = & (\delta_{m1} - g_{m1}^{cf\sigma}, \delta_{m1} - g_{m1}^{cc\sigma}, \dots, \delta_{mn} - g_{mn}^{cf\sigma}, \delta_{mn} - g_{mn}^{cc\sigma}, \dots \\ & \dots, \delta_{mN} - g_{mN}^{cf\sigma}, \delta_{mN} - g_{mN}^{cc\sigma})^T, \end{aligned} \quad (3.61)$$

so that then

$$\Delta^{(\sigma)}(\mathbb{1} - g^{(\sigma)}) = \mathbf{u}_1 \otimes \mathbf{v}_1 + \mathbf{u}_2 \otimes \mathbf{v}_2 \quad (3.62)$$

and the update equation for the Green function matrix is

$$g^{(\sigma)'} = g^{(\sigma)} [\mathbb{1} + \mathbf{u}_1 \otimes \mathbf{v}_1 + \mathbf{u}_2 \otimes \mathbf{v}_2]^{-1}. \quad (3.63)$$

To avoid a computationally costly large matrix inversion the Sherman-Morrison formula [44]

$$(A + \mathbf{u} \otimes \mathbf{v})^{-1} = A^{-1} - \frac{(A^{-1}\mathbf{u}) \otimes (\mathbf{v}A^{-1})}{1 + \mathbf{v} \cdot A^{-1}\mathbf{u}} \quad (3.64)$$

can be applied sequentially to finally obtain an effective update equation for single move updates $l_m \rightarrow l'_m$ of the J-term auxiliary field variables. From (3.64) (where for our purpose $A = \mathbb{1}$) we see that the core of the Green function update after a single field flip is an outer product: the size of the vectors means that $(2NL_T)^2$ multiplications will be required for the calculation. A complete sweep through all NL_T s-field and l-field variables is used to produce a new field configuration. Therefore, the computational time required for the update algorithm will scale with $(NL_T)^3$. Recently, however, we have been able to improve our update algorithm through implementation of so-called delayed updates (see appendix B).

4 Mean-Field and Spin Density Wave

4.1 The Large- \mathcal{N} Approach

As an aid to interpretation our results, and to get a feel for the KLM, we first look at what can be expected on the grounds of a mean-field theory or the large- \mathcal{N} approach. In a general sense \mathcal{N} represents an $SU(\mathcal{N})$ symmetry at each lattice site. Often, the method is applied to spin Hamiltonians with only $SU(2)$ symmetry, but even though 2 is not a large number, the large- \mathcal{N} approach can still be remarkably successful, but there is no way of knowing this in advance. In correlated electron physics the approach was first developed for heavy fermion models [45] where it proves to be a useful tool. Expansion around the large- \mathcal{N} limit in a $1/\mathcal{N}$ expansion was used to calculate Fermi liquid parameters [46, 47]. We begin by considering the Hamiltonian

$$H = \sum_{\mathbf{k}, \sigma} \epsilon(\mathbf{k}) c_{\mathbf{k}\sigma}^\dagger c_{\mathbf{k}\sigma} - \frac{J}{4} \sum_{\mathbf{i}} \left(\sum_{\sigma} c_{\mathbf{i}\sigma}^\dagger f_{\mathbf{i}\sigma} + f_{\mathbf{i}\sigma}^\dagger c_{\mathbf{i}\sigma} \right)^2 - \lambda \sum_{\mathbf{i}} (n_{\mathbf{i}}^f - 1), \quad (4.1)$$

which is the same quadratic form as the Hamilton (3.5) used as a form suitable for the introduction of auxiliary fields, but where now the condition of single occupancy on the f-sites is handled by introducing a Lagrange multiplier term $\lambda \sum_{\mathbf{i}} (n_{\mathbf{i}}^f - 1)$. Since we do not write a site index \mathbf{i} on λ the term represents a relaxation of strict single occupancy such that now the number of impurity spins per site is only equal to one on average.

We define the order parameter

$$V = \langle \hat{V} \rangle = \left\langle \sum_{\sigma} (c_{\mathbf{i}\sigma}^\dagger f_{\mathbf{i}\sigma} + f_{\mathbf{i}\sigma}^\dagger c_{\mathbf{i}\sigma}) \right\rangle \quad (4.2)$$

and write the interaction using the Hartree-Fock (HF) approximation, neglecting the quadratic fluctuation term $(\hat{V} - V)^2$ of the operator about its expectation value:

$$\frac{J}{4} \sum_{\mathbf{i}} \left(\sum_{\sigma} c_{\mathbf{i}\sigma}^\dagger f_{\mathbf{i}\sigma} + f_{\mathbf{i}\sigma}^\dagger c_{\mathbf{i}\sigma} \right)^2 = \frac{J}{4} \sum_{\mathbf{i}} \left(V + (\hat{V} - V) \right)^2 \quad (4.3)$$

$$\stackrel{\text{HF}}{\approx} \frac{J}{4} \sum_{\mathbf{i}} \left(V^2 + 2V(\hat{V} - V) \right). \quad (4.4)$$

In the non-approximated KLM the value of V would be zero due to the strict constraint of one localised impurity spin per site giving $\langle f_{\mathbf{i}\sigma}^\dagger c_{\mathbf{i}\sigma} \rangle = 0$, but in this mean-field approximation the single occupancy is given only on average so that V may be non-zero. It is

therefore used as a measure of the correlation between the c-sites and f-sites which we can equate to Kondo screening. We also refer to this Hamiltonian as the large- \mathcal{N} approach to the KLM since if one generalises the two spin *flavours*, spin-up and spin-down, to \mathcal{N} flavours, then in the limit of $\mathcal{N} \rightarrow \infty$ the approximated Hamiltonian becomes exact.

After Fourier transformation to momentum space the Hamiltonian reads

$$H = \sum_{\mathbf{k}\sigma} \begin{pmatrix} c_{\mathbf{k}\sigma}^\dagger & f_{\mathbf{k}\sigma}^\dagger \end{pmatrix} \begin{pmatrix} \epsilon_{\mathbf{k}} & -\Delta \\ -\Delta & \lambda \end{pmatrix} \begin{pmatrix} c_{\mathbf{k}\sigma} \\ f_{\mathbf{k}\sigma} \end{pmatrix} + N \left(\frac{JV^2}{4} - \lambda \right), \quad (4.5)$$

whereby $\Delta = \frac{JV}{2}$ and N is the number of sites in the lattice. The mean-field solution finds values for V and λ such that they fulfil the saddle point equations for the free energy $-\frac{1}{\beta} \ln Z[V, \lambda]$ (where $Z[V, \lambda]$ is the partition function):

$$\frac{\partial \ln Z[V, \lambda]}{\partial V} = \frac{\partial \ln Z[V, \lambda]}{\partial \lambda} = 0. \quad (4.6)$$

The Hamiltonian matrix in (4.5) can be diagonalised via unitary transformation matrix

$$U = \begin{pmatrix} u_{\mathbf{k}+} & -u_{\mathbf{k}-} \\ u_{\mathbf{k}-} & u_{\mathbf{k}+} \end{pmatrix} \quad (4.7)$$

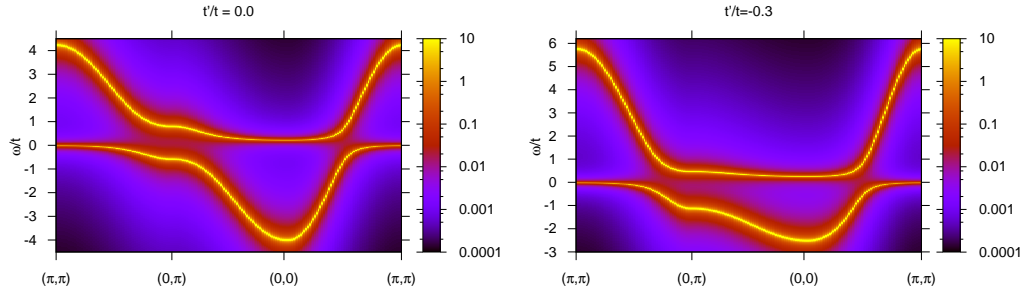
to obtain the mean-field solution. A non-zero hybridisation V causes the original light conduction electron band to be replaced by an upper and lower quasi-particle band with dispersion relations (see Fig. 4.1 for examples)

$$E_{\mathbf{k}\pm} = \frac{1}{2} \left[\epsilon(\mathbf{k}) + \lambda \pm \sqrt{(\epsilon(\mathbf{k}) - \lambda)^2 + 4\Delta^2} \right] \quad (4.8)$$

and quasi-particle weights given by

$$u_{\mathbf{k}\pm}^2 = \frac{1}{2} \left(1 \pm \frac{\epsilon(\mathbf{k}) - \lambda}{\sqrt{(\epsilon(\mathbf{k}) - \lambda)^2 + 4\Delta^2}} \right). \quad (4.9)$$

The band separation here is caused by the hybridisation of the conduction electron states with the local spin states to form heavy fermion states. At half-filling, the Fermi energy lies in this hybridisation gap giving rise to the Kondo insulator. In a hole doped system (for not too large doping) the Fermi energy cuts the dispersion in the vicinity of (π, π) where the large effective mass characterised by the very flat band in this region leads to the classification of a heavy hole-like Fermi surface. The term *large* Fermi surface is also used in this case to indicate the inclusion of the heavy fermion states in the Luttinger sum rule [48] for counting the number of particles in the Fermi surface volume.

(a) without next-nearest neighbour hopping (b) next nearest neighbour hopping $t'/t = -0.3$ **Figure 4.1:** Single particle spectrum obtained in the large- \mathcal{N} mean-field approximation at half-filling and with $J/t = 1$.

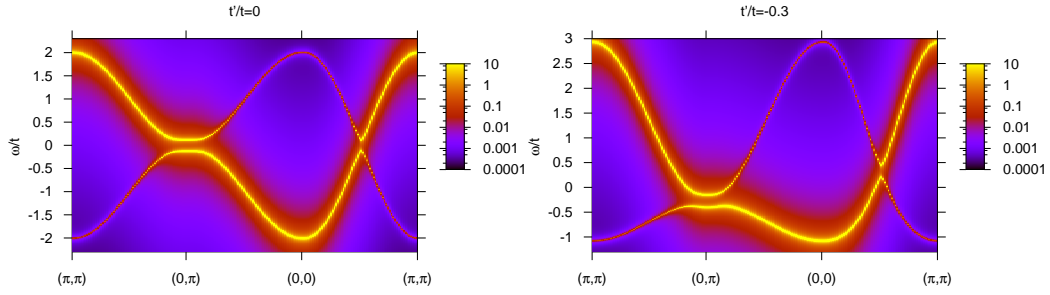
4.2 The Spin Density Wave Approach

Although the above approach was able to produce the flat band structure characteristic of experimental heavy fermion systems it takes no account of the RKKY interaction which is in competition with Kondo screening and which attempts to build an AF ordered state. Therefore, as an alternative, we may consider the spin density wave (SDW) picture (for example [49]) of the KLM. As motivation for such an approach, we draw on results from the one-dimensional Kondo lattice. In the 1D KLM the spin gap Δ_s tracks the Kondo temperature T_K of the single impurity problem as

$$\Delta_s \approx T_K^{\frac{1}{\nu}} \quad (1 \leq \nu \leq \frac{5}{4}). \quad (4.10)$$

Since the single impurity Kondo temperature is given by $T_K \propto \exp\left[-\frac{1}{D(\epsilon_F)J}\right]$ (where $D(\epsilon_F)$ is the conduction electron density of states at the Fermi energy), the spin gap becomes exponentially small for small couplings J/t . This means that the time scale for magnetic fluctuations becomes exponentially large, particularly in comparison to the time scale, set by $1/t$, for hopping of the conduction electrons. In this case, the conduction electrons can be considered as moving in a static magnetic background. Whether this picture is feasible in 2D for small J/t is debatable, because here we know that the spin gap is finite. Nevertheless, the SDW approach in 2D will give us more insight into the model and may be useful as a tool for interpreting the DCA/QMC results.

With the above in mind we go back to the Hamiltonian of the KLM and ask ourselves what the result would be if the f-spins were to display a fixed AF-ordering. This leads us


 (a) without next-nearest neighbour hopping (b) next nearest neighbour hopping $t'/t = -0.3$
Figure 4.2: Single particle spectrum obtained in the SDW approach at half-filling and with $J/t = 1$.

to replace

$$\mathbf{S}_i^f = \frac{1}{2} \begin{pmatrix} 0 \\ 0 \\ m \end{pmatrix} e^{i\mathbf{Q}i} \quad (4.11)$$

in the KLM Hamiltonian (1.1) to obtain

$$H = \sum_{\mathbf{k}\sigma} \begin{pmatrix} c_{\mathbf{k}\sigma}^\dagger & c_{\mathbf{k}+\mathbf{Q}\sigma}^\dagger \end{pmatrix} \begin{pmatrix} \epsilon_{\mathbf{k}} & \frac{Jm\sigma}{4} \\ \frac{Jm\sigma}{4} & \epsilon_{\mathbf{k}+\mathbf{Q}} \end{pmatrix} \begin{pmatrix} c_{\mathbf{k}\sigma} \\ c_{\mathbf{k}+\mathbf{Q}\sigma} \end{pmatrix}. \quad (4.12)$$

Again we obtain a two-band dispersion relation but now with

$$E_{\mathbf{k}\pm} = \frac{1}{2} \left[\epsilon(\mathbf{k}) + \epsilon(\mathbf{k} + \mathbf{Q}) \pm \left((\epsilon(\mathbf{k}) - \epsilon(\mathbf{k} + \mathbf{Q}))^2 + \left(\frac{Jm}{4} \right)^2 \right)^{\frac{1}{2}} \right] \quad (4.13)$$

and quasi-particle weights given by

$$u_{\mathbf{k}\pm}^2 = \frac{1}{2} \left(1 \pm \frac{\epsilon(\mathbf{k}) - \epsilon(\mathbf{k} + \mathbf{Q})}{\left((\epsilon(\mathbf{k}) - \epsilon(\mathbf{k} + \mathbf{Q}))^2 + \left(\frac{Jm}{4} \right)^2 \right)^{\frac{1}{2}}} \right). \quad (4.14)$$

The single particle spectrum obtained via this approach is shown in Fig. 4.2 on the example of $J/t = 1$ for both $t'/t = 0$ and $t'/t = -0.3$. For $t'/t = 0$ there is a direct band gap of size $Jm/4$. For $t'/t = -0.3$ however the SDW approach does not produce a band gap (Fig. 4.2).

Clearly this approach does not produce heavy fermion bands and the gap in the spectrum (in the absence of next-nearest neighbour hopping) has a different origin to the gap seen in

the previous mean-field approach. A static AF ordering on the f-sites means that we must define a new unit cell with two c-sites and two f-sites and the Brillouin zone of the lattice is the diamond shaped magnetic BZ; half-the size of the original lattice Brillouin zone. If we think in terms of quasi-free conduction electrons then the free dispersion relation of these electrons must firstly be folded back into this reduced MBZ creating two bands, reflecting the two conduction electrons of the unit cell, which for the moment are degenerate at the MBZ boundaries. Now since these quasi-free electrons are effectively moving in the spin-dependent potential of an AF background then Bragg reflection at the MBZ boundary lifts the energy level degeneracy by the creation of a gap with size proportional to the Fourier transform of the potential at a reciprocal lattice vector.

In the previous mean-field approach the gap opens due to the hybridisation between c-electrons and f-electrons: the size of the gap reflects the energy advantage gained through the formation of a composite quasi-particle, i.e. the localised magnetic moment together with its c-electron screening cloud. Since the degree of hybridisation should follow the Kondo scale then in that first case we would expect the gap to vanish exponentially with decreasing J/t . The origin of the gap seen in our numerical DCA results is examined in section 5.5.

4.3 A Mixed Approach

The third approach to the KLM, that we will draw on to gain understanding of the model and aid the interpretation of our numerical DCA results, is the mean-field approximation of Zhang and Yu [50]. This is basically a combination of the two previous approaches which employs the order parameters

$$\langle f_{\mathbf{i},\uparrow}^\dagger f_{\mathbf{i},\uparrow} - f_{\mathbf{i},\downarrow}^\dagger f_{\mathbf{i},\downarrow} \rangle = m_f e^{i\mathbf{Q}\mathbf{i}}, \quad (4.15)$$

$$\langle c_{\mathbf{i},\uparrow}^\dagger c_{\mathbf{i},\uparrow} - c_{\mathbf{i},\downarrow}^\dagger c_{\mathbf{i},\downarrow} \rangle = -m_c e^{i\mathbf{Q}\mathbf{i}}, \quad (4.16)$$

$$\langle f_{\mathbf{i},\uparrow}^\dagger c_{\mathbf{i},\uparrow} + c_{\mathbf{i},\downarrow}^\dagger f_{\mathbf{i},\downarrow} \rangle = \langle f_{\mathbf{i},\downarrow}^\dagger c_{\mathbf{i},\downarrow} + c_{\mathbf{i},\uparrow}^\dagger f_{\mathbf{i},\uparrow} \rangle = -V. \quad (4.17)$$

m_f and m_c are the staggered magnetisations of the impurity spins and conduction electrons respectively and V is a hybridisation order parameter measuring the screening of the impurity spins.

Again, we use a Lagrange multiplier term $\lambda \left(\left(\sum_{\mathbf{i},\sigma} f_{\mathbf{i}\sigma}^\dagger f_{\mathbf{i}\sigma} \right) - N \right)$ in the Hamiltonian to maintain an average of single occupancy on the f-sites. In the case of half-filling this term

is not necessary since there $\lambda = 0$. The Hamiltonian is now given by

$$\begin{aligned} \tilde{H} = & \sum_{\mathbf{k}\sigma} \begin{pmatrix} c_{\mathbf{k}\sigma} \\ c_{\mathbf{k}+\mathbf{Q}\sigma} \\ f_{\mathbf{k}\sigma} \\ f_{\mathbf{k}+\mathbf{Q}\sigma} \end{pmatrix}^\dagger \begin{pmatrix} \epsilon_{\mathbf{k}} - \mu & \frac{Jm_f\sigma}{4} & \frac{JV}{2} & 0 \\ \frac{Jm_f\sigma}{4} & \epsilon_{\mathbf{k}+\mathbf{Q}} - \mu & 0 & \frac{JV}{2} \\ \frac{JV}{2} & 0 & \lambda & -\frac{Jm_c\sigma}{4} \\ 0 & \frac{JV}{2} & -\frac{Jm_c\sigma}{4} & \lambda \end{pmatrix} \times \\ & \times \begin{pmatrix} c_{\mathbf{k}\sigma} \\ c_{\mathbf{k}+\mathbf{Q}\sigma} \\ f_{\mathbf{k}\sigma} \\ f_{\mathbf{k}+\mathbf{Q}\sigma} \end{pmatrix} + NJ \left(\frac{m_c m_f}{4} + \frac{V^2}{2} \right). \end{aligned} \quad (4.18)$$

A four-band energy dispersion relation is obtained where the magnetic character and Kondo screening character of the bands are tuned by the order parameters. In the limiting case $m_f = 0$, $m_c = 0$ but $V \neq 0$, with the magnetism shut out, we would recover the large- \mathcal{N} mean-field approximation. Equivalently, setting $V = 0$ but $m_f \neq 0$, $m_c \neq 0$ recovers the SDW result.

Motivation for this four-band modelling tool is given by exact BSS results for the finite sized, half-filled KLM [33], which have shown that Kondo screening is also present in the AF state, at least at half-filling. The spins are interpreted there as being partially screened with the remnant magnetic moments ordering antiferromagnetically and the coexistence of RKKY AF order and Kondo screening was seen to extend to small values of the coupling J/t . However, it was also demonstrated in that work that the solutions to the saddle point equations

$$\left\langle \frac{\partial \tilde{H}}{\partial m_f} \right\rangle = \left\langle \frac{\partial \tilde{H}}{\partial m_c} \right\rangle = \left\langle \frac{\partial \tilde{H}}{\partial V} \right\rangle = 0 \quad (4.19)$$

for the Zhang-Yu mean-field approximation in fact fail to describe the coexistence state of AF order and Kondo screening, which in this framework would be given by $m_f \neq 0$, $m_c \neq 0$ and also $V \neq 0$, except for a narrow crossover region around the AF order-disorder quantum critical point. We come back to this approximation in the discussion of the results of section 6.3.

5 The Half-Filled KLM

5.1 Perfect Nesting of the Fermi Surface

In this study, we have considered the KLM at half-filling in two cases: either with or without particle hole symmetry. Particle-hole symmetry is given if hopping is restricted to nearest neighbours on the square lattice. In this case the free band dispersion is given by $\epsilon(\mathbf{k}) = -2t [\cos(k_x) + \cos(k_y)]$ and the Fermi surface is a diamond (see Fig. 5.1).

A Fermi surface of this shape is said to exhibit *perfect nesting*, where a macroscopic number of electrons at the Fermi surface can be brought to another point on the Fermi surface, therefore without any energy transfer, by the same momentum transfer vector. In our case a momentum transfer of $\pm(\pi, \pi)$ or $\pm(-\pi, \pi)$ transfers electrons between the lower left and top right sides or the lower right and upper left sides of the Fermi surface diamond. To consider the consequences of this geometry, in particular with regard to the tendency towards magnetic ordering, we draw on the thoughts of appendix A on linear response functions and use a Kubo formula to obtain the magnetic susceptibility.

Assume we have an externally applied time-dependent and spatially oscillating magnetic field

$$\mathbf{H} = \mathbf{h}e^{i(\mathbf{q}\cdot\mathbf{r}_i - \omega t)} \quad (5.1)$$

which couples to the magnetic moment \mathbf{m}_i of the conduction electron at site i . Here, \mathbf{q} is the wave vector of the harmonic spacial oscillation of the field, ω the temporal oscillation frequency and \mathbf{r}_i the position vector of site i . The Hamiltonian will therefore include the perturbation term

$$V = - \sum_i \mathbf{m}_i \cdot \mathbf{h}e^{i(\mathbf{q}\cdot\mathbf{r}_i - \omega t)}. \quad (5.2)$$

We will further assume that the magnetic moment of the conduction electrons at each lattice site is given simply by

$$\mathbf{m}_i = g\mu_B \mathbf{S}_i \quad (5.3)$$

with Bohr magneton $\mu_B = \frac{e\hbar}{2mc}$ and gyromagnetic ratio $g \approx 2$. In this basic assumption we are neglecting any contributions, for example, due to spin-orbit coupling. The applied

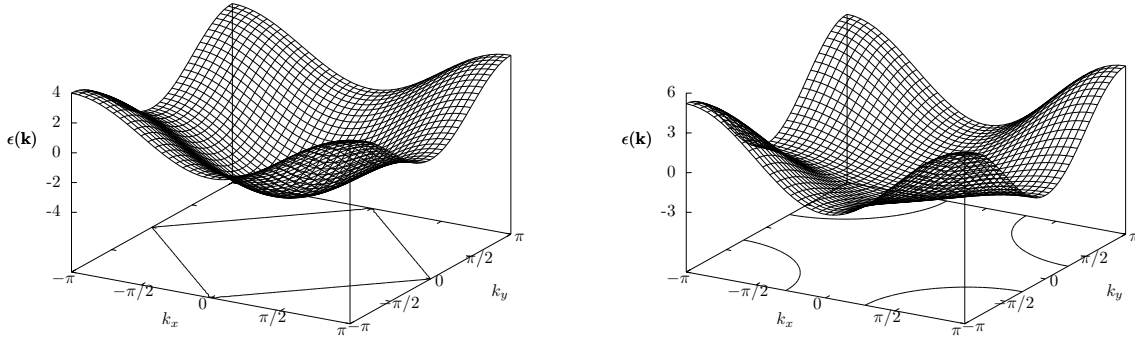


Figure 5.1: The conduction electron dispersion relation and Fermi surface at half-filling for two cases: (left) The particle-hole symmetrical case, i.e. without next-nearest neighbour hopping ($t' = 0$) (right) particle-hole unsymmetrical case with next-nearest neighbour hopping $t' = -0.3$.

field will affect the orientation of these magnetic moments, so the quantity we wish to consider is the so-called staggered magnetisation:

$$\mathbf{M}(\mathbf{q}) = \frac{1}{N} \sum_i \langle \mathbf{m}_i \rangle e^{-i\mathbf{q}\cdot\mathbf{r}_i}. \quad (5.4)$$

This exponential factor takes account of the fact that the applied field oscillates periodically in space and would therefore magnetise the spins accordingly. The staggered magnetisation is just a sum over expectation values which we can write using the Kubo formula (A.13), and inserting (5.2) for the perturbation term. We show this for one component $\alpha = x, y, z$ of \mathbf{M} :

$$M_t^\alpha(\mathbf{q}) = \frac{1}{N} \sum_i \langle m_i^\alpha \rangle_t e^{-i\mathbf{q}\cdot\mathbf{r}_i} \quad (5.5)$$

$$= \frac{1}{N} \sum_{\beta=x,y,z} \sum_{i,j} i \int_{-\infty}^t dt' h^\beta e^{i(\mathbf{q}\cdot\mathbf{r}_j - \omega t')} e^{-i\mathbf{q}\cdot\mathbf{r}_i} \langle [m_i^\alpha(t), m_j^\beta(t')]_- \rangle_0 \quad (5.6)$$

$$= \sum_{\beta=x,y,z} i \int_{-\infty}^t dt' e^{i\omega(t-t')} \langle [m^\alpha(\mathbf{q}, t), m^\beta(-\mathbf{q}, t')]_- \rangle_0 h^\beta e^{-i\omega t} \quad (5.7)$$

$$= \chi^{\alpha\beta}(\mathbf{q}, \omega) h^\beta e^{-i\omega t}. \quad (5.8)$$

In the above equation we have introduced the magnetic spin susceptibility function $\chi^{\alpha\beta}(\mathbf{q}, \omega) = i \int_{-\infty}^t dt' e^{i\omega(t-t')} \langle [m^\alpha(\mathbf{q}, t), m^\beta(-\mathbf{q}, t')]_- \rangle_0$, which is seen to be only a time Fourier transform of a retarded correlation function or, in other words, of a retarded Green function. At this stage we therefore rewrite the susceptibility in Matsubara formalism by defining

$$\chi^{\alpha\beta}(\mathbf{q}, i\nu) = \int_0^\beta d\tau e^{i\nu\tau} \langle T_\tau m^\alpha(\mathbf{q}, \tau) m^\beta(-\mathbf{q}, 0) \rangle_0 \quad (5.9)$$

so that analytic continuation

$$\chi^{\alpha\beta}(\mathbf{q}, i\nu) \xrightarrow{i\nu \rightarrow \omega + i\delta} \chi^{\alpha\beta}(\mathbf{q}, \omega) \quad (5.10)$$

returns the retarded correlation function for the susceptibility with real frequencies. We note that ν must be a bosonic Matsubara frequency ($\nu = \frac{2\pi n}{\beta}$) since the Green function defined in (5.9) is a correlation function of bosonic magnetic moment operators \mathbf{m} . Here, we wish only to consider the component χ^{zz} and we deal with the magnetic moment operators as described below. We first go back to real space:

$$m^z(\mathbf{q}, \tau) = \frac{1}{N} \sum_i e^{-i\mathbf{q}\cdot\mathbf{r}_i} m_i^z(\tau). \quad (5.11)$$

Now, since the z -component of the magnetic moment operator at site i is just given by $m_i^z = g\mu_B S_i^z$ (with $g \approx 2$) and the total z -component of spin at that site is given by $S_i^z = \frac{1}{2}(n_{i\uparrow} - n_{i\downarrow})$ then (5.11) becomes

$$m^z(\mathbf{q}, \tau) = \frac{\mu_B}{N} \sum_i e^{-i\mathbf{q}\cdot\mathbf{r}_i} \sum_{\sigma} \sigma c_{i\sigma}^{\dagger} c_{i\sigma} \quad (5.12)$$

$$= \frac{\mu_B}{N^2} \sum_{\sigma} \sum_{k, k'} \sigma c_{k\sigma}^{\dagger} c_{k'\sigma} \sum_i e^{-i(\mathbf{k}+\mathbf{q}-\mathbf{k}')\cdot\mathbf{r}_i}. \quad (5.13)$$

The sum over i produces the factor $N\delta_{\mathbf{k}+\mathbf{q}, \mathbf{k}'}$ so that then summing over k' results in

$$m^z(\mathbf{q}, \tau) = \frac{\mu_B}{N} \sum_{k, \sigma} \sigma c_{k\sigma}^{\dagger} c_{k+q\sigma} \quad (5.14)$$

We insert the moment operators into the correlation function (5.9) to obtain

$$\chi^{zz}(\mathbf{q}, i\nu) = \frac{\mu_B^2}{N^2} \sum_{kk', \sigma\sigma'} \sigma\sigma' \int_0^{\beta} d\tau e^{i\nu\tau} \langle T_{\tau} c_{k\sigma}^{\dagger}(\tau) c_{k+q\sigma}(\tau) c_{k'\sigma'}^{\dagger}(0) c_{k'-q\sigma'}(0) \rangle_0 \quad (5.15)$$

In order to calculate the expectation value here, we remember that the index “0” indicates that we are using the unperturbed density operator ρ_0 to build the trace, dependent only on H_0 , the Hamiltonian for the system of non-interacting electrons. Therefore, Wick decomposition is applicable and we may equate

$$\begin{aligned} \langle T_{\tau} c_{k\sigma}^{\dagger}(\tau) c_{k+q\sigma}(\tau) c_{k'\sigma'}^{\dagger}(0) c_{k'-q\sigma'}(0) \rangle_0 &= -\langle T_{\tau} c_{k\sigma}(0) c_{k\sigma}^{\dagger}(\tau) \rangle_0 \langle T_{\tau} c_{k+q\sigma}(\tau) c_{k+q\sigma}^{\dagger}(0) \rangle_0 \delta_{k', k+q} \delta_{\sigma, \sigma'} \\ &= -G_{k\sigma}^0(-\tau) G_{k+q\sigma}^0(\tau) \delta_{k', k+q} \delta_{\sigma, \sigma'}, \end{aligned} \quad (5.16)$$

$$= -G_{k\sigma}^0(-\tau) G_{k+q\sigma}^0(\tau) \delta_{k', k+q} \delta_{\sigma, \sigma'}, \quad (5.17)$$

where the $\delta_{\sigma, \sigma'}$ arises since for free electrons we have no terms in H_0 that allow spin flips and so we may only build contractions of operators with the same spin indices. The other Kronecker delta is a result of momentum conservation. We sum over σ' and k' and also Fourier transform the single particle Green functions of imaginary time to

fermionic Matsubara frequency functions according to $G(\tau) = \frac{1}{\beta} \sum_{n=-\infty}^{\infty} e^{-i\omega_n \tau} G(i\omega_n)$ with $\omega_n = (2n+1)\frac{\pi}{\beta}$ to obtain¹

$$\chi^{zz}(\mathbf{q}, i\nu) = -\frac{\mu_B^2}{N\beta} \sum_{k,\sigma} \sum_{m,n} \int_0^\beta d\tau e^{i\tau(\nu - \omega_m + \omega_n)} G_{k\sigma}^0(i\omega_n) G_{k+q\sigma}^0(i\omega_m) \quad (5.18)$$

$$= -\frac{\mu_B^2}{N\beta} \sum_{k,\sigma} \sum_n G_{k\sigma}^0(i\omega_n) G_{k+q\sigma}^0(i\omega_n + i\nu) \quad (5.19)$$

$$= -\frac{\mu_B^2}{N\beta} \sum_{k,\sigma} \sum_n \frac{1}{i\omega_n - \epsilon(\mathbf{k})} \frac{1}{i\omega_n + i\nu - \epsilon(\mathbf{k} + \mathbf{q})} \quad (5.20)$$

To perform the Matsubara frequency summation we define the function

$$f(z) := \frac{1}{z - \epsilon(\mathbf{k})} \frac{1}{z + i\nu - \epsilon(\mathbf{k} + \mathbf{q})} \frac{1}{e^{\beta z} + 1} \quad (5.21)$$

and consider the complex path integral

$$\frac{1}{2\pi i} \oint_{C_0(R)} f(z) dz \quad (5.22)$$

where the closed integration path $C_0(R)$ goes anticlockwise round a circle centred at $z = 0$ with radius $R \rightarrow \infty$. With know that with Cauchy's integral theorem the value of this integral is equal to the sum of the residues at all of the singularities enclosed in the path. The singularities of the function $f(z)$ are 1st order poles at $z = \epsilon(\mathbf{k})$, $z = \epsilon(\mathbf{k} + \mathbf{q}) - i\nu$ and along the imaginary axis at the Matsubara frequencies $z = i\omega_n$. So we have

$$\begin{aligned} \frac{1}{2\pi i} \oint_{C_0(R)} f(z) dz &= \text{Res}[f(z), z \rightarrow \epsilon(\mathbf{k})] \\ &+ \text{Res}[f(z), z \rightarrow \epsilon(\mathbf{k} + \mathbf{q}) - i\nu] \\ &+ \sum_n \text{Res}[f(z), z \rightarrow i\omega_n]. \end{aligned} \quad (5.23)$$

On the left hand side, the integral is equal to zero since $|zf(z)| \xrightarrow{R \rightarrow \infty} 0$ and the conditions for Jordan's lemma are fulfilled. The residue of $f(z)$ at one of the Matsubara frequencies is just $-\frac{1}{\beta} G_{k\sigma}^0(i\omega_n) G_{k+q\sigma}^0(i\omega_n + i\nu)$ and (5.23) becomes

$$\frac{1}{\beta} \sum_n G_{k\sigma}^0(i\omega_n) G_{k+q\sigma}^0(i\omega_n + i\nu) = \text{Res}[f(z), z \rightarrow \epsilon(\mathbf{k})] + \text{Res}[f(z), z \rightarrow \epsilon(\mathbf{k} + \mathbf{q}) - i\nu] \quad (5.24)$$

$$= \frac{n_F(\epsilon(\mathbf{k})) - n_F(\epsilon(\mathbf{k} + \mathbf{q}))}{i\nu + \epsilon(\mathbf{k}) - \epsilon(\mathbf{k} + \mathbf{q})} \quad (5.25)$$

¹Note that we could also get this from Feynman diagram rules by just recognising the two-particle correlation function in (5.9) together with the integral over τ as a simple diagram in the two-particle diagrammatic perturbation expansion

with the Fermi-function $n_F(\epsilon) = (e^{\beta\epsilon} + 1)^{-1}$. We can insert this result into (5.20) to obtain

$$\chi^{zz}(\mathbf{q}, i\nu) = -2 \frac{\mu_B^2}{N} \sum_k \frac{n_F(\epsilon(\mathbf{k})) - n_F(\epsilon(\mathbf{k} + \mathbf{q}))}{i\nu + \epsilon(\mathbf{k}) - \epsilon(\mathbf{k} + \mathbf{q})}. \quad (5.26)$$

The factor 2 just comes from summing over the spin σ .

Now we come to the point of all these calculations: The static magnetic susceptibility, i.e. taking $\nu = 0$, diverges for $\mathbf{q} \rightarrow (\pi, \pi)$ since, at half-filling, for a \mathbf{k} at the Fermi surface then $\epsilon(\mathbf{k}) - \epsilon(\mathbf{k} + \mathbf{q}) \rightarrow 0$ whereas the numerator in (5.26) will be finite. This a direct result of the diamond shape of the Fermi surface, there are many \mathbf{k} in the summation along each edge of the surface which contribute to the divergence of the susceptibility at (π, π) . The staggered magnetisation is then at its maximum for $\mathbf{q} = (\pi, \pi)$ which means for this oscillating response magnetisation that the wave-length λ , defined by $\mathbf{q} = (\frac{2\pi}{\lambda_x}, \frac{2\pi}{\lambda_y})$, is the same in both the x and y directions: $\lambda = 2$, and neighbouring spins are aligned antiferromagnetically. So we see that with $t' = 0$, we have perfect nesting of the Fermi surface at half-filling and the resultant magnetic instability in the susceptibility will cause AF order in the conduction electrons when they are placed into an infinitely small AF field. This could form the start point for the spin density wave (SDW) approach considered as part of chapter 4, where we lock-in a staggered magnetisation on the localised spins and allow the conduction electrons to move in this background.

To break the perfect nesting of the Fermi surface and remove the nesting enhancement of the magnetic order, we introduce a next-nearest neighbour hopping with matrix element $t' = -0.3$. The Hamiltonian in real space is therefore

$$H = -t \sum_{\langle i,j \rangle, \sigma} c_{i,\sigma}^\dagger c_{j,\sigma} - t' \sum_{\langle\langle i,j \rangle\rangle, \sigma} c_{i,\sigma}^\dagger c_{j,\sigma} + J \sum_{\mathbf{i}} \mathbf{S}_{\mathbf{i}}^c \cdot \mathbf{S}_{\mathbf{i}}^f \quad (5.27)$$

where $\langle i, j \rangle$ and $\langle\langle i, j \rangle\rangle$ represents nearest and next-nearest neighbours, respectively. The Fourier transform of the non-interacting part gives a modified dispersion

$$\epsilon(\mathbf{k}) = -2t [\cos(k_x) + \cos(k_y)] - 2t' [\cos(k_x + k_y) + \cos(k_x - k_y)] \quad (5.28)$$

resulting in a deformed Fermi-surface at half-filling. We will use $t'/t = -0.3$ which gives the dispersion shown in Fig. 5.1. The deformation of the Fermi-surface lifts the perfect nesting since we no longer have $\epsilon(\mathbf{k}) = \epsilon(\mathbf{k} + \mathbf{q})$ for a \mathbf{k} on the Fermi surface. However, we note that the static spin-susceptibility $\chi^{zz}(\mathbf{q})$ still displays a maximum at $\mathbf{q} = (\pi, \pi)$ such that this value of t'/t still will be a good choice for investigating the AF order-disorder transition of the KLM.

5.2 Magnetic Phase Transition at Half-Filling

In section 1.2 we discussed the competition between the magnetic ordering and the screening of the localised magnetic moments in the KLM and that the Kondo screened phase

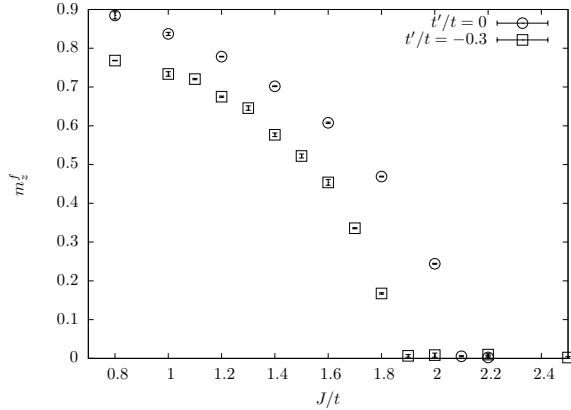


Figure 5.2: The staggered magnetisation m_z^f of the local moment spins as a function of coupling J/t . Results are shown for the ground state with next-nearest neighbour hopping $t'/t = -0.3$ and with $t'/t = 0$.

gives way to an AF ordered phase at a QCP as J/t is reduced at half-filling. Lattice QMC results show the phase transition to be at 1.45 ± 0.05 [33]. In order to capture the expected transition from the insulating paramagnetic Kondo-screened phase at large values of J/t to the AF-ordered insulator at low values of J/t the staggered magnetisation $m_z^f = \frac{1}{N_c} \sum_i \langle n_{i,\uparrow}^f - n_{i,\downarrow}^f \rangle e^{-i\mathbf{Q}\mathbf{r}_i}$ was measured. Hereby, N_c is just the number of original lattice sites in the cluster (i.e. for $N_c^{AF} = 4$ then $N_c = 8$) and $\mathbf{Q} = (\pi, \pi)$. This is a local quantity and as such the value measured during the QMC cluster solver part of the DCA calculation is equal to the value which would be obtained from the full lattice Green function [37]. We remember also that the staggered magnetisation can be measured in our DCA approach only because AF ordering is allowed for through the definition of the two-site unit cell.

In Fig. 5.2, m_z^f is shown as a function of the coupling J/t with and without next-nearest neighbour hopping. Importantly, the DCA results for the particle-hole symmetry case ($t'/t = 0$) are in qualitative agreement with known results: We track a continuous phase transition from magnetic disordered to AF ordered with decreasing coupling J/t . However, we note that the DCA results give a critical J/t which is shifted to a higher value in comparison to the lattice QMC results. We obtain $\frac{J_c}{t} \approx 2.1$. It is not so concerning that the DCA does not reproduce J_c from the lattice QMC measurements, because the measurements displayed here were with only $N_c^{AF} = 1$. By definition of the DCA, as N_c^{AF} is increased the numerical value of all the DCA results must approach the QMC lattice results because ultimately we would reach the limit $N_c^{AF} = N$ so that the cluster is the size of the lattice and the DCA is per definition exact. However, what interests us here is that the qualitative behaviour of the transition is reproduced by our approach, albeit at

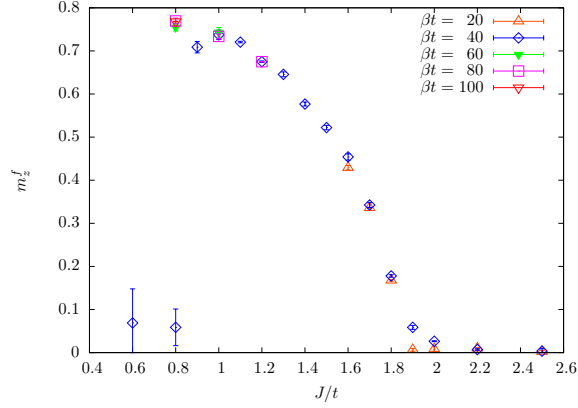


Figure 5.3: Staggered magnetisation as a function of coupling J/t with $t' = -0.3$ but now also showing data for different temperatures for comparison.

a different transition coupling J_c/t . As could be expected by the removal of the nesting induced magnetic instability, the breaking of particle hole symmetry, by using $t'/t \neq 0$, suppresses the onset of magnetism ($J_c/t \approx 1.85$).

On the technical side, in order to ensure that a given result can be considered to be a ground state result it was necessary to perform simulations at a variety of inverse temperatures β . The energy scales in the problem, the Kondo scale, coherence scale and the RKKY scale, all become smaller with smaller J/t .

In Fig. 5.3 we show the same magnetisation plot for $t' = -0.3$ as before (Fig. 5.2) but include some measured values at different temperatures. We point out that $\beta t \leq 40$ is unsuitable for $J/t < 1$, since we are obviously not below the Neel temperature for those values of J/t . However $\beta t = 40$ is suitable for $1 \leq J/t \leq 1.6$ whereas we consider $\beta t = 20$ sufficiently large for simulations with $J/t > 1.6$. In later results for the doped KLM we expect lower temperatures will be required in order to consider the results to be for the ground state because the chemical potential will no longer be in a gap and therefore the smearing out of the spectral function due to thermal fluctuations may play a greater role.

5.3 Single Particle Spectrum - $t'/t = 0$

We now show the DCA results for $t'/t = 0$, the particle-hole symmetric case. The single particle spectrum $A(\mathbf{k}, \omega) = -\frac{1}{\pi} \Im G_{cc}^{ret}(\mathbf{k}, \omega)$ of the conduction electrons is plotted for \mathbf{k} vectors along a path of high symmetry in the first Brillouin zone: $(\pi, \pi) \rightarrow (0, \pi) \rightarrow (0, 0) \rightarrow (\pi, \pi)$. As described in section 2.4.1, in the case of AF ordering, the true first Brillouin zone would be reduced to the diamond shape, but we will continue to show the results for the path indicated, in what we will then call the *extended* Brillouin zone, so

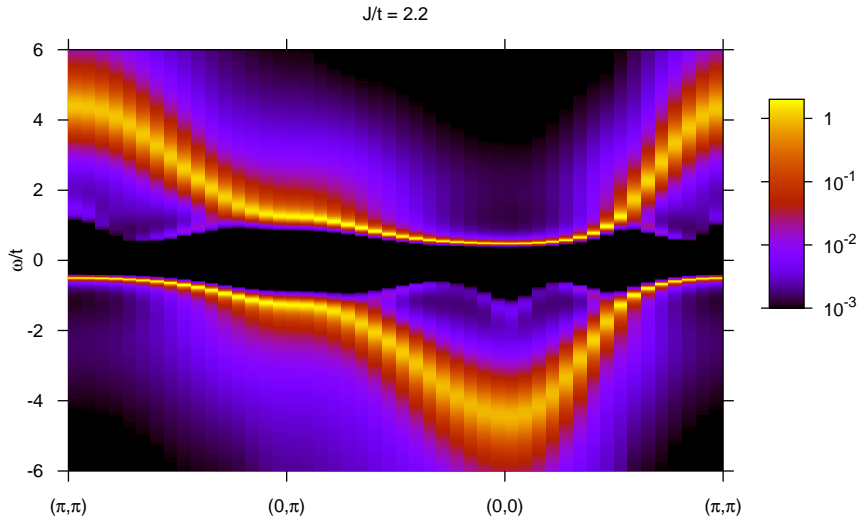


Figure 5.4: Single particle spectral function for a simulation at half-filling ($\langle n_c \rangle = 1$) and with particle-hole symmetry ($t' = 0$) close to the magnetic phase transition on the paramagnetic side, $J/t = 2.2$.

as to make direct comparison with the PM case. On the energy axis, ω values are given relative to the Fermi energy (i.e. $E_F \equiv [\omega = 0]$) which is fixed by the value of μ .

In Fig. 5.4 we plot the spectrum for $J/t = 2.2$, which was seen to be in the paramagnetic phase (see Fig. 5.2). The first notable feature is the quasi-particle gap: no band crosses the Fermi energy ($\omega = 0$). In section 5.5 we examine the QP gap in detail as a function of J/t . For now, it is enough to note that a finite gap in the conduction electron spectrum indicates that the state is insulating. The lower band runs very flat around $\mathbf{k} = (\pi, \pi)$, with relatively low spectral weight (note the logarithmic scale of the colour chart) in comparison to the other parts of the band which are mostly unchanged from the non-interacting case. The flat band feature is associated with Kondo screening of the impurity spins and the resultant heavy fermion nature of the composite quasi-particles, where a large effective mass is given by the very small curvature of the band, We will later also see such flat bands in the hole doped phase to be discussed later.

At $J/t = 2.0$ we have measured a non-vanishing staggered magnetisation $m_z^f = 0.244 \pm 0.001$. The spectral function (Fig. 5.5, left: for the complete path in k -space, right: showing a close-up for $\mathbf{k} = (0, 0) \rightarrow (\pi, \pi)$) for this lightly AF ordered simulation now includes additional low energy band structures: In the upper band around (π, π) and in the lower band around $(0, 0)$. The features are directly linked with the magnetic ordering. These are so-called *shadow bands*, arising due to a reduction of the Brillouin zone, applicable for the system when spin symmetry between neighbouring sites is broken. In the case

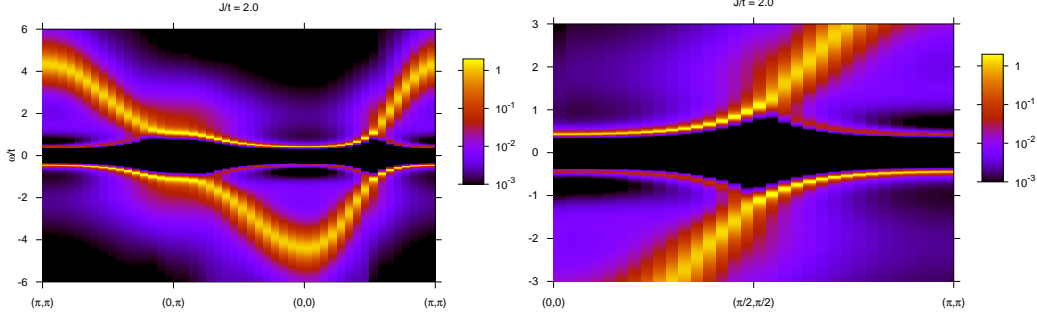


Figure 5.5: Single particle spectral function for a simulation at half-filling ($\langle n_c \rangle = 1$) and with particle-hole symmetry ($t' = 0$) close to the magnetic phase transition on the AF side, $J/t = 2.0$. The staggered magnetisation for this point is measured to be $m_z^f = 0.244 \pm 0.001$.

of AF ordering, two k -points separated by the AF ordering vector $\mathbf{Q} = (\pi, \pi)$ become equivalent. We can also say, on example of the lower band, that the heavy fermion part of the band around (π, π) is *backfolded* around $(\frac{\pi}{2}, \frac{\pi}{2})$, reflecting the AF reduced Brillouin zone. The point $(\frac{\pi}{2}, \frac{\pi}{2})$ lies at the edge of the true first Brillouin zone so that moving along a path in k -space towards the zone centre at $(0, 0)$ is equivalent to moving towards the centre of the neighbouring Brillouin zone at (π, π) . If we look back at the spectrum for $J/t = 2.2$ (Fig. 5.4) we can interpret the faint low spectral weight, low energy structure in the photoemission ($\omega < 0$) spectrum around $\mathbf{k} = (0, 0)$ as pre-cursor signs of AF ordering. In our DCA approach we begin a simulation with non-equal up/down-spin Green functions, setting an artificial magnetisation which, when iterated to convergence within the DCA/QMC solving process, will either vanish or stabilise depending on whether the parameters J/t and $\langle n_c \rangle$ produce a PM or AF state, respectively. For the PM state we will never achieve $G_\uparrow = G_\downarrow$ *exactly*, but only within our error bars. Therefore, particularly in the neighbourhood of the quantum phase transition, where convergence of the iterative process becomes critically slow, weak indications of backfolding are understandable.

Fig. 5.6 shows no qualitative differences to the previous plot, but we are deeper in the magnetically ordered phase and the shadow band have a larger spectral weight. We note that the gap between the lower and upper has progressively become smaller going from $J/t = 2.2$ to $J/t = 1.6$, and will be analysed in section 5.5.

At $J/t = 1.2$ we make an important comparison with the spectrum obtained via QMC lattice simulations (using the projective auxiliary field algorithm of [33]) for the same parameters. We see in Fig. 5.7 the QMC lattice simulation results [33] on the left and our DCA result on the right, both only for the ($\omega < 0$)-photoemission spectrum. The agreement of the DCA spectrum with the BSS result is excellent. The BSS result suffers aesthetically from the fact that since the simulations were carried out on a finite lattice

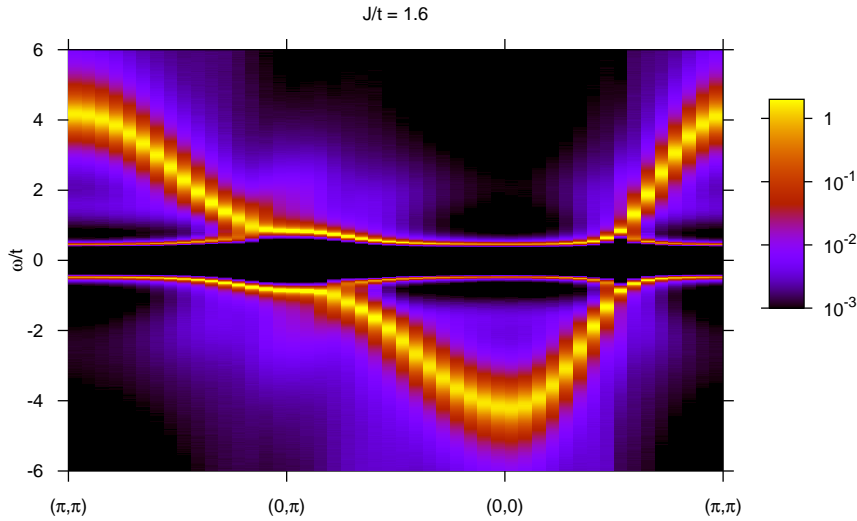


Figure 5.6: Single particle spectral function at half-filling ($\langle n_c \rangle = 1$), with particle-hole symmetry ($t' = 0$) and with coupling $J/t = 1.6$ giving rise to intermediate strength AF ordering. The staggered magnetisation is measured as $m_z^f = 0.608 \pm 0.002$.

(here a 12×12 lattice) spectral data is only available for that limited number of points in k -space, at least without some interpolation method to smooth out the plot. The DCA plot is smoother in k -space because the DCA self-energy, in the case of $N_c^{AF} = 1$ is not k -dependent so that we may calculate the lattice Green function and extract from it the spectral function for any desired k -vector.

It is quite remarkable that already with the smallest possible cluster capable of capturing AF order, $N_c^{AF} = 1$, we are able to produce a single particle spectrum which is basically exactly the same as the lattice QMC result. This confirms that the DCA is indeed a well suited approximation for use with the KLM: the essence of the competition between RKKY-mediated spacial magnetic order and the time displaced correlations responsible for Kondo screening is successfully distilled to a small cluster dynamically embedded in the mean-field of the remaining bath electrons.

Before moving on to results for $t'/t = -0.3$ we consider the position of the band maxima and minima. The lower band maximum remains at $\mathbf{k} = (\pi, \pi)$ for all J/t down to at least $J/t = 1.0$. In the upper band the minimum is always at $(0, 0)$. Therefore in the PM region we have an indirect gap with momentum transfer vector $\mathbf{q} = (\pi, \pi)$ (and rotationally equivalent vectors). At $J/t = 0.8$ the band becomes practically flat from $(0, 0)$ to (π, π) and the maximum is hard to determine. Further discussion on this point will be made later in section 5.5. In the AF phase, the backfolding of the upper and lower bands means that the minimum and maximum of the two bands are also found at vectors $\mathbf{q} = \mathbf{k}_{max/min} + \mathbf{Q}$,

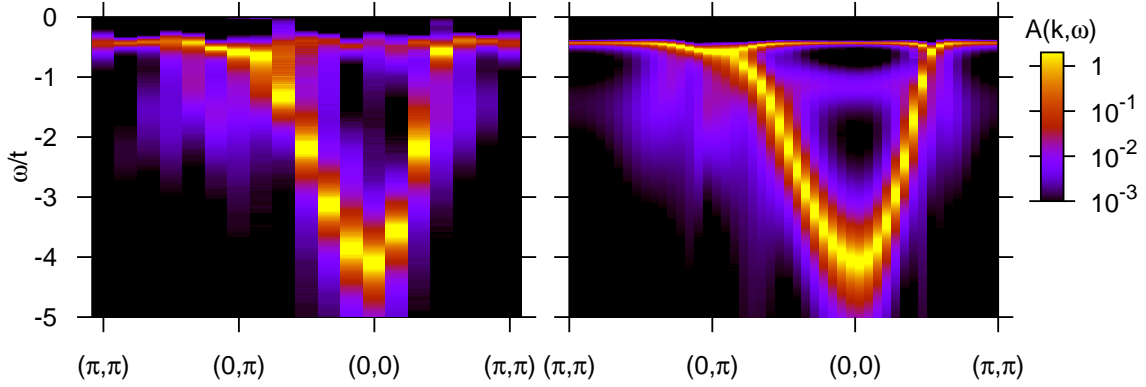


Figure 5.7: Comparison of single particle spectra for the conduction electrons with previous results: left, data taken from [33] which used a projective auxiliary field Monte Carlo method on a finite lattice KLM. right, our DCA results for the same parameter set - $t' = 0$, $\langle n_c \rangle = 1$, $J/t = 1.2$.

with $\mathbf{Q} = (\pi, \pi)$ and rotational symmetry equivalents. We therefore have a direct gap for the AF phase.

5.4 Single Particle Spectrum - $t'/t = -0.3$

We now report on the results for the case where particle hole symmetry is broken by the inclusion of the next-nearest neighbour hopping term $t'/t = -0.3$. In the absence of particle-hole symmetry, the chemical potential for a simulation can no longer simply be set to $\mu = 0$ to achieve $\langle n_c \rangle = 1$ i.e. half-filling. However, for larger values of J/t the charge gap is sufficiently large such that only a few guesses for the chemical potential were needed in order to land in the gap. On the basis of these results it is then possible to extrapolate the required value of μ successively for simulations with smaller J/t .

In the PM phase with $J/t = 2.5$ (see Fig. 5.8) the spectrum is qualitatively identical to the PM phase in the $t' = 0$ case. The model is insulating with an indirect gap. The underlying free dispersion relation is modified by the inclusion of next-nearest neighbour hopping, hence the different energy span of the spectrum. In this plot we already begin to observe some extremely weak precursors to magnetic order in the form of backfolding in the lower band.

At $J/t = 2.0$ and $J/t = 1.9$, shown in Figs. 5.9 and 5.10 respectively, the system is still paramagnetic (see the magnetisation plot of Fig. 5.2). For $J/t = 1.9$ in particular though, we see the same sort of precursor effect to backfolding seen for $t' = 0$, $J/t = 2.2$ (Fig. 5.4). The backfolded band forms more fully only with $J/t = 1.8$ (Fig. 5.11) and gains spectral weight by $J/t = 1.6$ (Fig. 5.12). In Figs. 5.13, 5.14, and 5.15 we continue to follow the

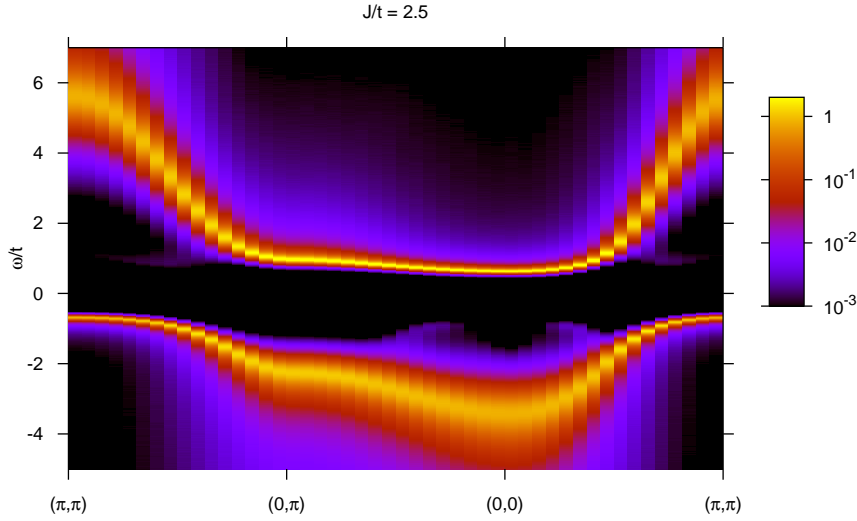


Figure 5.8: Single particle spectral function at half-filling ($\langle n_c \rangle = 1$), away from particle-hole symmetry ($t' = -0.3$). The coupling $J/t = 2.5$ sets the point on the paramagnetic side of the phase transition.

changes in the spectrum for $J/t = 1.5, 1.4$ and 1.3 . For the moment we focus on k -vectors along the line from $(0, 0)$ to (π, π) (shown in the close-up plots on the right of these figures). The local minimum energy dip at $\mathbf{k} = (\frac{\pi}{2}, \frac{\pi}{2})$ becomes less pronounced as the heavy fermion band flattens until by the time we reach $J/t = 1.2$ this dip has turned into a bump such that the lower band maximum has shifted from (π, π) to $(\frac{\pi}{2}, \frac{\pi}{2})$. Although this important change in band structure appears to be continuous, it is unlikely, even if we had data for $1.3 > J/t > 1.2$, to be clear whether the band maximum truly shifts continuously along the path between the two positions due to limits in the resolution of the underlying QMC result (compare also section 5.5 for the method used for resolving band maxima or minima). For smaller $J/t = 1.1, 1.0$, and 0.8 the spectra are shown in Figs. 5.17, 5.18 and 5.19 respectively, now only for the path from $(0, 0)$ to (π, π) . The lower band maximum remains at $(\frac{\pi}{2}, \frac{\pi}{2})$ and becomes more pronounced.

If we now consider the position of the minimum in the upper band, following the evolution of the spectra again from large J/t in the paramagnetic region down to low J/t in the AF phase, we see that for $2.5 \geq J/t \geq 1.6$ (Figs. 5.8 - 5.12) the upper band minimum is at $\mathbf{k} = (0, 0)$ whereas for $1.5 \geq J/t \geq 0.8$ the band minimum is at $\mathbf{k} = (0, \pi)$. The position of the minima and maxima in the upper and lower bands of the spectra for $t'/t = -0.3$ are summarised schematically in Fig. 5.20.

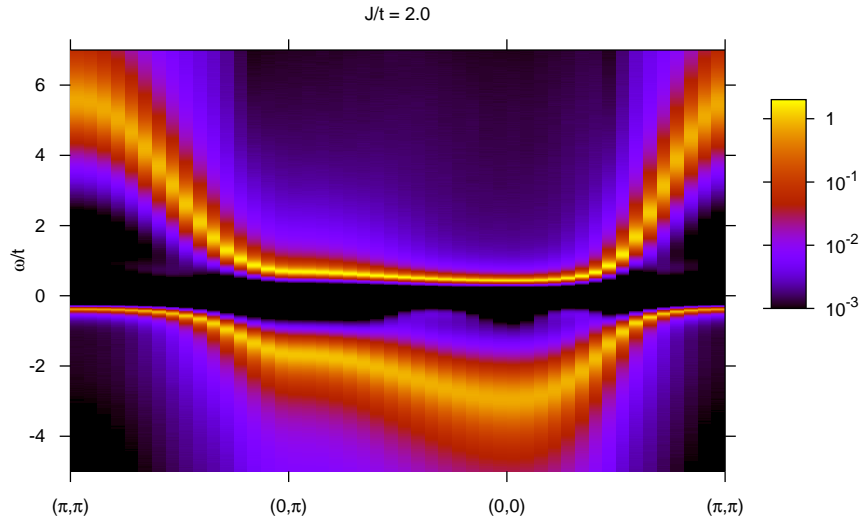


Figure 5.9: Single particle spectral function at $J/t = 2.0$, with $\langle n_c \rangle = 1$, $t' = -0.3$. These parameters set the simulation in the paramagnetic region close to the magnetic phase transition.

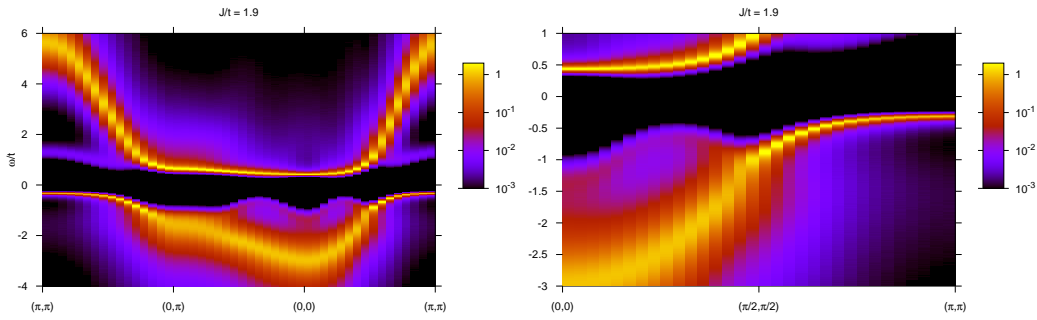


Figure 5.10: Single particle spectral function with $J/t = 1.9$, $\langle n_c \rangle = 1$, $t' = -0.3$, still just on the paramagnetic side of the phase transition.

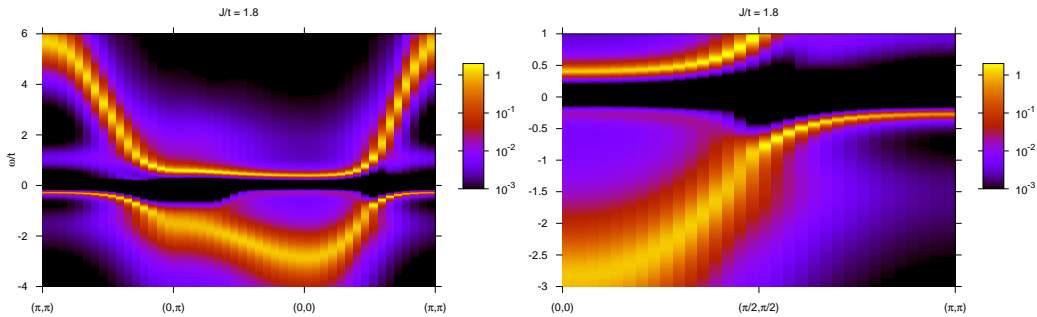


Figure 5.11: Single particle spectral function with $J/t = 1.8$, $\langle n_c \rangle = 1$, $t' = -0.3$, just inside the AF ordered phase.

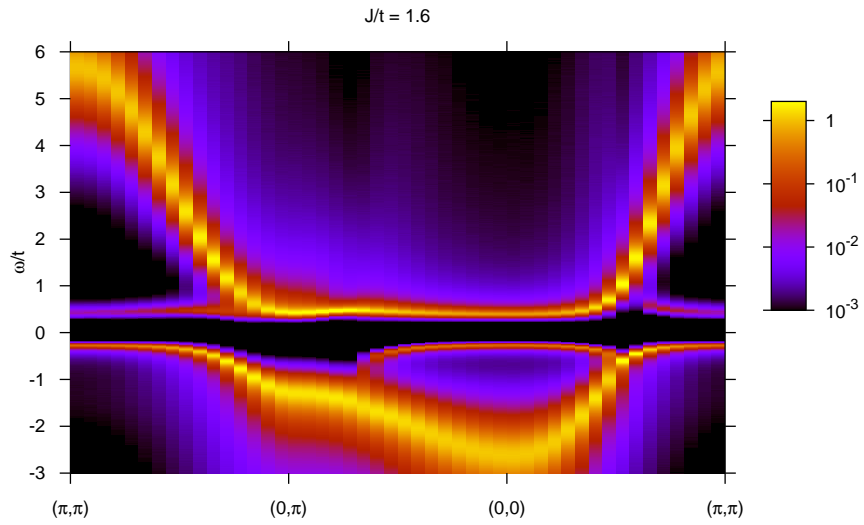


Figure 5.12: Single particle spectrum for $J/t = 1.6$, $\langle n_c \rangle = 1$, $t' = -0.3$.

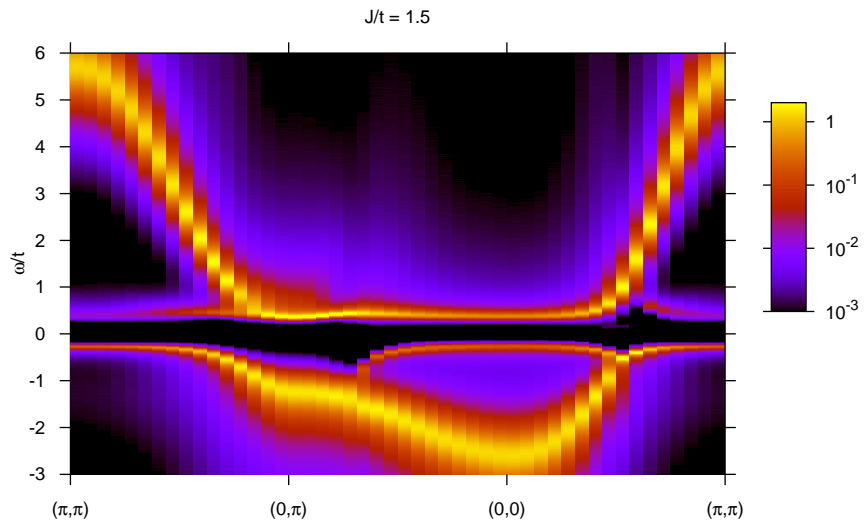


Figure 5.13: Single particle spectrum for $J/t = 1.5$, $\langle n_c \rangle = 1$, $t' = -0.3$.

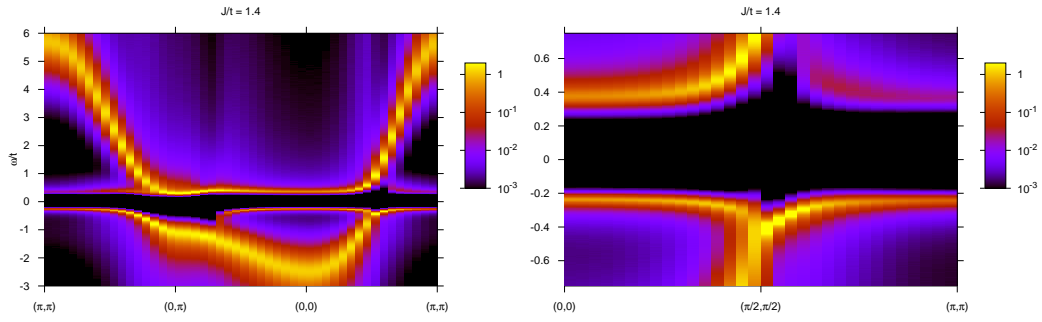


Figure 5.14: Single particle spectrum for $J/t = 1.4$, $\langle n_c \rangle = 1$, $t' = -0.3$.

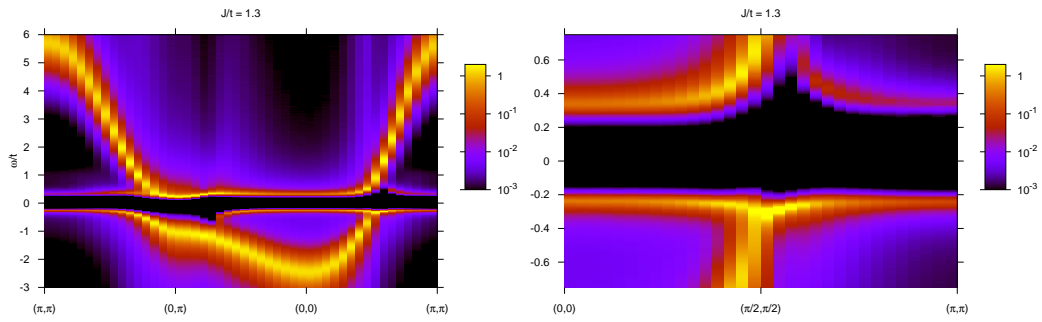


Figure 5.15: Single particle spectrum for $J/t = 1.3$, $\langle n_c \rangle = 1$, $t' = -0.3$.

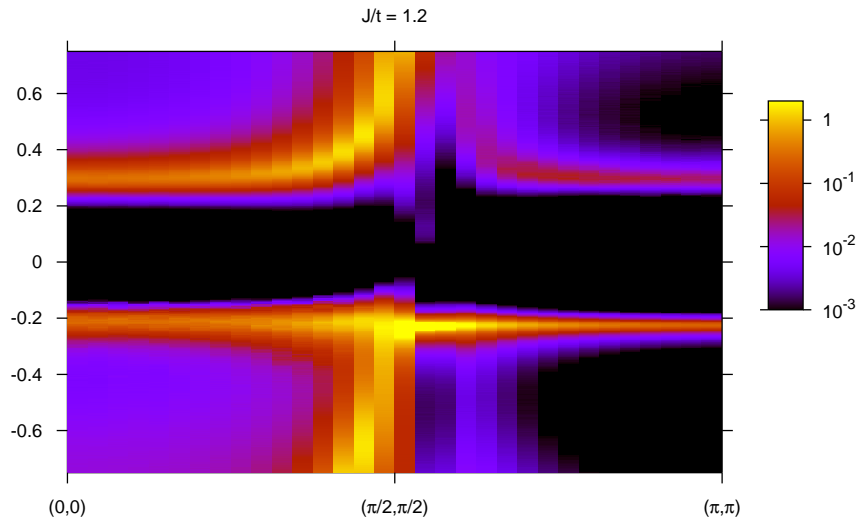


Figure 5.16: Single particle spectrum for $J/t = 1.2$, $\langle n_c \rangle = 1$, $t' = -0.3$.

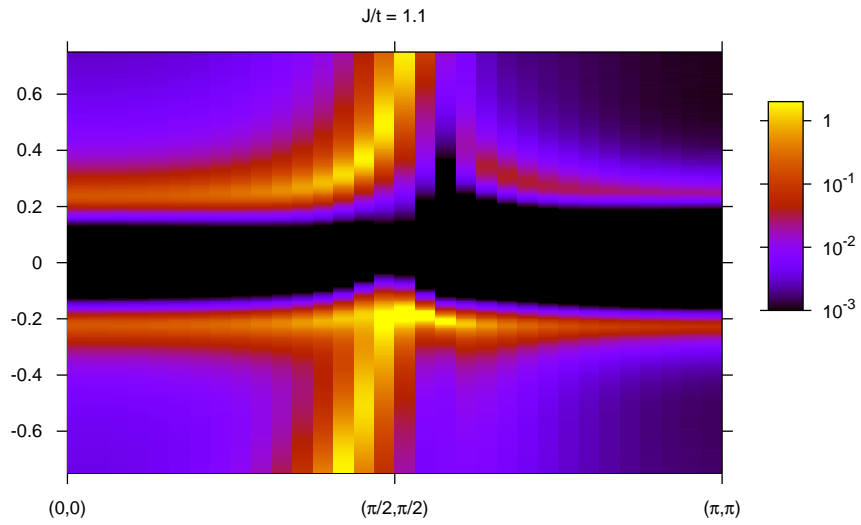


Figure 5.17: Single particle spectrum for $J/t = 1.1$, $\langle n_c \rangle = 1$, $t' = -0.3$.

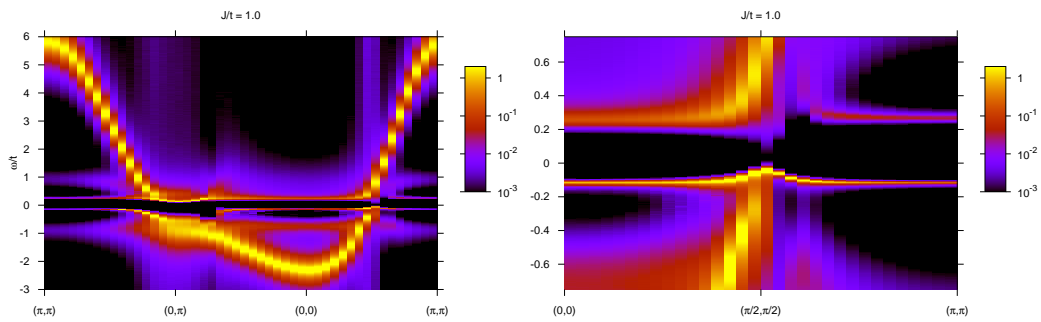


Figure 5.18: Single particle spectrum for $J/t = 1.0$, $\langle n_c \rangle = 1$, $t' = -0.3$.

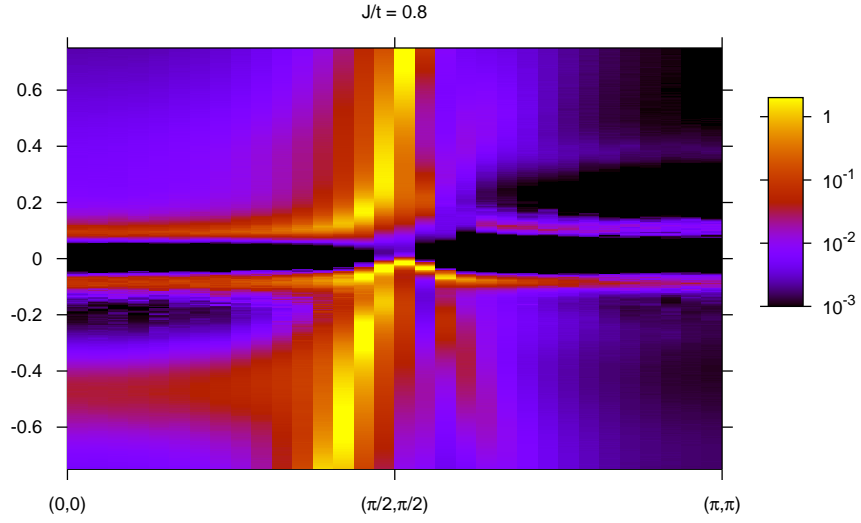


Figure 5.19: Single particle spectrum for $J/t = 0.8$, $\langle n_c \rangle = 1$, $t' = -0.3$.

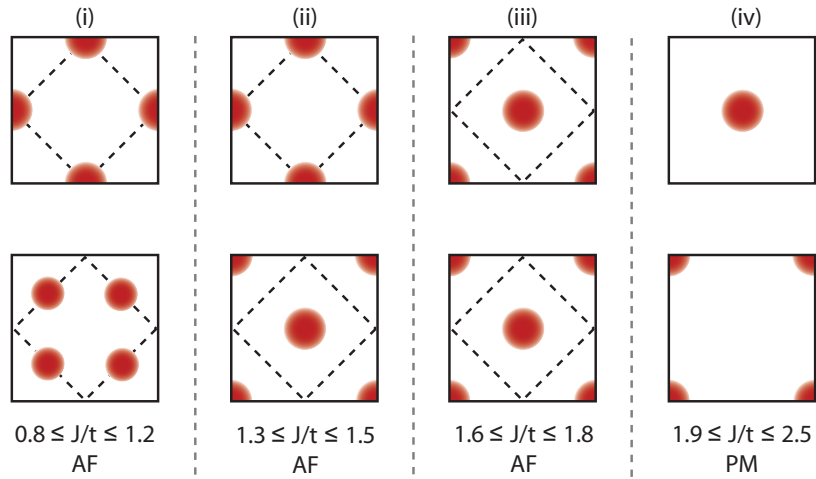


Figure 5.20: Schematic representation of the position of the upper band minima (top row) and lower band maxima (bottom row) of the conduction electron single particle spectral function with next-nearest neighbour hopping $t' = -0.3$ and for half-filling. The squares represent the 1st Brillouin zone (for the PM phase) or the extended Brillouin zone (for the AF phase), with the bottom left corner and top right corner of each square given by $\mathbf{k} = (-\pi, -\pi)$ and $\mathbf{k} = (\pi, \pi)$, respectively.

5.5 The Quasi-Particle Gap

The quasi-particle gap Δ_{qp} is the energy difference between the ground states of the $N + 1$ electron system and the N electron system. For an insulator, a finite quasi-particle gap will show up in the quasi-particle dispersion relation (the single particle spectrum). According to Landau Fermi liquid theory for quasiparticles an extra electron added to the correlated system will lose its single electron character and be assimilated into the pool of composite quasiparticles. The energy difference of the $N + 1$ and N electron ground states will give the energy required for the lowest quasiparticle excitation. In contrast, the charge gap is the lowest energy required for a change in the charge configuration whilst holding the number of electrons constant. For the Kondo insulator the charge gap is just twice the quasiparticle gap. Just by looking at the spectra of the previous section it can be difficult to read off a reliable estimate for the gap. An easier method is to read the gap from the imaginary time lattice Green function for the conduction electrons $G_{\mathbf{k}}(\tau) = -\langle T_{\tau} a_{\mathbf{k}}(\tau) e a_{\mathbf{k}}^{\dagger}(0) \rangle$. In spectral representation, by inserting the same complete set of eigenstates $|E_n\rangle$ to H that we use to build the trace, this may be written as

$$G_{\mathbf{k}}(\tau) = -\frac{1}{Z} \sum_{n,m} |\langle E_n a_{\mathbf{k}} | E_m \rangle|^2 e^{\tau(E_n - E_m)} e^{-\beta E_n} \quad (5.29)$$

for $\tau > 0$, for example, where the Green function describes inverse photoemission processes. In the $T = 0$ limit $\beta \rightarrow \infty$ and the only term we need in the sum over n is the ground state $n = 0$. In this case the asymptotic behaviour of the Green function for large τ becomes

$$G_{\mathbf{k}}(\tau) \xrightarrow{\tau \rightarrow \beta} -|\langle E_0 | a_{\mathbf{k}} | E_1 \rangle|^2 e^{-\tau E_1}, \quad (5.30)$$

therefore an exponential decay controlled by the lowest excitation energy E_1 , which will be equivalent to the quasiparticle gap. For $\tau < 0$, corresponding to photoemission, the spectral representation gives

$$G_{\mathbf{k}}(\tau) \xrightarrow{\tau \rightarrow -\beta} |\langle E_0 | a_{\mathbf{k}}^{\dagger} | E_1 \rangle|^2 e^{\tau E_1}. \quad (5.31)$$

In our simulations, β is large but not infinite. The Matsubara Green functions are anti-periodic with period β (i.e. $G(-\tau) = -G(\beta - \tau)$). Inverse photoemission is described by our Green function for $0 \leq \tau \lesssim \frac{\beta}{2}$ whereas the photoemission processes are described for $\frac{\beta}{2} \lesssim \tau < \beta$. We can therefore determine the lowest excitation energies by linearly fitting to a logarithmic plot of the Green function $G_{\mathbf{k}}(\tau)$ (at the momentum vector of the gap) and reading off the slope.

The quasi-particle gap measured as a function of J/t is shown in Fig. 5.21 with ($t'/t = -0.3$) and without ($t'/t = 0$) next-nearest neighbour hopping. We note first that the known linear dependence of Δ_{qp} on J/t for $t'/t = 0$ and small J/t [33] is reproducible in the DCA approach. This linear behaviour has been interpreted in [33] as being linked

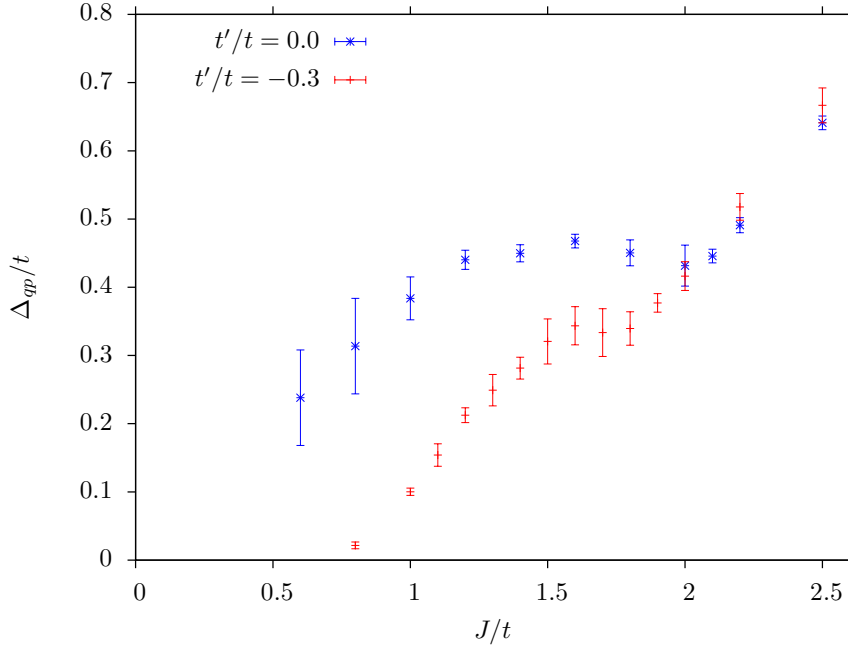


Figure 5.21: The quasi-particle gap Δ_{qp}/t as a function of antiferromagnetic coupling J/t for the two cases of $t' = 0$ and $t'/t = -0.3$.

to the magnetic ordering (which sets in before the linear region at higher J/t) and, in particular, the nesting instability to AF order in the particle-hole symmetric case. In the framework of the SDW approximation, we would expect a gap $\Delta_{qp} \propto J/t$ (4.13). In contrast to this, away from the particle-hole symmetric point with $t' = -0.3$ the gap is greatly suppressed for small J/t and is consistent with an exponential decay. Again, this can be considered as consistent with the SDW framework since for $t'/t = -0.3$ the gap proportional to J/t is lost (see back to Fig. 4.2). We can therefore assume that the gap follows a Kondo scale and that its nature is that of a hybridisation gap which decreases exponentially for small J/t as the RKKY scale wins out over the Kondo scale. This is the generic result whereas the linear dependency on J/t is given only for the special particle-hole symmetric case with perfectly nested Fermi surface for free electrons.

6 The Hole-Doped KLM

6.1 Magnetic Phase Diagram

We have carried out numerous simulations in the hole-doped phase. This is achieved simply by reducing the chemical potential away from the half-filling value. For the case with $t'/t = 0$, where at half-filling $\mu = 0$, we move to negative values of μ noting that in order to achieve hole-doping, we must first reduce μ significantly enough in order to move out of the quasi-particle gap. For $t'/t = -0.3$ at half-filling μ already has a negative value which is then reduced further to dope with holes, where again we must first reduce enough to shift the Fermi energy E_F out of the gap. Since we are only considering hole-doping the changes in the lower band will be significant for the Fermi-surface of the doped model. The half-filling results showed the typical flat hybridisation band in the paramagnetic region with lower band maxima at (π, π) . As J/t was reduced the lower band was first backfolded, developing shadow bands with the onset of antiferromagnetism at the QCP. With further reduction of J/t , the magnetisation strengthened and the band maxima shifted from (π, π) to $(\frac{\pi}{2}, \frac{\pi}{2})$. Although at half-filling we cannot talk of Fermi surfaces, it is tempting to assume a rigid band theory, as argued in the following. The periodic Anderson model (PAM) is a band insulator at half-filling, as can be seen by considering the non-interacting $U_f = 0$ case where the energy dispersion would just be $E(\mathbf{k}) = \pm \sqrt{\epsilon(\mathbf{k})^2 + V^2}$. Now since the KLM is just the large U_f limit of the PAM we can also argue that the half-filled KLM is a band insulator, such that upon doping the holes will form around the lower band maxima of the half-filling spectrum. This would mean a topological change in the Fermi surface, a so-called Lifshitz transition [51], would occur on reducing the coupling whilst remaining inside the AF phase. In the following section we explore the ground state magnetic phase diagram for the hole-doped KLM, i.e. $\langle n_c \rangle < 1$. We begin with several lines at constant J/t in parameter space and vary the hole doping, before moving on to examine the spectral function from which we can read out the Fermi surface in the hole-doped metallic phase.

6.2 Staggered Magnetisation

Fig. 6.2 shows the staggered magnetisation as a function of conduction electron density for $J/t = 0.8, 1.0, 1.2$ and 1.4 . The magnetically ordered state found at half-filling therefore survives when moving away from these points by doping with holes. At all coupling

values a continuous magnetic phase transition is observed with the AF order decreasing gradually as the system is doped and vanishing smoothly at a quantum critical point. Checks were made by varying the temperature, $1/\beta$, of the simulations to ensure that the results can be considered to be ground state. The temperature must be low enough as to ensure that we are below the smallest scale of the problem: the coherence scale and/or the RKKY scale. Since the coherence scale decays exponentially with J/t we are limited to values of $J/t \geq 0.8$. This restriction arises since the computational time required by the QMC cluster solver scales as $(\beta N_c^{AF})^3$ [34]. On general grounds, we remember, we expect fuller magnetism at small values of J/t since in this region the RKKY scale set by $J^2\chi(\mathbf{q}, \omega = 0)$ dominates over the Kondo scale, $T_K \sim e^{-t/J}$. Here, $\chi(\mathbf{q}, \omega = 0)$ corresponds to the spin susceptibility of the conduction electrons. The results show, that upon doping, the magnetic metallic state progressively dominates the phase diagram as a function of decreasing coupling.

6.3 Single Particle Spectrum and Topology of the Fermi Surface

As we did for the half-filling results section we plot the single particle spectrum $A(\mathbf{k}, \omega) = -\text{Im}G_{cc}^{ret}(\mathbf{k}, \omega)$ in an extended Brillouin zone scheme and track its evolution, this time with increasing hole-doping away from half-filling. We begin with a line in the magnetic phase diagram at constant coupling $J/t = 1.0$ and plot the spectra for several points shown in the magnetisation graph for this coupling (Fig. 6.1(b)). The plots display only the line $(0, 0)$ to (π, π) in k-space, as it is here that a change in the Fermi-surface topology becomes evident. Fig. 6.2(a), where $\langle n_c \rangle = 1$, is shown again for comparison before doping the system.

Evidently, upon initial doping (Fig. 6.2(b)) a Fermi-surface forms comprised of hole pockets around $(\frac{\pi}{2}, \frac{\pi}{2})$. With further doping this low energy band flattens out progressively becoming almost flat by $\langle n_c \rangle = 0.926$ (Fig. 6.2(d)). Doping further still gives rise to a Fermi surface with holes centred on (π, π) (and equivalent points by rotational symmetry of the square lattice). Since at $\langle n_c \rangle = 0.908$ (Fig. 6.2(e)) and $\langle n_c \rangle = 0.898$ (Fig. 6.2(f)) we still have non-zero magnetisations of $m_z^f = 0.340$ and $m_z^f = 0.245$, respectively, then backfolding of the band produces a hole at $(0, 0)$ although there, due to the proximity of the upper band with small positive energy relative to the chemical potential, the band is somewhat smeared out or hard to resolve. In Fig. 6.2(g) the magnetisation is very small ($m_z^f = 0.123$) such that the backfolded band begins to weaken. In the final figure of the series, the magnetisation is practically zero, and consequently, the backfolded band has vanished leaving a Fermi-surface given solely by holes around (π, π) (and equivalent points).

To gain insight into these DCA results we can draw on the mean-field approaches in-

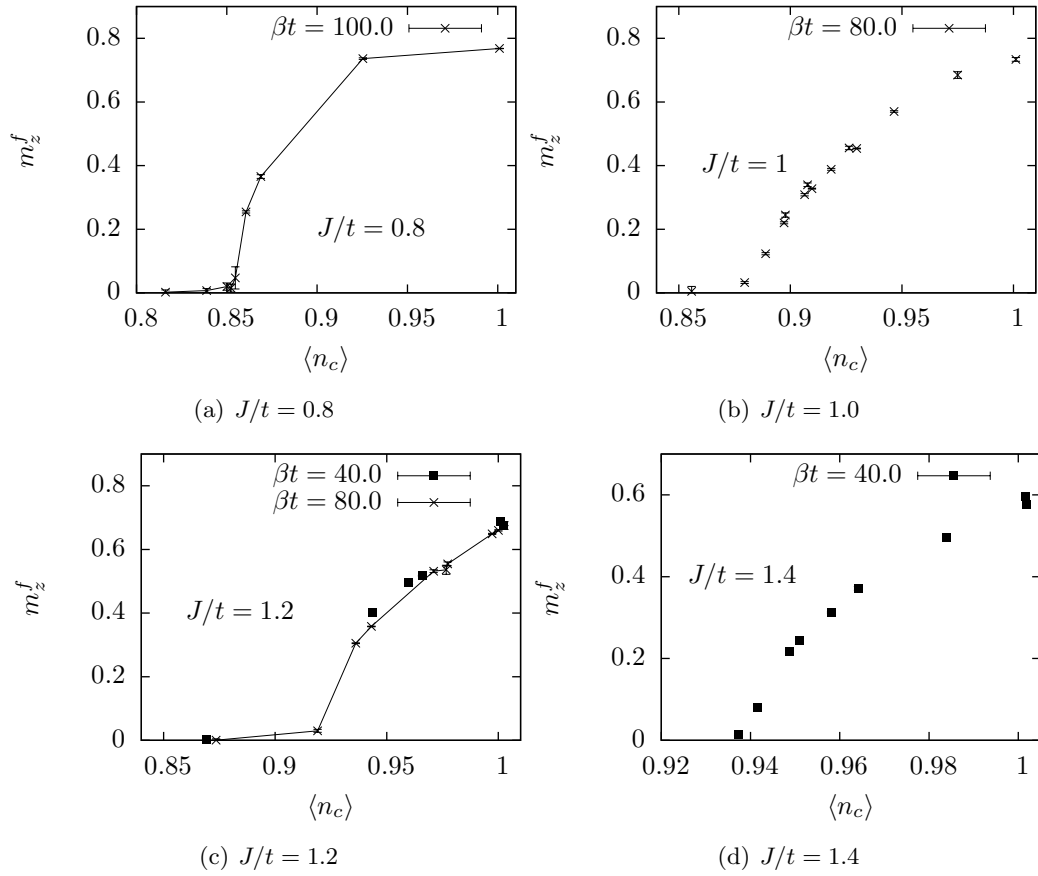


Figure 6.1: The staggered magnetisation m_z^f of the f -electrons as a function of $\langle n_c \rangle$ at different constant couplings J/t

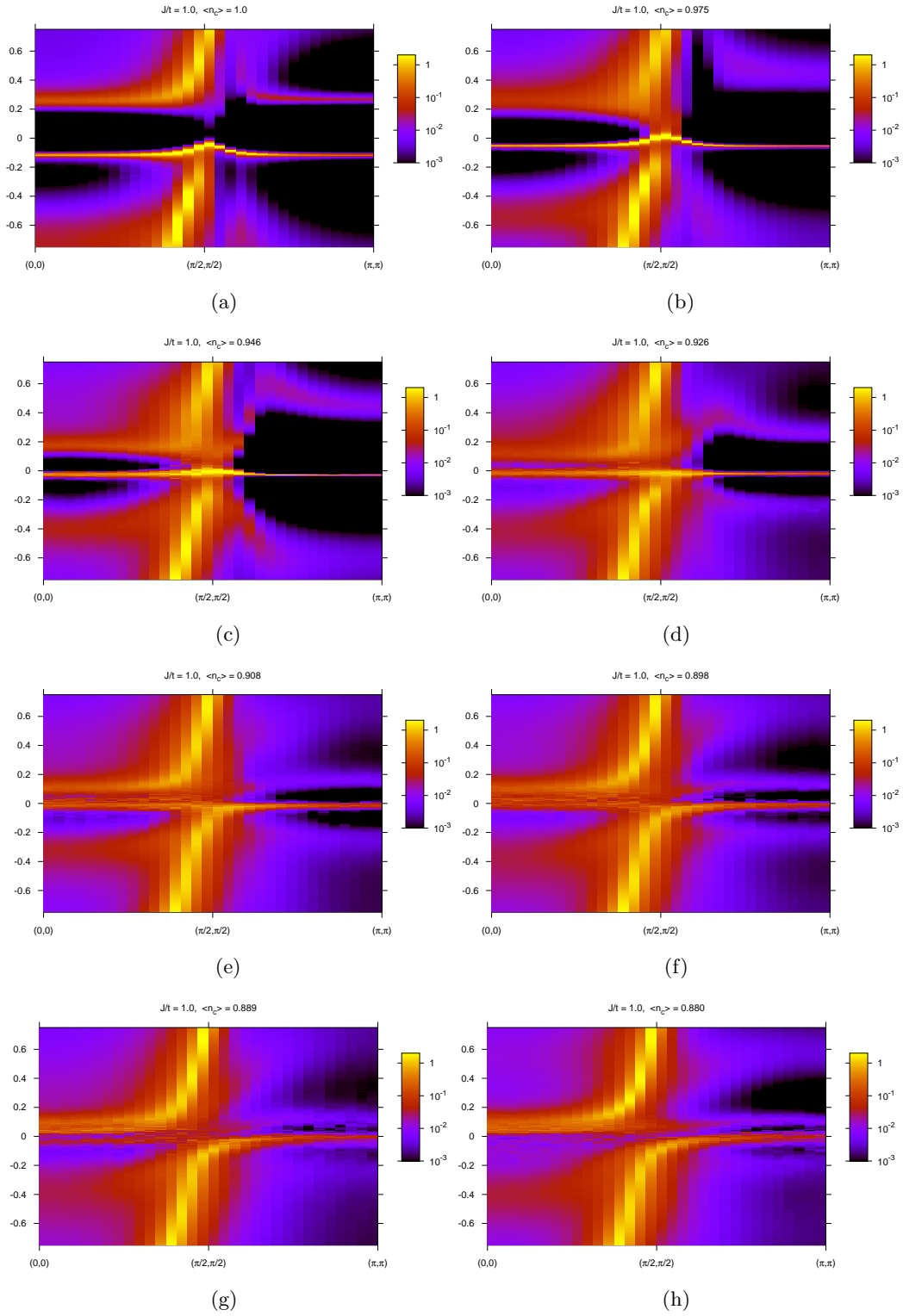


Figure 6.2: Single particle spectrum of the conduction electrons for $J/t = 1$. The conduction electron density is reduced progressively (conduction electron density value displayed above figures) in the series of figures from half-filled $\langle n_c \rangle = 1$ in (a) to $\langle n_c \rangle = 0.880$ in (h). The y-axis is ω/t and the x-axis gives k-vectors along the straight path from $(0, 0)$ to (π, π)

roduced in chapter 4. The mean-field approximation of Zhang and Yu [50] with the Hamiltonian given by (4.18) results in a four-band energy dispersion relation, $E_n(\mathbf{k})$, in the MBZ. For this mean-field Hamiltonian the Luttinger sum rule reads:

$$\frac{2}{N_{MBZ}} \sum_{\mathbf{k} \in MBZ, n} \Theta(-E_n(\mathbf{k})) = 2(n_f + n_c) \equiv 2(1 + n_c) \quad (6.1)$$

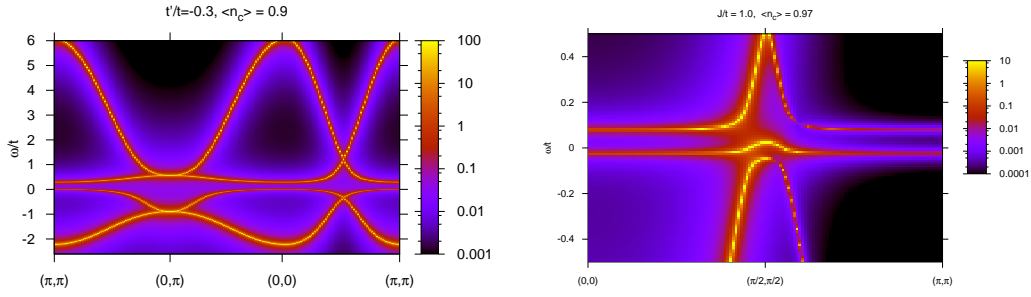
where we carefully note that N_{MBZ} stands for the number of AF unit cells (i.e. two f -electron orbitals and two c -electron orbitals) such that $N_{MBZ} = N/2$. The final equivalency on the right hand side is given since the Lagrange parameter in the Hamiltonian enforces $n_f = 1$. The Brillouin zone volume enclosed by the surface defined by the discontinuities in the single particle occupation number — the Luttinger volume — is determined only by bands which cross the Fermi energy.

The low temperature features of the PM phase, which for $J/t = 1$ is given by the region $\langle n_c \rangle \lesssim 0.880$, are well understood in this mean-field framework by setting $m_f = m_c = 0$ in (4.18) which recovers the generic hybridised band structure of the large- \mathcal{N} approximation with dispersion given by (4.8) and spectral weight given by (4.9). The large- \mathcal{N} result gives heavy (very flat band corresponding to large effective mass of the quasi-particles) bands $E_{\mathbf{k}\pm}$ crossing the Fermi energy in the vicinity of $\mathbf{k} = (\pi, \pi)$ and equivalent points. This is in excellent agreement with the DCA result in the PM phase. Based on this mean-field modelling of the DCA data, and since only the $E_{\mathbf{k},-}$ band crosses the FS, the Luttinger volume in the PM phase, V_L^{PM} , is given by: $V_L^{PM}/V_{BZ} = \frac{1}{N} \sum_{\mathbf{k} \in BZ} \Theta(-E_-(\mathbf{k}))$. For the paramagnet, the reciprocal space is given by the *full* BZ with Luttinger sum rule: $\frac{2}{N} \sum_{\mathbf{k} \in BZ, n} \Theta(-E_n(\mathbf{k})) = n_f + n_c$, which in combination with the volume yields

$$\frac{V_L^{PM}}{V_{BZ}} = \frac{n_f + n_c}{2} = \frac{1 + n_c}{2} \quad (6.2)$$

counting both conduction band electrons and magnetic moment spins. Since the mean-field model accounts very well for the DCA spectral function in the PM phase, we attribute the DCA result with this same *large* Luttinger volume.

In the strongly AF phase, close to half-filling with $0.926 \lesssim \langle n_c \rangle < 1$, the DCA spectrum with hole pockets around $(\pi/2, \pi/2)$ can again be well accounted for with the mean-field Hamiltonian of (4.18) but now setting non-vanishing staggered magnetisations, equal to the QMC measured observables, and also using a non-zero hybridisation value of about $V = 0.3$, for 3% doping for example, as fit parameter. An example spectrum produced via this procedure is given in Fig. 6.3(b). The value for V is chosen purely on the basis of whether the spectrum thus produced qualitatively matches the DCA result. Since for the given magnetisations, which we read out of the QMC simulation, a non-zero value of V is required to produce the observed hole-pockets, we conclude that the bands retain heavy fermion nature and that at least partial Kondo screening is present. In this fit, one band



(a) Single particle spectrum obtained in the large- \mathcal{N} mean-field approximation with $t'/t = -0.3$, model Hamiltonian (4.18) inserting the Monte-Carlo magnetisation measurements and required backfolding of the bands into a reduced (magnetic) Brillouin zone
 (b) The spectrum obtained from the 4-band $J/t = 1$ and 10% hole-doping but with artificial Carolo magnetisation measurements and required backfolding of the bands into a reduced (magnetic) Brillouin zone
 (c) The spectrum obtained from the 4-band $J/t = 1$ and 10% hole-doping but with artificial Carolo magnetisation measurements and required backfolding of the bands into a reduced (magnetic) Brillouin zone
 (d) The spectrum obtained from the 4-band $J/t = 1$ and 10% hole-doping but with artificial Carolo magnetisation measurements and required backfolding of the bands into a reduced (magnetic) Brillouin zone

Figure 6.3:

drops completely below the Fermi energy which itself is crossed only by the second band $E_2(\mathbf{k})$ in the vicinity of $\mathbf{k} = (\pi/2, \pi/2)$. In this case the Luttinger volume is given by

$$\frac{V_L^{AF}}{V_{MBZ}} = n_c \quad (6.3)$$

with the f -electrons excluded from the counting. Since the heavy fermion bands are still present but shifted to lower energies, we conclude that partial Kondo screening is present in the magnetic phase. However, the topology of the FS is actually that of a spin-density wave approximation ($V = 0$, $m_f = 1, m_c \neq 0$ in (4.18)) where the f -electrons are also frozen and do not participate in the Luttinger sum rule. Hence, we coin the FS, obtained from the DCA spectrum, as *small*.

For the intermediate region of the AF phase, which for $J/t = 1$ is given for $0.880 \lesssim \langle n_c \rangle \lesssim 0.926$ corresponding to staggered magnetisation $0 \lesssim m_z^f \lesssim 0.455$, we have the third variant for the Fermi-surface topology. In the extended zone scheme, holes are formed around (π, π) and $(0, 0)$. We understand this simply by considering the spectrum of the large- \mathcal{N} approach backfolded around $(\frac{\pi}{2}, \frac{\pi}{2})$ to take account of the reduction of the BZ which takes place with the breaking of the original lattice symmetry via AF ordering. This simple approach, depicted in Fig. 6.3(a) gives a good account of the DCA result for the intermediate parameter region and again may be classified as a large Fermi-surface topology.

We note some similarities to results recently observed in a variational Monte-Carlo approach to the KLM [52]. A major difference however is that in that work, although there

is a magnetic phase transition separating topologically different Fermi surfaces, it is of first order in the variational approach [52]. In contrast, the DCA calculation presented here supports a continuous transition. However, the transition between small and large Fermi surface topology does not occur at the quantum critical point. Such a situation may also occur experimentally: Experiments on the quantum criticality of the heavy fermion material YbRh_2Si_2 indicate, via a jump in the Hall coefficient, a topology change of the Fermi surface that is not coupled to the order-disorder QCP and which may occur to either side of the magnetic phase transition depending on positive or negative chemical pressure [18]. We note that the variational wave function corresponds to the ground-state Slater determinant of (4.18) supplemented by a Gutzwiller projection and the order parameters are determined by minimising the variational energy. The FS is then deduced from the mean-field Hamiltonian. In the presence of t' and close to half-filling one expects the observed AF_e FS phase [52], characterised by $V \neq 0, m_f \neq 0, m_c \neq 0$ to correspond to hole-pockets.

We now look at what happens at a larger coupling $J/t = 1.4$ upon hole-doping away from half-filling. We recall that at half-filling the lower band maximum was at (π, π) so that drawing on the experiences of the result for $J/t = 1$ and assuming a rigid band principle, where doping serves only to move the Fermi-energy down into the lower band without changing its qualitative structure, then the Fermi surface topology could be expected to be that of the backfolded large- \mathcal{N} case with holes around (π, π) and $(0, 0)$. What in fact happens is that firstly there appears to be no band crossing the Fermi-surface at all. The spectral functions obtained for $J/t = 1.4$ are shown in Fig. 6.4 going from half-filling (Fig. 6.4(a)) to approximately 6% hole-doping in Fig. 6.4(e). Extensive testing including comparing the value obtained for $\langle n_c \rangle$ from the QMC run with that obtained from the DCA result for the lattice Green function and also production of well controlled QMC data through large investment of computing time, have failed to resolve this problem.

If we consider this to be a numerical error and that the Fermi energy has been badly resolved in the spectral plots such that a small shift of the spectrum is required, then we would conclude that the Fermi surface is indeed the backfolded large- \mathcal{N} large FS topology. Progressively doping the system destroys the magnetic order, and the model undergoes a continuous phase transition to a PM metal. Here it is interesting to note that the apparent ‘gap’ in the spectrum also appears to be smaller or may even be considered to vanish in the absence of magnetic order. The same problem of apparent lack of Fermi surface in the AF region of the phase diagram is also present already for $J/t = 1.2$. If viewed as a numerical problem remedied by a small shift in the Fermi energy, the topology is also the large FS.

We summarise the above results for the magnetic phase diagram and Fermi surface topology in Fig. 6.5. It is clear in that plot that the region of phase space with a small Fermi

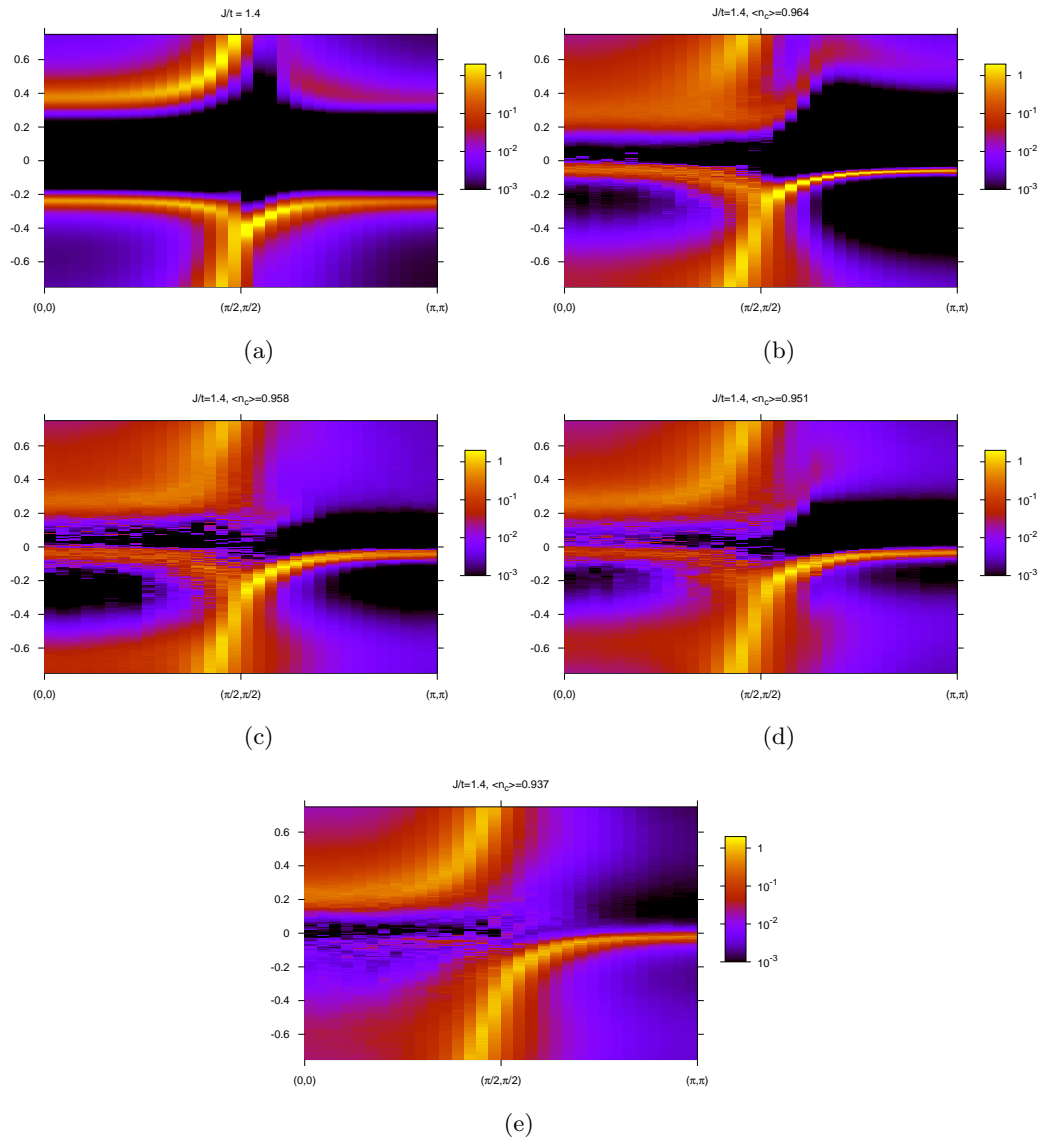


Figure 6.4: Single particle spectrum of the conduction electrons for $J/t = 1.4$.

surface with hole pockets around $(\pi/2, \pi/2)$ is characterised by a large staggered magnetisation. We also include Fig. 6.6 as a useful summary plot with a schematic summary of the three distinct areas of the phase diagram, the corresponding characteristic spectra in each of those areas, and the resultant Fermi surface topologies.

We note that the results summarised in the above are confirmed by the results of simulations carried out using the larger cluster size $N_c^{AF} = 4$, see Fig. 6.7. In particular, we observe the small Fermi surface topology in the strong AF region with small coupling J/t and evidence for a large Fermi surface in the weakly ordered region ($J/t \gtrsim 1.2$) although, again, the problem of a shift in the chemical potential is observed, such that no band clearly crosses the Fermi energy. The apparent gap, as read from a log-plot of the lattice Green function, is of equal size or even slightly larger than for $N_c^{AF} = 1$ when comparing simulations at equal doping and coupling.

Since the system, according to the QMC observable, is clearly doped but the single particle spectrum fails to reflect this, then we can make a tentative argument for the existence of some kind of quasiparticle pairing. A superconducting phase may be sandwiched between the paramagnetic Kondo screened regime and the strongly antiferromagnetic small Fermi surface regime topologies. This must be seen only as a hypothesis, since without susceptibility measurements we do not feel confident enough to exclude the possibility of numerical error in the results. Consider, for example, the difficulties in determining the correct high frequency behaviour of the self-energy using only a finite mesh in imaginary time. A poor resolution of the high frequency *tail* of the self-energy can act as an effective μ in the interacting Green function, thereby giving a systematic error in Fermi energy.

Exotic superconductivity of paired composite quasiparticles has been suggested in the vicinity of the QCP, mediated via antiferromagnetic fluctuations. We note that a d-wave superconducting phase has recently been suggested to exist for the Heisenberg KLM (with an additional J_{AF} coupling between magnetic impurities) [53].

The main result of this section still remains to be a reordering of the Fermi surface within the AF phase. We may ask ourselves what the driving force or mechanism for the topology change is, or what is the nature of transition? For example, does the band structure evolve continuously, perhaps becoming completely flat with divergent effective mass m^* ? The DCA data could never hope to give a clear answer here since the resolution of the quasiparticle spectrum is not great enough: In our phase diagram, Fig. 6.5, we draw the line dividing the two topologies through those simulation points in which we could not clearly distinguish between the two.

Drawing again on our model fit, the 4-band mean field with order parameters for magnetisation and for Kondo screening, we set a constant c-electron occupancy of $\langle n_c \rangle = 0.966$, coupling $J/t = 1.2$, and use the QMC values for the staggered magnetisations of f-electrons and c-electrons: $m_z^f = 0.517$, $m_z^c = 0.167$. Our DCA results show this AF ordered point

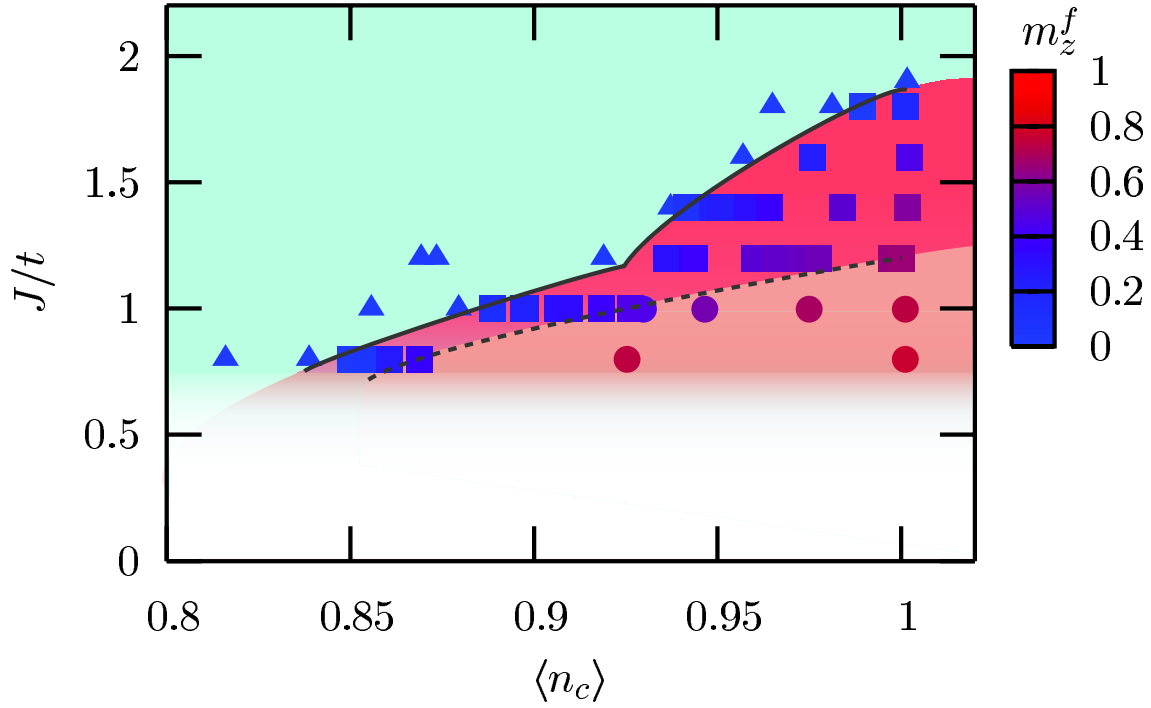


Figure 6.5: Ground state magnetic phase diagram of the hole-doped KLM showing simulation results for the staggered magnetisation m_z^f (colour-coded) as a function of coupling J/t and conduction electron occupancy $\langle n_c \rangle$. Triangles: PM region, large FS. Squares: AF, large FS. Circles: AF, small FS. Here $t'/t = -0.3$ and the calculations are carried out with the $N_c^{AF} = 1$ cluster.

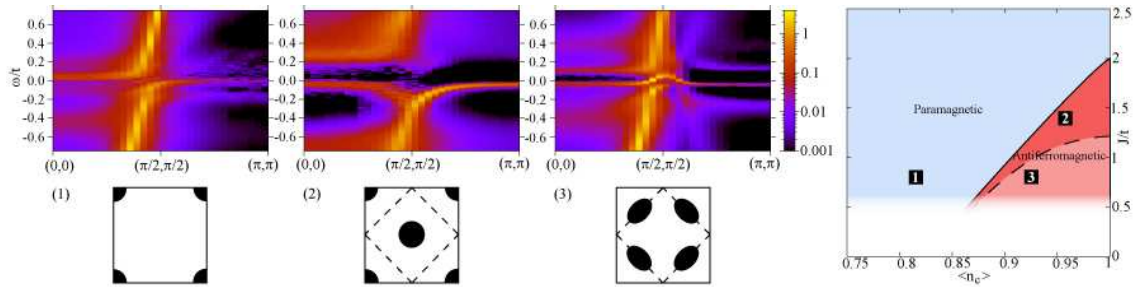


Figure 6.6: Summary of the three distinctive regions of the phase diagram, depicting characteristic spectrum and Fermi surface in each case.

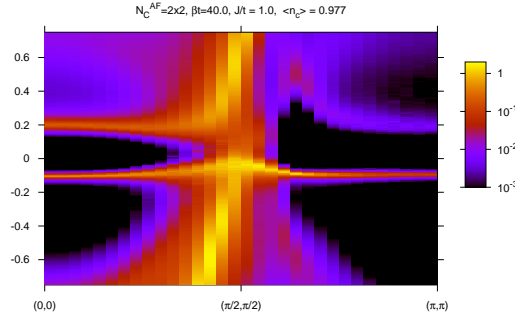


Figure 6.7: Single particle spectrum of the conduction electrons obtained using cluster size $N_c^{AF} = 4$ confirming that the small Fermi surface topology in the lightly doped AF phase with coupling $J/t = 1$ is not just an artifact of the smaller cluster results.

in the phase diagram to be just on the large Fermi surface side of the Lifshitz transition. Now, we show in Fig. 6.8 a series of plots of the band dispersion around the Fermi energy obtained with our model-fit for screening parameters ranging from $V = 0.30$ up to $V = 0.386$.

With small screening we can produce the small Fermi surface scenario and with increasing screening the band is forced into the large Fermi surface scenario, interestingly also going through an intermediate topology with holes at both $(\frac{\pi}{2}, \frac{\pi}{2})$ and (π, π) although here the energy scale is very small. In our modelling, the progression from small to large Fermi surface with increasing screening occurs gradually and there is no complete flattening of the band, and therefore no support for a divergent effective mass m^* .

This analysis is by no means conclusive, we use the model simply as a tool to understanding the DCA results, justifying the approach by noting that the band structure thus produced is highly resemblant of the DCA results. We therefore argue that the driving force for Fermi surface reconstruction is linked to the strength of Kondo screening.

6.4 The Spectral Function for $T \neq 0$

In the ground state phase diagram the point $J/t = 1$, $\langle n_c \rangle = 0.946$ is AF ordered and displays the small Fermi surface topology. In the series of plots shown in Fig. 6.10 the evolution of the single particle spectrum with these parameters is followed as we cool the system down, step by step, into this ground state. We firstly note from Fig. 6.9, which displays the corresponding staggered magnetisation at each of the temperature steps, that the magnetisation appears to develop smoothly with a Neel temperature of approximately $T_N = 0.04t$.

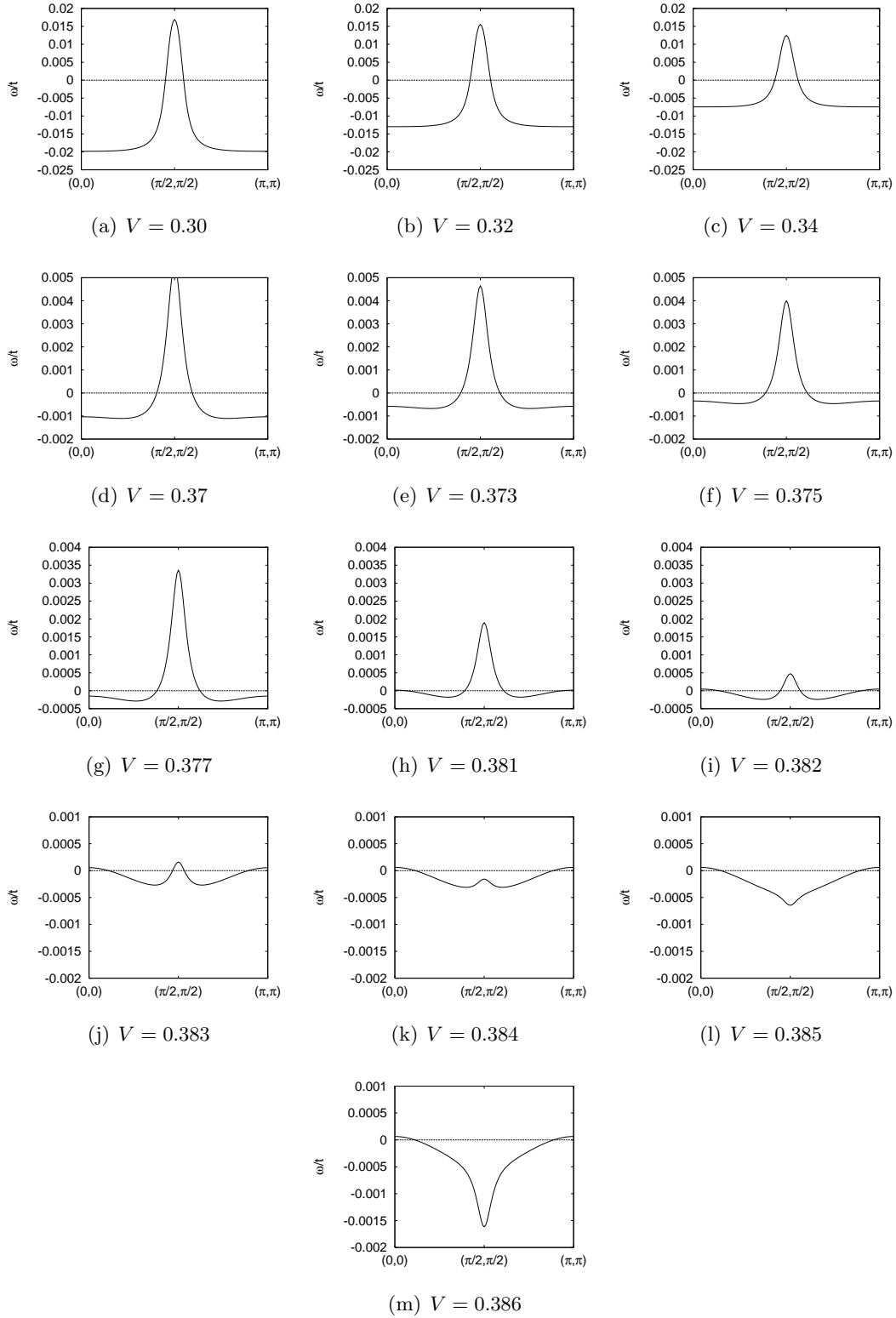


Figure 6.8: Following the evolution of the Zhang-Yu mean-field model band (see text) at the Fermi energy (dotted line) with increasing screening parameter V . Note the rescaling of the energy axis with at each row of three plots.

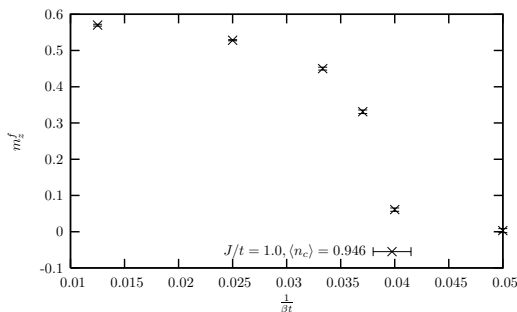


Figure 6.9: m_z^f as a function of temperature at constant conduction electron density $\langle n_c \rangle = 0.946$ and coupling $J/t = 1.0$

As we reduce the temperature, the spectral function arguably¹ evolves according to the following: From $\beta t = 20$ to $\beta t = 27$ the Kondo screening signature of the hybridised band around (π, π) strengthens. This suggests that the temperature has already dropped below the Kondo temperature T_K . Since the shadow bands associated with AF order begin to become evident only at $\beta t = 30$ we suggest that the temperature scale associated with the RKKY interaction at this point in the phase space is lower than the Kondo temperature. Only at the lowest temperature, given by $\beta t = 80$ do the band features sharpen. Therefore the final temperature scale is the coherence temperature T_{coh} where we may really speak of a Fermi liquid. If future simulations can be used to produce a plot of the specific heat we might be able to read off the coherence temperature as the point at which the curve becomes linear in T in accordance with Fermi liquid theory. From our results it is not clear whether just below the Neel temperature the Fermi surface is large or small. It would be interesting to attempt such a temperature scan closer to the ground state phase transition such that the ground state is known to be with large Fermi surface topology. Such temperature results would be aimed at mapping out not just the magnetic phase diagram, but paying close attention the development of the large or small Fermi surface with decreasing temperature, the temperature for Neel ordering and the development of a coherent Fermi liquid.

¹from the spectrum alone this is hard to read out, future work could perhaps be focused on the specific heat in order to trace singularities, or jumps, as the temperature drops under each energy scale successively

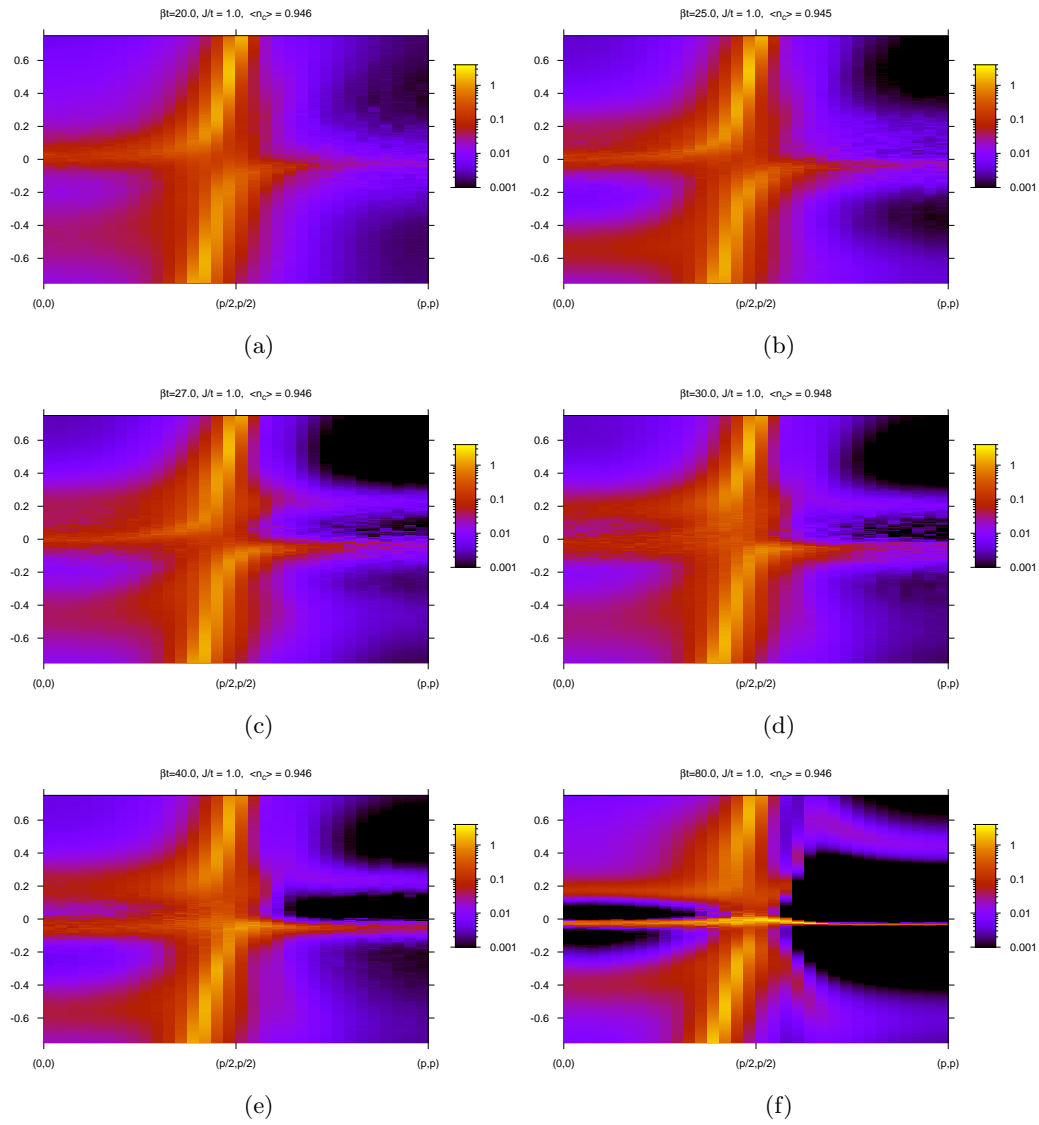


Figure 6.10: Tracking the single particle spectrum of the conduction electrons for $J/t = 1$ whilst reducing temperature. The conduction electron density is held at $\langle n_c \rangle = 0.946$ through suitable adjustment to the chemical potential

7 Summary and Conclusions

In this chapter we summarise this work and review the main results. The focus of this work has been on the two dimensional KLM both at half-filling and in the hole doped phase. The KLM is a strongly correlated system as discussed in the introduction, where particularly correlations in time are expected to play an important role. For this reason the numerical method we have used, the DCA, may be considered to be well suited to the problem. We have shown how the DCA makes an approximation to the self-energy by assuming only a weak momentum dependence whilst, however, retaining the full dynamics of the problem in imaginary time. The basis for the DCA is well founded, it is a conserving approximation from which we can, in theory at least, recover the original system without approximation by progressively increasing the cluster size.

In our particular implementation of the DCA, we wished to be able to perform simulations within the AF ordered phase because the nature of the Fermi surface in this region is currently of on-going interest, both theoretically for model Hamiltonians for heavy fermions, and experimentally in heavy fermion metals themselves. We developed a variant of the DCA approach in which we define an AF unit cell in real space and allow broken symmetry within that cell.

The DCA relies on one's ability to calculate the effective self-energy of the cluster, given the *bath* Green function \mathcal{G} , in which the interactions of the surrounding bath electrons have effectively been included. Since we have seen, by comparison of Feynman diagrams for the Baym-Kadanoff generating functional, that in the DCA the cluster self-energy has the same functional form as that of an impurity problem, then to calculate this cluster self-energy we draw on a QMC impurity solver: the Hirsch-Fye algorithm. In a previous work [29] we presented this algorithm in considerable detail, such that to save repetition, here we have presented only those adaptations of the algorithm which pertain to its implementation in solving for the KLM Hamiltonian. To this end, we re-wrote the KLM in a form suitable for the introduction of auxiliary fields, noting that in order to implement the Hilbert space restriction of single occupancy on the f-orbitals in the KLM, we introduce a Hubbard U term on these sites with U chosen large enough as to give a measured value for the double occupancy of practically zero. The Hubbard U term is handled in the standard way as first introduced by Hirsch and Fye [34]. The J -term of the KLM required the introduction of a second auxiliary field variable, and we derived the relevant update equation and QMC process for implementing the algorithm. Here we note however one of the drawbacks of

using the Hirsch-Fye algorithm: The computational time required scales with $(\beta N_c)^3$, the inverse temperature times number of cluster orbitals to the power three. The algorithm is actually not well suited to large clusters due to the prohibitive time scaling. However, we saw later in the first results chapter for the half-filled KLM that the single particle spectral function obtained in the DCA approach with only N_c^{AF} (two f-electrons, two c-electrons in the cluster) already compared extremely favourably with that obtained via exact QMC simulations on a 12×12 lattice.

Also included in the methods section at the end of chapter 2 we discussed some technical aspects applicable when implementing DCA together with QMC. Of importance is the method for *unfolding* the obtained lattice Green functions in the MBZ in order to plot in the extended BZ. Also, we discuss an elegant method of interpolating the self-energy between the values obtained in the DCA cluster patches in k-space.

Before moving on to discuss results we presented three useful mean-field or SDW approaches to the KLM. The so-called large- \mathcal{N} approach is very successful at describing the large J limit of the KLM, with hybridised heavy fermion bands and gapped quasi-particle spectrum, but cannot capture the broken symmetry AF phase. For this, we proposed the SDW approach, in which the conduction electrons are considered as moving in the fixed AF ordered magnetic field generated by the localised f-electron spins. Notable aspects here are a quasi-particle gap scaling linearly with J/t for next-nearest neighbour hopping $t'/t = 0$ but which is absent for small J/t with $t'/t = -0.3$. However, the SDW approach does not take account of Kondo screening, which has been previously proposed to continue to partially exist in the AF ordered phase. Our third *toy-model* approach is the Zhang-Yu mean field approach which introduces order parameters for magnetic ordering but also for Kondo screening. Although the self-consistent solution of this approach is known to rule out continued Kondo screening in the AF phase, we still draw on the model to help interpret our quasiparticle spectra results on the grounds of recognising which ingredients might be necessary in order to observe a given band structure and Fermi surface topology.

Turning now to our results sections, to begin with we looked at the KLM at half-filling. We made the important point that the half-filled KLM with nearest neighbour hopping t displays a perfect nesting instability to AF order. We made the case for including a next-nearest neighbour hopping element $t'/t = -0.3$ in order to lift nesting of the Fermi surface whilst still retaining a significant peak in the conduction electron spin susceptibility at the AF ordering momentum vector (π, π) . After verifying, by measurement of the staggered magnetisation, a continuous phase transition from paramagnetic insulator to AF insulator with decreasing coupling J/t we tracked the evolution of the quasiparticle spectra across the transition.

In the paramagnetic phase the key feature is a very flat heavy fermion band and also the fact that the spectrum is gapped. This is in accordance with the picture painted by strong

coupling, large J/t , as discussed in the introduction. Our DCA calculation for half-filling gives the AF phase transitions to be approximately at $J_c/t = 2.1 \pm 0.05$ for $t'/t = 0$ and at $J_c/t = 1.85 \pm 0.05$ for $t'/t = -0.3$. The $t' = 0$ result is higher than the generally accepted value of $J_c/t = 1.45 \pm 0.05$, but we note that the small cluster size of only one AF unit cell ($N_c^{AF} = 1$) may be conducive to enhancement of AF order. With increasing cluster size we would expect to progressively move towards the lattice results. The important point is that our method is able to capture the essence of the interplay between RKKY interaction and Kondo screening, and the agreement of the single particle spectra of the DCA results with the lattice results is extremely favourable. In the AF phase the typical feature is backfolding of the spectrum around (π, π) to reflect the reduction of the BZ with the breaking of lattice translational symmetry.

For $t'/t = -0.3$, careful tracking of lower-band maximum and upper-band minimum revealed four distinct regions of the J/t axis where these maxima and minima are found at differing locations in the BZ. Later we saw, that with hole doping, a rigid band idea holds, and the holes doped into the system form at the lower-band maxima positions observed at half-filling.

We also reported measurements for the quasiparticle gap both with and without next-nearest neighbour hopping. For $t'/t = 0$ we are able to verify a linear scaling of the gap, $\Delta_{qp} \propto J/t$, at small J/t . This is the result suggested by the SDW approach. However, the results for $t'/t = -0.3$ are consistent with an exponential scaling with J/t , i.e. the gap tracks the Kondo scale. Again, a consistent comparison can be made with the SDW model for $t'/t = -0.3$, since, in that approach, the gap is absent. Therefore the existence of a gap in our DCA results can only be associated with the hybridisation gap and, rightly so, tracks the exponential Kondo scale. We conclude that the generic result is that the gap follows the exponential Kondo scale and that only in the case of perfect nesting $t'/t = 0$ does the gap become linear with small J/t .

In the hole-doped region, AF order survives and we observe an extended AF metallic region giving way progressively, with a continuous magnetic order quantum phase transition to a PM metallic region with further hole-doping (or decreasing conduction electron occupancy $\langle n_c \rangle$). Our major result has been to follow the evolution of the Fermi surface which for $J/t < 1.2$ can undergo a topology change, a Lifshitz transition, within the AF phase. We see three distinct Fermi surface topologies in the magnetic phase diagram of the doped KLM. The PM phase always displays the so-called *large* Fermi surface topology, in which the f-electrons participate in the Luttinger volume sum rule, and the Fermi surface is given by holes in the heavy fermion band around (π, π) . With the initial development of AF order, and for all values of coupling down to $J/t = 0.8$, we observe a simple backfolding of the PM band spectrum into the MBZ, such that holes are present at $(0, 0)$. However, in those regions of the phase diagram with the strongest magnetisation, $J/t < 1.2$ and low

hole doping, there is a reconstruction of the Fermi surface with holes around $(\frac{\pi}{2}, \frac{\pi}{2})$ and the Luttinger volume is the same as for the SDW approach. Based on this we conclude that in this region the f-electron do not participate in the Luttinger sum rule and the resultant Fermi surface is to be classed as *small*. Since this topology change does not take place at the magnetic transition then the QCP may still be interpreted in terms of a Hertz-Millis transition. We do not need to draw on the ideas of local quantum criticality in which a breakdown of Kondo screening via local magnetic fluctuations is proposed at the QCP. With the aid of the Zhang-Yu mean field Hamiltonian we produced a qualitative fit to the small Fermi surface result via variation of the screening parameter V . We also saw that keeping the magnetisation constant and varying V drives the band structure from the large to small Fermi surface scenario, although going through an intermediate stage with holes at both $(0, 0)$ and $(\frac{\pi}{2}, \frac{\pi}{2})$ albeit with the crossing of the Fermi energy on a very small energy scale. The dispersion obtained in this way does not suggest a total flattening of the band during the transition from large to small Fermi surface, such that we might not expect a divergence of the effective mass m^* .

We have also presented initial results at finite temperature, cooling the system down from above the Neel temperature into a small Fermi surface ground state. Different energy scales play a role: the Kondo temperature T_K , where initial Kondo screening of the magnetic moments occurs, the Neel temperature T_N for AF ordering, the temperature T^* at which a possible restructuring of the Fermi surface occurs, and the coherence temperature T_{coh} for coherent formation of heavy quasi-particles and the Fermi liquid regime. From the remarks of the previous paragraph, a temperature driven Fermi surface topology change may not result in divergence of the specific heat C_V as would be associated with a flat heavy fermion band and divergent effective mass m^* . However, our consideration of the evolution of the dispersion would support a discontinuous jump in C_V at reordering.

We see that the magnetic phase diagram of the KLM as a function of doping, coupling and temperature is very complex, and remains an interesting focus for further investigation, particularly owing to the large number of recent high profile experimental papers concerned with Fermi surface topology and quantum criticality in heavy fermion systems.

Recent developments in numerical methods make direct measurement of susceptibilities more feasible [39]. This provides one clear direction for future work. Additionally, continued research into the third dimension in the magnetic phase diagram, namely temperature, is needed. Signatures of the characteristic energy scales of initial Kondo screening, AF order, topology change and coherence can be searched for in the single particle spectrum at different points in the phase diagram. Also, ambitious calculations of the specific heat would be expected to highlight these energy scales. The problem of the apparent lack of Fermi surface for intermediate coupling also remains open. A search for pairing correlations might possibly shed light on the apparent gap.

A Linear Response and the Kubo Formalism

Starting with a non-interacting system of electrons described by the Hamiltonian H_0 we can ask ourselves the question: How does the system react to a small perturbation V ? The answer will be given by a response function such as an electrical conductivity, a susceptibility or an equivalent correlation function depending on the nature of the perturbation. For example, in the context of this work, we will consider the effect of a magnetic field on the magnetisation M of the conduction electrons of the KLM. The magnetisation response to the field B will be given by $M = \chi B$, where the field strength is sufficiently small such that M is linearly proportional to B via the magnetic susceptibility χ , which is the quantity we wish to calculate. In this small field regime the talk is therefore of "linear response theory". Formulae for response functions of the type presented in this section were first proposed by Green [54, 55] in application to transport in liquids. However linear response theory is more strongly associated with Kubo who first derived equations of this kind for electrical conductivity in solids [56]. Today, the term "Kubo formula" is applied to all such equations for response correlations functions in a variety of regimes such as zero and finite temperature, static or dynamical quantities, and for numerous applications ranging from calculation of optical properties to electrical transport or, as will be the case here, magnetic susceptibility.

We begin by writing a perturbed Hamiltonian $\hat{H} = \hat{H}_0 + \hat{V}$ with perturbation term \hat{V} given by

$$\hat{V}_t = \hat{B}F_t \tag{A.1}$$

such that an externally applied field F couples to the observable \hat{B} . We write the index t on the field and perturbation to represent that we are considering fields which may be explicitly time-dependent. How is the expectation value of an observable \hat{A} changed in the presence of this field? Firstly, *without* the field we may write

$$\langle A \rangle_0 = \text{Tr}(\rho_0 A) \tag{A.2}$$

where from now on we drop the hat symbol used to designate operators. Continuing, we assume that the field was turned on at some point in the past and gradually, *adiabatically*, increased to reach the required strength F_t . The density operator used to calculate the expectation value changes accordingly:

$$\rho_0 \rightarrow \rho_t \tag{A.3}$$

To account for the turning-on and adiabatic increasing of the field we can set the following boundary conditions:

$$\lim_{t \rightarrow -\infty} \rho_t = \rho_0 \quad (\text{A.4})$$

It is clear that we need to find an expression for ρ_t in the presence of the field. Consider the density operator in Dirac representation

$$\rho_t^D(t) = e^{iH_0 t} \rho_t e^{-iH_0 t} \quad (\text{A.5})$$

where we make the point of distinguishing between the explicit time-dependency (index t) due to time dependency of the external field and the time evolution of the operator described by H_0 in the Dirac representation (t in round brackets). We may now derive

$$\frac{d}{dt} \rho_t^D(t) = i H_0 e^{iH_0 t} \rho_t e^{-iH_0 t} - i e^{iH_0 t} \rho_t e^{-iH_0 t} H_0 + e^{iH_0 t} \frac{\partial \rho_t}{\partial t} e^{-iH_0 t} \quad (\text{A.6})$$

To deal with the time derivative in the last term we can use $\dot{\rho}_t = \frac{d}{dt} (\sum_m p_m |\psi(t)\rangle \langle \psi(t)|)$ and also $i |\dot{\psi}(t)\rangle = H |\psi(t)\rangle$ to give us

$$\frac{\partial \rho_t}{\partial t} = -i [H, \rho_t]_- \quad (\text{A.7})$$

and now

$$\frac{d}{dt} \rho_t^D(t) = i e^{iH_0 t} [H_0 - H, \rho_t]_- e^{-iH_0 t} \quad (\text{A.8})$$

$$= i [\rho_t^D(t), V_t^D(t)]_- \quad (\text{A.9})$$

The formal solution of this equation of motion for the density operator in Dirac representation under the boundary condition A.4 is

$$\rho_t^D(t) = \rho_0 - i \int_{-\infty}^t dt' [V_{t'}^D(t'), \rho_{t'}^D(t')]_- \quad (\text{A.10})$$

where we note that ρ_0 can be considered to be in Schrödinger representation since ρ_0 commutes with H_0 and therefore also with the Dirac time evolution exponentials which then cancel each other out. With this equation $\rho_t^D(t)$ may be iteratively inserted into the commutator on the right hand side to produce higher order terms in the perturbation $V_t^D(t)$. However, we make the assumption that the externally applied field F_t is sufficiently small that we may neglect these higher order terms and need only retain the linear term in V to obtain the approximation

$$\rho_t^D(t) = \rho_0 - i \int_{-\infty}^t dt' [V_{t'}^D(t'), \rho_0]_- \quad (\text{A.11})$$

or equivalently

$$\rho_t = \rho_0 - i \int_{-\infty}^t dt' e^{-iH_0 t} [V_{t'}^D(t'), \rho_0]_- e^{iH_0 t} \quad (\text{A.12})$$

with ρ_t returned to Schrödinger representation. With this equation for ρ_t we can now calculate the linear response of the observable A in the applied field F_t which couples to the observable B :

$$\begin{aligned}
\langle A \rangle_t &= \text{Tr} \{ \rho_t A \} \\
&= \text{Tr} \{ \rho_0 A \} - i \int_{-\infty}^t dt' F_{t'} \text{Tr} \left\{ \rho_0 [A^D(t), B^D(t')]_- \right\} \\
&= \langle A \rangle_0 - i \int_{-\infty}^t dt' F_{t'} \langle [A^D(t), B^D(t')]_- \rangle_0
\end{aligned} \tag{A.13}$$

Equation A.13 is a general formulation of a Kubo formula for linear response and is used in section 5.1 in the discussion of perfect nesting.

B Delayed Update Algorithm Improvement

At the core of the update is an outer product for which we use the BLAS routine *dger*. We note that gprof call graph analysis shows the program to spend over 90% of the total time in this optimised BLAS routine. The compute time for one update therefore scales with $(N_{orb}L)^2$ so that a sweep through all the auxiliary fields requires a time that scales with $(N_{orb}L)^3$ or, equivalently, that scales as $(N_{orb}\beta)^3$. However, the efficiency of the algorithm has recently been improved further [57]. It is possible to delay update steps on the whole green function matrix, calculating and storing instead only the updated rows and columns corresponding to the Monte-Carlo move in the auxiliary field. After accumulating $Nstep$ such moves, the update on the whole Green function matrix can be carried out via a matrix-matrix product of the rectangular matrices built up from each delayed update step. For this the BLAS routine *dgemm* is used. The details of the update and calculation of rectangular storage matrices show that as long as $1 \ll Nstep \ll L$ then the algorithm will scale as $(N_{orb}\beta)^x$ where now $x < 3$. In figure B.1 we compare the CPU time required by the two methods using data from a series of actual production runs. The vast improvement in efficiency of approximately one whole order of magnitude, opens the door to exciting new simulation possibilities deserving exploitation. Simulations close to the phase transition provide some of the most interesting physics but, with regards to computing time, are amongst the most intensive.

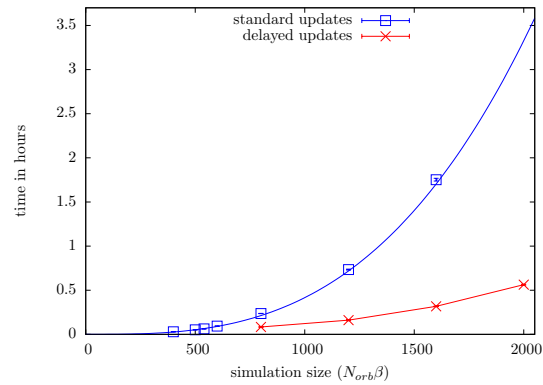


Figure B.1: Comparison of our improved *delayed updates* QMC algorithm with the original standard updates algorithm - For the standard update procedure the curve represents a best fit to the theoretically expected computer time scaling behaviour $\propto (N_{orb}\beta)^3$. The simulation running times given are for one iteration of our program. A typical simulation may sometimes require in the order of 70 iterations to reach convergence. The delayed updates procedure reduces the computing time by a factor of up to seven, which will allow us to carry out very ambitious large scale simulations.

Bibliography

- [1] P. W. Anderson, *Localized Magnetic States in Metals*, Phys. Rev. **124**, 41 (1961).
- [2] B. T. Matthias, M. Peter, H. J. Williams, A. M. Clogston, E. Corenzwit, and R. C. Sherwood, *Magnetic Moment of Transition Metal Atoms in Dilute Solution and Their Effect on Superconducting Transition Temperature*, Phys. Rev. Lett. **5**, 542 (1960).
- [3] A. M. Clogston, B. T. Matthias, M. Peter, H. J. Williams, E. Corenzwit, and R. C. Sherwood, *Local Magnetic Moment Associated with an Iron Atom Dissolved in Various Transition Metal Alloys*, Phys. Rev. **125**, 541 (1962).
- [4] S. Doniach, *The Kondo lattice and weak antiferromagnetism*, Physica B **91**, 231 (1977).
- [5] A. C. Hewson, *The Kondo Problem to Heavy Fermions*, Cambridge Studies in Magnetism (Cambridge University Press, Cambridge, 1997).
- [6] S. Burdin, A. Georges, and D. R. Grempel, *Coherence scale of the Kondo Lattice*, Phys. Rev. Lett. **85**, 1048 (2000).
- [7] F. F. Assaad, *Coherence scale of the two-dimensional Kondo Lattice model.*, Phys. Rev. B **70**, 020402 (2004).
- [8] M. A. Ruderman and C. Kittel, *Indirect Exchange Coupling of Nuclear Magnetic Moments by Conduction Electrons*, Phys. Rev. **96**, 99 (1954).
- [9] T. Kasuya, *A Theory of Metallic Ferro- and Antiferromagnetism on Zener's Model*, Prog. Theo. Phys. **16**, 45 (1956).
- [10] K. Yosida, *Magnetic Properties of Cu-Mn Alloys*, Phys. Rev. **106**, 893 (1957).
- [11] S. Paschen, T. Lühmann, S. Wirth, P. Gegenwart, O. Trovarelli, C. Geibel, F. Steglich, P. Coleman, and Q. Si, *Hall-effect evolution across a heavy-fermion quantum critical point*, Nature **432**, 881 (2004).
- [12] J. A. Hertz, *Quantum critical phenomena*, Phys. Rev. B **14**, 1165 (1976).
- [13] A. J. Millis, *Effect of a nonzero temperature on quantum critical points in itinerant fermion systems*, Phys. Rev. B **48**, 7183 (1993).

- [14] Q. Si, S. Rabello, K. Ingersent, and J. Smith, *Locally critical quantum phase transitions in strongly correlated metals.*, Nature **413**, 804 (2001).
- [15] T. Senthil, M. Vojta, and S. Sachdev, *Weak magnetism and non-Fermi liquids near heavy-fermion critical points*, Phys. Rev. B **69**, 035111 (2004).
- [16] N. Harrison, S. E. Sebastian, C. H. Mielke, A. Paris, M. J. Gordon, C. A. Swenson, D. G. Rickel, M. D. Pacheco, P. F. Ruminer, J. B. Schillig, J. R. Sims, A. H. Lacerda, M.-T. Suzuki, H. Harima, and T. Ebihara, *Fermi Surface of CeIn₃ above the Néel Critical Field*, Phys. Rev. Lett. **99**, 056401 (2007).
- [17] S. K. Goh, J. Paglione, M. Sutherland, E. C. T. O'Farrell, C. Bergemann, T. A. Sayles, and M. B. Maple, *Fermi-Surface Reconstruction in CeRh_{1-x}Co_xIn₅*, Phys. Rev. Lett. **101**, 056402 (2008).
- [18] S. Friedemann, T. Westerkamp, M. Brando, N. Oeschler, S. Wirth, P. Gegenwart, C. Krellner, C. Geibel, and F. Steglich, *Detaching the antiferromagnetic quantum critical point from the Fermi-surface reconstruction in YbRh₂Si₂*, Nature **5**, 465 (2009).
- [19] W. Knafo, S. Raymond, P. Lejay, and J. Flouquet, *Antiferromagnetic criticality at a heavy-fermion quantum phase transition*, Nature **5**, 753 (2009).
- [20] H. Tsunetsugu, M. Sigrist, and K. Ueda, *The ground-state phase diagram of the one-dimensional Kondo lattice model*, Rev. Mod. Phys. **69**, 809 (1997).
- [21] J. R. Schrieffer and P. A. Wolff, *Relation between the Anderson and Kondo Hamiltonians*, Phys. Rev. **149**, 491 (1966).
- [22] Y. Onuki and T. Komatsubara, *Heavy fermion state in CeCu₆*, J. Magn. Magn. Mater. **63&64**, 281 (1987).
- [23] R. M. White, *Quantum Theory of Magnetism*, 2 ed. (Springer, Berlin, 1983).
- [24] E. H. Lieb, *The Hubbard Model: Some Rigorous Results and Open Problems*, (1993), arXiv:cond-mat/9311033v2 (journal reference: XI Int. Cong. MP, Int. Press (1995) 392-412).
- [25] W. Metzner and D. Vollhardt, *Correlated Lattice Fermions in d=∞ Dimensions*, Phys. Rev. Lett. **62**, 324 (1989).
- [26] E. Müller-Hartmann, *Correlated fermions on a lattice in high dimensions*, Z. Phys. B **74**, 507 (1989).
- [27] U. Brandt and C. Mielsch, *Thermodynamics and correlation functions of the Falicov-Kimball model in large dimensions*, Z. Phys. B **75**, 365 (1989).

-
- [28] A. Georges, G. Kotliar, W. Krauth, and M. J. Rozenberg, *Dynamical mean-field theory of strongly correlated fermion systems and the limit of infinite dimensions*, Rev. Mod. Phys. **68**, 13 (1996).
- [29] L. C. Martin, *Dynamic Mean Field Theory and a Projector Quantum Monte-Carlo Method* (Institut für Theoretische Physik und Astrophysik, Universität Würzburg, Würzburg, 2004), pp. 10–12.
- [30] T. Maier, M. Jarrell, T. Pruschke, and M. H. Hettler, *Quantum cluster theories*, Rev. Mod. Phys. **77**, 1027 (2005).
- [31] G. Baym and L. P. Kadanoff, *Conservation Laws and Correlation Functions*, Phys. Rev. **124**, 287 (1961).
- [32] G. Baym, *Self-Consistent Approximations in Many-Body Systems*, Phys. Rev. **127**, 1391 (1962).
- [33] S. Capponi and F. F. Assaad, *Spin and charge dynamics of the ferromagnetic and antiferromagnetic two-dimensional half-filled Kondo lattice model*, Phys. Rev. B **63**, 155114 (2001).
- [34] J. E. Hirsch and R. M. Fye, *Monte Carlo Method for Magnetic Impurities in Metals*, Phys. Rev. Lett. **56**, 2521 (1986).
- [35] A. Sandvik, *Stochastic method for analytic continuation of quantum Monte Carlo data*, Phys. Rev. B **57**, 10287 (1998).
- [36] K. S. D. Beach, *Identifying the maximum entropy method as a special limit of stochastic analytic continuation*, cond-mat/0403055 (2004).
- [37] M. Jarrell, T. Maier, C. Huscroft, and S. Moukouri, *Quantum Monte Carlo algorithm for nonlocal corrections to the dynamical mean-field approximation*, Phys. Rev. B **64**, 195130 (2001).
- [38] S. Hochkeppel, F. F. Assaad, and W. Hanke, *Dynamical-quantum-cluster approach to two-particle correlation functions in the Hubbard model*, Phys. Rev. B **77**, 205103 (2008).
- [39] F. F. Assaad, private discussion.
- [40] F. F. Assaad, M. Imada, and D. J. Scalapino, *Charge and spin structures of a $d_{x^2-y^2}$ superconductor in the proximity of an antiferromagnetic Mott insulator*, Phys. Rev. B **56**, 15001 (1997).

- [41] G. G. Batrouni and P. de Forcrand, *Fermion sign problem: Decoupling transformation and simulation algorithm*, Phys. Rev. B **48**, 589 (1993).
- [42] F. F. Assaad and H. G. Evertz, in *Computational Many-Particle Physics*, edited by H. Fehske, R. Schneider, and A. Weiße (Springer, Berlin, 2008), Vol. 1, pp. 337–344.
- [43] R. Blankenbecler, D. J. Scalapino, and R. L. Sugar, *Monte Carlo calculations of coupled boson-fermion systems. I*, Phys. Rev. D **24**, 2278 (1981).
- [44] W. H. Press, S. A. Teukolsky, W. T. Vetterling, and B. P. Flannery, *Numerical Recipes in C* (Cambridge University Press, Cambridge, 1992).
- [45] N. Read and D. N. Newns, *On the solution of the Coqblin-Schrieffer Hamiltonian by the large- N expansion technique*, J. Phys. C **16**, 3273 (1983).
- [46] A. Auerbach and K. Levin, *Kondo Bosons and the Kondo Lattice: Microscopic Basis for the Heavy Fermi Liquid*, Phys. Rev. Lett. **57**, 877 (1986).
- [47] A. J. Millis and P. A. Lee, *Large-orbital-degeneracy expansion for the lattice Anderson model*, Phys. Rev. B **35**, 3394 (1987).
- [48] J. M. Luttinger, *Fermi Surface and Some Simple Equilibrium Properties of a System of Interacting Fermions*, Phys. Rev. **119**, 1153 (1960).
- [49] P. Fazekas, *Lecture Notes on Electron Correlation and Magnetism* (World Scientific, Singapore, 1999), pp. 363–386.
- [50] G.-M. Zhang and L. Yu, *Kondo singlet state coexisting with antiferromagnetic long-range order: A possible ground state for Kondo insulators*, Phys. Rev. B **62**, 76 (2000).
- [51] I. M. Lifshitz, *Anomalies of electron characteristics of a metal in the high pressure region*, Sov. Phys. JETP **11**, 1130 (1960).
- [52] H. Watanabe and M. Ogata, *Fermi Surface Reconstruction without Breakdown of Kondo Screening at Quantum Critical Point*, Phys. Rev. Lett. **99**, 136401 (2007).
- [53] J. C. Xavier and E. Dagotto, *Robust d -wave Pairing Correlations in the Heisenberg Kondo Lattice Model*, Phys. Rev. Lett. **100**, 146403 (2008).
- [54] M. S. Green, *Markoff Random Processes and the Statistical Mechanics of Time-Dependent Phenomena*, The Journal of Chemical Physics **20**, 1281 (1952).
- [55] M. S. Green, *Markoff Random Processes and the Statistical Mechanics of Time-Dependent Phenomena. II. Irreversible Processes in Fluids*, The Journal of Chemical Physics **22**, 398 (1954).

- [56] R. Kubo, *Lectures in Theoretical Physics, Vol. I* (Wiley-Interscience, New York, 1959), pp. 120–203.
- [57] G. Alvarez, M. S. Summers, D. E. Maxwell, M. Eisenbach, J. S. Meredith, J. M. Larkin, J. Levesque, T. A. Maier, P. R. C. Kent, and E. F. D. *et al.*, *SC 08: Proceedings of the 2008 ACM/IEEE Conference on Supercomputing* (IEEE Press, Piscataway N.J., 2008), p. 110.

Publications

Parts of this work have led to publication:

- L. C. Martin and F. F. Assaad
Evolution of the Fermi Surface across a Magnetic Order-Disorder Transition in the Two-Dimensional Kondo Lattice Model: A Dynamical Cluster Approach
Phys. Rev. Lett. **101**, 066404 (2008)

- L. C. Martin, F. F. Assaad, W. Hanke
Numerical Simulations of Heavy Fermion Systems
NIC Symposium 2008 (proceedings), Gernot Münster, Dietrich Wolf, Manfred Kremer (Editors)
(NIC Scientific Council)

Date of Birth: 16th March 1978
Place of Birth: Basingstoke
Nationality: British

Education

11/2004 - 11/2009 University of Würzburg, Germany
- PhD Studies

10/1998 - 11/2004 University of Würzburg, Germany
- Physics Diplom

08/2001 - 05/2002 University of Grenoble, France
- Student Exchange Program

1997 University of Würzburg, Germany
- German Language Courses

09/1994 - 06/1996 Queen Mary's College, Basingstoke, U.K.
- A' level Examinations

1990 - 1994 Hurst Community School, Tadley, U.K.
- GCSE Examinations

Employment

11/2004 - 11/2009 University of Würzburg, Germany
- Scientific Research Assistant

05/2004 - 07/2009 University of Würzburg, Germany
- Teaching Assistant

06/2002 - 09/2002 A.W.E Aldermaston, U.K.
- Summer Placement Student

Languages

English, German, French

Acknowledgements

I would like to thank the following people for discussions, support or guidance, without whom this work would not have been possible:

- Prof. Dr. Fakher Assaad, for the opportunity to work with you on this project, your support and guidance throughout these years is much appreciated. Discussing physics with you never ceased to motivate.
- All colleagues and friends within the solid state theory department, and one or two from beyond, with particular mention of Christian Brünger, Stephan Hochkeppel, Thomas Lang, Julia Wernsdorfer, Maximilian Aulbach, Stefan Karg, and special thanks to Judith Stahl for ensuring a smooth running department!
- Many thanks to David Luitz for last minute German language corrections in the *Kurzfassung*

I also most sincerely thank my parents for all their ongoing support.

Finally, a big thank you to Priscilla Martin.

Versicherung an Eides statt

Hiermit versichere ich, Lee C. Martin geboren am 16. März 1978 in Basingstoke, an Eides statt, dass ich die vorliegende Arbeit eigenständig, d.h. insbesondere ohne Hilfe eines kommerziellen Promotionsberaters angefertigt habe. Es wurden keine anderen als in der Arbeit angegebenen Quellen und Hilfsmittel benutzt. Diese Arbeit liegt nicht in gleicher oder anderer Form in einem anderen Prüfungsfach vor.

Würzburg, am 8. Dezember 2009

Lee C. Martin